Imperial College London

Nonlinear Optics in Nanoantennas

John Jinsung Yang

Department of Physics
Imperial College London

January 2025

Submitted in partial fulfilment of the requirements for the degree of
Doctor of Philosophy of Imperial College London

Abstract

Nonlinear optical processes are inherently weak in nanoantennas, but this can be significantly enhanced through the use of plasmonic resonances and field enhancements. This thesis presents an experimental investigation of two different designs for plasmonic nanoantennas to demonstrate different mechanisms via nonlinear optical measurements. In the first, the existence of a critical coupling condition that maximises field enhancement is explored in coupled waveguide-dimer nanoantennas. The prediction formed by fitting experimental data to the coupled oscillator model is confirmed via measurements of second harmonic generation and third harmonic generation that vary with a geometric parameter within the nanoantenna design. A second plasmonic nanoantenna is used to demonstrate the stimulated emission tomography technique, which allows for characterisation of a spontaneous parametric process by studying its stimulated analogue. Four-wave mixing is observed in individual nanoantennas, and stimulated emission tomography is performed to reconstruct the joint spectral density maps for spontaenous four-wave mixing. Furthermore, a key derivation in the technique is used to assess the spontaneous four-wave mixing generation rate in the nanoantennas, which is found to be approximately 100 pairs generated per second per mW of pump power and per nanoantenna. Further optimisation of the nanoantenna design is expected to increase this value significantly.

Statement of Originality

I declare that the work presented in this thesis is my own and that the works of others have been appropriately referenced and acknowledged.

John Jinsung Yang

August 2024

Copyright Statement

The copyright of this thesis rests with the author. Unless otherwise indicated, its contents are licensed under a Creative Commons Attribution-Non Commercial 4.0 International Licence (CC BY-NC).

Under this licence, you may copy and redistribute the material in any medium or format. You may also create and distribute modified versions of the work. This is on the condition that: you credit the author and do not use it, or any derivative works, for a commercial purpose.

When reusing or sharing this work, ensure you make the licence terms clear to others by naming the licence and linking to the licence text. Where a work has been adapted, you should indicate that the work has been changed and describe those changes.

Please seek permission from the copyright holder for uses of this work that are not included in this licence or permitted under UK Copyright Law.

Publications

- Yang, J., Dichtl P., Flórez, J., Phillips, C.C., Clark, A.S. and Oulton, R.F. *Stimulated emission tomography analysis of plasmonic nanoantennas* in *Active Photonic Platforms 2022* **12196** (2022), 78–84

- Xiao, X., Yang, J., Severs, T., Zhu, S., Kowalczyk, K., Tisch, J.W.G., Matthews, M., Maier, S.A. and Oulton, R.F. Nanofocusing in Critically Coupled Nanogap Waveguide Resonators. *ACS Photonics* **11**, 2836–2842 (2024). (Co-first author)

- Schulz, S. A. *et al.* Roadmap on photonic metasurfaces. *Applied Physics Letters* **124** 260701 (2024).

- Yang, J., Xiao X., Flórez, J., Gemmell, N., Dichtl, P., Gennaro, S.D., Maier, S.A., Phillips, C.C., Clark, A.S. and Oulton, R.F. Stimulated emission tomography of spontaneous four-wave mixing in plasmonic nanoantennas. *ACS Photonics* (Under review)

Acknowledgements

This thesis is the result of contributions from a countless group of people. As I am unable to list all the names in these acknowledgements, I extend my sincerest apologies to those who were not mentioned, and I look forward to thanking you personally in the near future.

Words are truly not enough to express my gratitude to my main supervisor, Prof. Rupert Oulton. Thank you, Rupert, for your infinite patience and invaluable guidance. I will always appreciate how you pushed me when I needed to be pushed and supported me when I needed help, and it was the greatest comfort knowing that you were always on my side. Thank you also to my co-supervisor Dr. Alex Clark, whose infectious optimism and skills in the laboratory I respect deeply. It is thanks to you that I became involved in the nonlinear optics project in the very beginning, and I will always remember how you were able to align in one hour the 4f system that I was struggling with for one week.

I would also like to thank Prof. Myungshik Kim for giving me the opportunity to join the Quantum Systems Engineering CDT program as well as all the lecturers, admins, and colleagues in the program who made learning physics enjoyable. Thank you as well to Juraci Didone and Carolyn Dale in the EXSS admin office and Loli Sanchez in the postgraduate office for always supporting us students so that we can focus on research.

A special thank you goes out to those who helped me endure the loneliness of Blackett 1015—Jefferson Florez for his warm companionship and introducing me to salsa, Toby Severs for his delightful personality and helpful insights, Xiaofei Xiao for his positivity and tireless work ethic, and Paul Dichtl for helping me get started when I fell in the deep end. Thank you as well to Nathan Gemmell, Ming Fu, and Toby for your contributions to the critical coupling and SET projects, and all my other colleagues in the research group and H722 office for creating a welcoming and fun atmosphere.

Thank you to my beloved mother, father, and sister for always reminding me that I have a home to come to. I would not have been able to leave for another country to do

a PhD without your love and constant support. A big thank you to Robert Shaw, Rode Filgueira, Tekla Virag, and Schweiny at William Temple House for giving me a home away from home. Thank you as well to all my loved ones at WTH, Dom, Woojin, Jaro, Juan, Mensah, Keerthana, Blake, Eldad, Andra, Anelise, Chris, Marine, and all the others for forming my London family. My deepest love and gratitude to Wookhwan, Alis, and Joel for comforting me and giving me hope during the most difficult time of my life. Last, but certainly not least, thank you to my girlfriend Alizée for witnessing all the moments and being my light until the very end.

Contents

List of Tables **11**

List of Figures **13**

List of Acronyms **14**

1 Introduction **15**

1.1 Outline of thesis 17

2 Nonlinear Optics **19**

2.1 Linear optics 19

2.1.1 Lorentz oscillator model 20

2.1.2 Electromagnetic wave equation 22

2.1.3 Refractive index and dispersion 23

2.2 Nonlinear susceptibility and polarisation 24

2.2.1 Coupled wave equations 25

2.3 Second harmonic generation 26

2.4 Third-order processes 30

2.4.1 Third harmonic generation 30

2.4.2 Four-wave mixing 31

2.5 Conclusion 32

3 Plasmonics **34**

3.1 Background 34

3.1.1 Helmholtz equation and boundary conditions 35

3.1.2 Dielectric function of the free electron gas 36

3.2 Surface plasmon polaritons 38

3.3 Localised surface plasmons . . . 43
3.4 Conclusion . . . 45

4 Optical Properties of Nanoantennas for Nonlinear Optics 47
4.1 Background . . . 47
4.1.1 Nonlinear optics via reciprocity . . . 48
4.1.2 Multi-resonant antennas . . . 50
4.1.3 Nanofocusing and coupling bright and dark modes . . . 53
4.2 Waveguide resonator and dimer . . . 55
4.2.1 Electric field enhancement and mode overlap . . . 56
4.2.2 Polarisation . . . 60
4.3 Bar and discs . . . 61
4.3.1 Electric field profile and transmission . . . 63
4.4 Conclusion . . . 65

5 Frequency Mixing in Critically Coupled Nanoantennas 67
5.1 Coupled oscillator model . . . 68
5.1.1 Critical coupling condition . . . 70
5.1.2 Extracting fitted parameters . . . 71
5.2 SHG and THG measurements . . . 73
5.2.1 SHG and THG dependence on dimer displacement . . . 75
5.2.2 Pumping with off-axis polarisations . . . 77
5.3 Conclusion . . . 79

6 Four-Wave Mixing in Plasmonic Nanoantennas 81
6.1 Background and motivation . . . 82
6.1.1 The case for spontaneous four-wave mixing . . . 82
6.1.2 Stimulated emission tomography . . . 84
6.1.3 Summary . . . 85
6.2 Sample and experimental setup . . . 85
6.2.1 Dual-beam setup . . . 87
6.3 Observation of four-wave mixing . . . 89
6.3.1 Delay shift with wavelength tuning . . . 92
6.3.2 JSD characterisation . . . 95

6.4 Estimating SFWM generation rate 96
6.5 Conclusion 101

7 Conclusion **103**
7.1 Summary 103
7.2 Outlook 104

References **107**

List of Tables

6.1 Experimental parameters for SFWM generation rates. 100
6.2 SFWM photon-pair generation rates 101

List of Figures

2.1 Diagram of a Lorentz oscillator 21
2.2 Second harmonic generation 27
2.3 Third harmonic generation 30
2.4 Four-wave mixing 31

3.1 Theoretical and experimental values for the dielectric function for gold . . 38
3.2 Geometry of metal-dielectric interface 39
3.3 Surface plasmon polaritons 42
3.4 Localised surface plasmons 43

4.1 Nonlinear scattering theory for SHG 49
4.2 Enhanced SHG in multiresonant plasmonic nanoantenna 52
4.3 Examples of nanofocusing configuration 53
4.4 Coupling bright and dark resonators 54
4.5 Waveguide resonator and dimer nanoantenna 56
4.6 Simulated field enhancement at fundamental wavelength for waveguide resonator and dimer 57
4.7 Simulated field enhancement at fundamental wavelength for coupled waveguide-dimer 57
4.8 Simulated field enhancement at second harmonic wavelength for coupled waveguide-dimer 58
4.9 Simulated field enhancement at third harmonic wavelength for coupled waveguide-dimer 58
4.10 Field enhancement, mode overlap, and transmission for coupled waveguide-dimer according to displacement 60
4.11 Field enhancement according to polarisation for different dimer displacements 61

4.12 Bar-discs nanoantenna for SHG 62
4.13 Simulated field profiles at fundamental wavelength for bar-discs nanoantenna 64
4.14 Simulated field profiles at second harmonic wavelength for bar-discs nanoantenna 64
4.15 Simulated transmission of bar-discs nanoantenna 65

5.1 Three-level model for coupled waveguide-dimer system 68
5.2 Extraction of critical coupling parameters 72
5.3 Experimental setup for SHG/THG measurements 74
5.4 Observation of SHG/THG in waveguide-dimer nanoantenna 75
5.5 Predicted and measured SHG/THG intensity according to dimer displacement 76
5.6 Polarisation series for SHG 78
5.7 Polarisation series for THG 78

6.1 Energy level diagrams for SFWM and SPDC 83
6.2 Bar-discs nanoantenna 86
6.3 Experimental setup for four-wave mixing 88
6.4 Spectra of nonlinear processes in bar-discs nanoantenna 90
6.5 Power series of nonlinear processes in bar-discs nanoantenna 91
6.6 Delay shift according to pump/seed wavelength 93
6.7 Optimum delay for peak FWM signal according to pump/seed wavelength 95
6.8 Joint spectral density 96
6.9 Extinction of bar-discs nanoantenna 99

List of Acronyms

FDTD finite-difference time-domain

FWM four-wave mixing

FWHM full width at half maximum

LSP localised surface plasmon

JSD joint spectral density

OPO optical parametric oscillator

QST quantum state tomography

SHG second harmonic generation

SFWM spontaneous four-wave mixing

SPDC spontaneous parametric down-conversion

SET stimulated emission tomography

SFG sum-frequency generation

SPP surface plasmon polariton

THG third harmonic generation

Chapter 1

Introduction

Although nonlinear optical effects were first studied well over a century ago [1], significant research into the field was only made possible by the invention of the laser in 1960 [2]. The high intensity provided by lasers was necessary to drive intrinsically weak nonlinear responses [3], and the field of nonlinear optics formally began with the demonstration of second harmonic generation (SHG) in 1961 [4] followed not long after by third harmonic generation (THG) in 1962 [5]. Following these achievements, nonlinear optics expanded rapidly with observations of countless nonlinear processes and discoveries of diverse applications ranging from the damage-negating amplification of laser pulses by chirped pulse amplification [6] to the generation of heralded single photons by spontaneous parametric down-conversion (SPDC) [7] and spontaneous four-wave mixing (SFWM) [8].

At first, the study of nonlinear interactions was limited to macroscopic volumes in bulk nonlinear crystals. At the time, the strategy was to maximise the conversion of nonlinear processes by increasing the interaction volume between the incident light and nonlinear medium. In practice, however, this approach is fundamentally limited by the simultaneous accumulation of a phase mismatch between interacting fields [3, 9, 10]. As

a result, there was significant interest during the early stages of nonlinear optics research in demonstrating efficient phase-matching in various materials [11–14].

Significant obstacles exist, however, to these traditional approaches to nonlinear optics. For one, the extreme precision and range of controls required for phase-matching necessitates complex setups [15] or difficult growth and fabrication techniques [16]. Although researchers are currently able to achieve superior nonlinear conversion efficiencies using these techniques, they are prohibitively cumbersome in today's nanoscale platforms. Moreover, bulk nonlinear optics is limited in the materials that are available for use as phase-matching is only available for a narrow range of materials possessing specific optical properties [3].

The modern metamaterial paradigm completely removes these obstacles. Today, researchers are able to produce a range of metamaterials that display exotic optical properties with nanoscale resolution, which was made possible by the rapid development of fabrication techniques in the semiconductor industry [17–19]. The building blocks of these metamaterials consist of metal and/or dielectric nanostructures whose individual and collective geometries can be tailored to meet specific needs [20]. This is in line with current trends towards compact nanoscale devices that facilitate light-matter interactions at subwavelength scales resulting in phase-matching requirements being relaxed or disregarded completely [15].

To overcome the inherent weakness of nonlinear interactions in such small volumes, today's researchers rely on strong confinement and enhancements of fields by exploiting various resonant properties in modern nanoantennas [21]. This thesis is a continuation of these efforts, and in the following chapters, we will present experimental work that aims to further our understanding of modern nanoantenna designs and working principles.

1.1 Outline of thesis

The thesis will be presented as follows:

- Chapter 2 covers the fundamental concepts of nonlinear optics including the origin of the nonlinear response of light-matter interaction. We will cover the nonlinear processes of second harmonic generation, third harmonic generation, and four-wave mixing which will be experimentally investigated in Chapters 5 and 6.

- Chapter 3 introduces key principles of plasmonics, including surface plasmon polariton and localised surface plasmon modes. We will discuss plasmonic phenomena such as electric field confinement and enhancement which will aid the understanding of the plasmonic nanoantennas to be used in the experimental chapters.

- Chapter 4 discusses the key features of effective nanoantennas for nonlinear optical applications through informative examples in recent literature in order to provide motivation for the design of our own nanoantennas. We then present simulation studies of two novel plasmonic nanoantenna designs demonstrating these features in order to better understand their working principles.

- Chapter 5 presents an experimental investigation of a coupled waveguide and dimer nanoantenna. We explore the geometric parameter of the nanoantenna that controls coupling in order to demonstrate a critical coupling condition via SHG and THG measurements.

- Chapter 6 is an experimental study of a second plasmonic nanoantenna, the coupled bar and discs. We demonstrate four-wave mixing in individual nanoantennas and perform a stimulated emission tomography analysis to assess its ability to generate correlated photon pairs via spontaenous four-wave mixing.

- Chapter 7 summarises the experimental results and provides commentary with an outlook to future studies to continue the work presented in this thesis.

Chapter 2

Nonlinear Optics

In this chapter, we will cover the foundations of nonlinear optics including the origin of the nonlinear response and the mechanism behind key nonlinear optical processes demonstrated in this thesis. As a full survey of nonlinear optics is beyond the scope of this thesis, we will limit ourselves to the relevant aspects that will support our discussions in the following chapters. The derivations in this chapter primarily follow the ones presented in Reference [9] and are supplemented by Reference [3] and relevant literature.

2.1 Linear optics

We begin in the realm of linear optics which assumes a linear response of the electric polarisation $\boldsymbol{P}$ of a material to the electric field $\boldsymbol{E}$ according to

$$\boldsymbol{P} = \varepsilon_0 \chi^{(1)} \boldsymbol{E} \ , \tag{2.1}$$

where ε_0 is the vacuum permittivity and $\chi^{(1)}$ is the linear optical susceptibility. Here, $\chi^{(1)}$ is actually a second-rank tensor, with the higher-order susceptibilities to be discussed

later, $\chi^{(n)}$, being a tensor of rank $n+1$. However, for simplicity, we will consider the scalar form in this chapter without any loss of generality. Equation 2.1 is found to be a good description of light-matter interaction in the presence of weak fields and is sufficient to explain linear optical phenomenon such as refraction and reflection [10]. We can further define the displacement vector $\boldsymbol{D}$ which accounts for both the polarisation and the external field as

$$\boldsymbol{D} = \varepsilon_0 \boldsymbol{E} + \boldsymbol{P} = \varepsilon_0 (1 + \chi^{(1)}) \boldsymbol{E} = \varepsilon_0 \varepsilon_r \boldsymbol{E}, \tag{2.2}$$

where we have defined the relative permittivity (or dielectric constant) as $\varepsilon_r = 1 + \chi^{(1)}$. As light is an electromagnetic wave, its interaction with a material is governed by the Lorentz force law,

$$\boldsymbol{F} = q(\boldsymbol{E} + \boldsymbol{v} \times \boldsymbol{B}) \ , \tag{2.3}$$

where q is the charge of a particle moving with velocity $\boldsymbol{v}$ in a magnetic field $\boldsymbol{B}$. The magnitude of the magnetic field is defined as $|\boldsymbol{B}| = |\boldsymbol{E}|/c$, with c being the speed of light, and for $v \ll c$ this may safely be neglected. In a dielectric material, electrons are bound to the nucleus and their response to an electric field is described by the interaction of the field with the least bound electron with charge e, and Equation 2.3 reduces to

$$\boldsymbol{F} = -e\boldsymbol{E} \ . \tag{2.4}$$

2.1.1 Lorentz oscillator model

The classic way of modelling this situation is to consider the electron bound to the nucleus by a spring with a damping constant γ as shown in Figure 2.1. This is known as the Lorentz oscillator model and we will continuously be returning to this model throughout

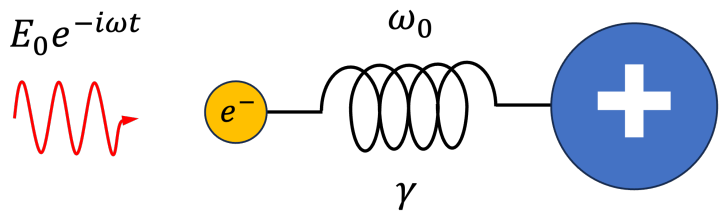


Figure 2.1: **Diagram of a Lorentz oscillator**. The electron is bound to a heavy nucleus by a spring with resonance ω_0 and damping γ. An external field acts as a driving force leading to the electron oscillating as a dipole.

this thesis. For simplicity, we consider the equation of motion in a single dimension x, and for a time-varying electric field $E(t) = E_0 e^{-i\omega t}$ we have

$$\ddot{x}(t) + \gamma\dot{x}(t) + \omega_0^2 x(t) = -\frac{e}{m}E_0 e^{-i\omega t} \ , \tag{2.5}$$

where we have substituted Equation 2.4, and ω_0 is the natural frequency of oscillation and m is the mass of the electron. If we assume that x has the same temporal dependence as the driving field and takes the form $x(t) = x_0 e^{-i\omega t}$, Equation 2.5 gives us

$$x(t) = \frac{-eE_0 e^{-i\omega t}}{m(\omega_0^2 - \omega^2 - i\gamma\omega)} \ . \tag{2.6}$$

The displaced electron acts as a time varying dipole $d(t) = -ex(t)$, and if we define the polarisation as the dipole moment per unit space we have

$$P = Nd(t) = \frac{e^2 N}{m}\frac{E_0 e^{-i\omega t}}{\omega_0^2 - \omega^2 - i\gamma\omega} \ , \tag{2.7}$$

where N is the dipole number density in a given material and is typically on the order of 10^{23} in solids [10]. As we can see in Equation 2.7, the polarisation oscillates at the same frequency as the driving field with a proportional amplitude, $|P| \propto |E|$. We now relate

Equation 2.7 to Equation 2.1 to redefine the linear optical susceptibility as

$$\chi^{(1)} = \frac{e^2 N}{\varepsilon_0 m} \frac{1}{\omega_0^2 - \omega^2 - i\gamma\omega} = \frac{\omega_p^2}{\omega_0^2 - \omega^2 - i\gamma\omega} \ , \tag{2.8}$$

where

$$\omega_p = \sqrt{\frac{e^2 N}{\varepsilon_0 m}} \tag{2.9}$$

is called the plasma frequency and will be revisited in Chapter 3 to discuss its significance.

2.1.2 Electromagnetic wave equation

In order to derive the electromagnetic wave equation which will describe the nonlinear optical processes in later sections, we turn to Maxwell's equations which read

$$\nabla \cdot \boldsymbol{D} = \rho \tag{2.10a}$$

$$\nabla \cdot \boldsymbol{B} = 0 \tag{2.10b}$$

$$\nabla \times \boldsymbol{E} = -\frac{\partial \boldsymbol{B}}{\partial t} \tag{2.10c}$$

$$\nabla \times \boldsymbol{H} = \frac{\partial \boldsymbol{D}}{\partial t} + \boldsymbol{J} \ , \tag{2.10d}$$

where ρ is the external charge and $\boldsymbol{J}$ the external current density. Recall that $\boldsymbol{D} = \varepsilon_0 \boldsymbol{E} + \boldsymbol{P}$ (Eq. 2.2) and $\boldsymbol{H} = \frac{1}{\mu_0}\boldsymbol{B} - \boldsymbol{M}$, where μ_0 is the vacuum permeability. Throughout this thesis, we only consider non-magnetic media and thus $\boldsymbol{M} = 0$. Let us first consider the case of a vacuum in the absence of polarisation ($\boldsymbol{P} = 0$) and any external charge ($\rho = 0$) or current ($\boldsymbol{J} = 0$). Taking the curl of both sides of Equation 2.10c and making

the relevant substitutions yields

$$\nabla \times (\nabla \times \boldsymbol{E}) = \nabla \times \left(-\frac{\partial \boldsymbol{B}}{\partial t} \right) = -\varepsilon_0 \mu_0 \frac{\partial^2 \boldsymbol{E}}{\partial t^2} \ , \tag{2.11}$$

and we can make use of the vector identity $\nabla \times (\nabla \times \boldsymbol{E}) = \nabla(\nabla \cdot \boldsymbol{E}) - \nabla^2 \boldsymbol{E}$ to arrive at the desired result,

$$\nabla^2 \boldsymbol{E} = \varepsilon_0 \mu_0 \frac{\partial^2 \boldsymbol{E}}{\partial t^2} = \frac{1}{c^2} \frac{\partial^2 \boldsymbol{E}}{\partial t^2} \ , \tag{2.12}$$

where the speed of light in a vacuum is defined as $c = 1/\sqrt{\varepsilon_0 \mu_0}$. For the more general case we are interested in of light propagating through an isotropic medium, we once again make use of Equation 2.1 to recast Equation 2.12 as

$$\nabla^2 \boldsymbol{E} = \mu_0 \frac{\partial^2}{\partial t^2} (\varepsilon_0 \boldsymbol{E} + \boldsymbol{P}) \ . \tag{2.13}$$

We will return to Equation 2.13 in the following section to derive the coupled wave equations that describe the interaction of different fields in a nonlinear process.

2.1.3 Refractive index and dispersion

Equation 2.13 describes an electromagnetic wave travelling through a medium with velocity $v = 1/\sqrt{\varepsilon_0 \mu_0 (1 + \chi^{(1)})} = c/\sqrt{1 + \chi^{(1)}}$. The ratio of the speed of light in a vacuum and a medium is called the refractive index and is defined as

$$n = \frac{c}{v} = \sqrt{1 + \chi^{(1)}} = \sqrt{\varepsilon_r} \ . \tag{2.14}$$

As we have seen in Equation 2.8, $\chi^{(1)}$ is a function of the frequency of the EM wave, so the refractive index must also vary with frequency, and this phenomenon is known as

dispersion. Equation 2.8 also shows $\chi^{(1)}$ to be complex-valued, and by extension we can decompose the refractive index (and dielectric constant) into real and imaginary parts as

$$n(\omega) = n_r(\omega) + in_i(\omega) \ . \tag{2.15}$$

Here, $n_r(\omega)$ is related to the wave propagation and $n_i(\omega)$ is related to the absorption in a given material, a concept we will revisit in Chapter 3. When ω is close to ω_0, $\frac{\partial n}{\partial \omega} < 0$ and is called anomalous dispersion, while when ω is far from ω_0, $\frac{\partial n}{\partial \omega} > 0$ and is called normal dispersion. It is important to keep in mind that the refractive index varies with frequency, as dispersion plays a crucial role when considering light-matter interactions over a range of frequencies as we will see in the nonlinear experiments of later chapters.

2.2 Nonlinear susceptibility and polarisation

In the previous section, we claimed that the linear polarisation provides a good description of light-matter interaction for weak fields, and were thus able to effectively model the situation with the Lorentz oscillator model of an electron trapped in a harmonic potential with a linear restoring force. However, we can no longer make this assumption for the very high electric fields present in lasers, and thus we rewrite Equation 2.1 as a Taylor series expansion in terms of the electric field,

$$\boldsymbol{P} = \varepsilon_0 \left(\chi^{(1)} \boldsymbol{E} + \chi^{(2)} \boldsymbol{E}^2 + \chi^{(3)} \boldsymbol{E}^3 + \ldots \right) \ . \tag{2.16}$$

At this point, we make a crucial observation about the symmetry of the second-order term in Equation 2.16. The equation tells us that the second-order polarisation is the

same whether we have a positive or negative field. However, this contradicts the property of centrosymmetric materials that requires $P(-E) = -P(E)$. As a result, the second-order polarisation term must vanish, and second-order (and by extension all even-order) nonlinear effects are prohibited in centrosymmetric materials. As we shall see in later discussions, there are multiple exceptions to this restriction, particularly in the realm of metamaterials, but this is a good principle to keep in mind when investigating nonlinear optics.

2.2.1 Coupled wave equations

We are now ready to derive the coupled wave equations governing nonlinear processes. For simplicity, we restrict ourselves to the case of a plane wave propagating in the z-direction, but the insights we will gain here can be generalised to 3-dimensional cases. We rewrite Equation 2.13 in scalar form to

$$\frac{\partial^2 E}{\partial z^2} - \mu_0 \varepsilon_0 \frac{\partial^2 E}{\partial t^2} = \mu_0 \frac{\partial^2 P}{\partial t^2} \ , \tag{2.17}$$

where we can consider the polarisation term P to be acting as a source of oscillating dipoles which generates new frequencies. It is helpful to separate Equation 2.16 in scalar form into linear and nonlinear components as

$$\begin{aligned} P &= \varepsilon_0 \chi^{(1)} E + \varepsilon_0 \chi^{(2)} E^2 + \varepsilon_0 \chi^{(3)} E^3 + \dots \\ &= P^{\mathrm{L}} + P^{\mathrm{NL}} \ . \end{aligned} \tag{2.18}$$

In anticipation of the new frequencies to be generated, we also express $E(z,t)$ and $P(z,t)$ as the sum of n discrete frequency components,

$$E(z,t) = \sum_n \frac{1}{2}\left(\tilde{E}_n(z)e^{i(\omega_n t - k_n z)} + \text{c.c.}\right) \tag{2.19a}$$

$$P(z,t) = \sum_n \frac{1}{2}\left(\tilde{P}_n(z)e^{i(\omega_n t - k_n z)} + \text{c.c.}\right) \ . \tag{2.19b}$$

Substituting the n^{th} components of Equation 2.19 into Equation 2.17 and restricting our focus to the generated nonlinear polarisation P^{NL} yields

$$\frac{\partial \tilde{E}_n}{\partial z} = \frac{-i\mu_0\omega_n^2}{2k_n}\tilde{P}^{\text{NL}}(z) = \frac{-i\omega_n}{2\varepsilon_0 c n_n}\tilde{P}_n^{\text{NL}}(z) \ , \tag{2.20}$$

where we have assumed the slowly varying envelope approximation ($\frac{\partial^2 \tilde{E}_n}{\partial z^2} \approx 0$) to simplify the derivation. Equation 2.20 describes the evolution of the electric field $\tilde{E}_n(z)$ as it propagates through a nonlinear medium and its relationship to the nonlinear polarisation $\tilde{P}_n^{\text{NL}}(z)$. This is the starting point for understanding any nonlinear optical process, and the derivation of $\tilde{P}_n^{\text{NL}}(z)$ for all n frequency components involved in a process will yield a set of coupled wave equations that fully characterise it.

2.3 Second harmonic generation

It is worth deriving the coupled wave equations to gain insights about a nonlinear process, and we will do this for the simplest case of SHG as we investigate this process in multiple experiments in later chapters. In SHG, two pump photons at the fundamental frequency ω are annihilated to produce a signal photon at the second harmonic frequency 2ω as shown in Figure 2.2. As such, we consider Equation 2.20 for the case where $n = 2$,

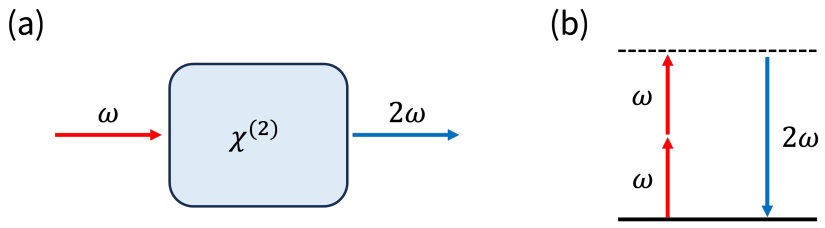


Figure 2.2: **Second harmonic generation**. **(a)** Illustration of SHG in a $\chi^{(2)}$ material. **(b)** Energy level diagram for SHG showing two photons at the fundamental frequency ω being annihilated to produce a photon at the second harmonic frequency 2ω.

$$\frac{\partial \tilde{E}_\omega}{\partial z} = \frac{-i\omega}{2\varepsilon_0 c n_\omega} \tilde{P}^{\mathrm{NL}}(z) \tag{2.21a}$$

$$\frac{\partial \tilde{E}_{2\omega}}{\partial z} = \frac{-i\omega}{\varepsilon_0 c n_{2\omega}} \tilde{P}^{\mathrm{NL}}(z) \ , \tag{2.21b}$$

and Equation 2.19 reads

$$E(z,t) = \frac{1}{2}\left(\tilde{E}_\omega e^{i(\omega t - k_\omega z)} + \tilde{E}_{2\omega} e^{i(2\omega t - k_{2\omega} z)} + \text{c.c.}\right) \tag{2.22a}$$

$$P^{\mathrm{NL}}(z,t) = \frac{1}{2}\left(\tilde{P}^{\mathrm{NL}}_\omega e^{i(\omega t - k_\omega z)} + \tilde{P}^{\mathrm{NL}}_{2\omega} e^{i(2\omega t - k_{2\omega} z)} + \text{c.c.}\right) \ . \tag{2.22b}$$

We also use Equation 2.18 to express the second-order nonlinear polarisation as

$$\begin{aligned} P^{\mathrm{NL}}(z,t) &= \varepsilon_0 \chi^{(2)} E^2(z,t) \\ &= \frac{1}{4}\varepsilon_0 \chi^{(2)} \left(\tilde{E}_\omega e^{i(\omega t - k_\omega z)} + \tilde{E}_{2\omega} e^{i(2\omega t - k_{2\omega} z)} + \text{c.c.}\right)^2 \ . \end{aligned} \tag{2.23}$$

The next step is to expand Equation 2.23 and collect all terms of ω and 2ω, while discarding the others that are not relevant. Once we have done this, we can relate the collected terms to Equation 2.22b to re-express the fundamental and second harmonic terms of the

nonlinear polarisation as

$$\tilde{P}_{\omega}^{\mathrm{NL}}(z) = \varepsilon_0 \chi^{(2)} \left(\tilde{E}_{2\omega} \tilde{E}_{\omega}^{*} e^{-i(k_{2\omega} - 2k_{\omega})z} \right) \tag{2.24a}$$

$$\tilde{P}_{2\omega}^{\mathrm{NL}}(z) = \frac{1}{2} \varepsilon_0 \chi^{(2)} \left(\tilde{E}_{\omega}^{2} e^{i(k_{2\omega} - 2k_{\omega})z} \right) \ . \tag{2.24b}$$

Note the expression $k_{2\omega} - k_{\omega}$ in both equations, which is the origin of the phase mismatch mentioned in Chapter 1 and shall henceforth be referred to as Δk. We will return to the significance of Δk in the discussion below. We are now ready to fully express the coupled wave equations for SHG by substituting Equation 2.24 into Equation 2.21,

$$\frac{\partial \tilde{E}_{\omega}}{\partial z} = \frac{-i\omega\chi^{(2)}}{2cn_{\omega}} \tilde{E}_{2\omega} \tilde{E}_{\omega}^{*} e^{-i\Delta k z} \tag{2.25a}$$

$$\frac{\partial \tilde{E}_{2\omega}}{\partial z} = \frac{-i\omega\chi^{(2)}}{2cn_{2\omega}} \tilde{E}_{\omega}^{2} e^{i\Delta k z} \ . \tag{2.25b}$$

We can summarise the significance of Equation 2.25 with three key observations.

First, Equation 2.25a tells us that the growth of the fundamental field $\tilde{E}_{\omega}$ is dependent on the second harmonic field $\tilde{E}_{2\omega}$. This is to be expected, as in the photon picture described above, two pump photons are annihilated for every second harmonic photon generated, and the pump becomes depleted with SHG growth. In practice, for very low SHG efficiencies ($\eta_{\mathrm{SHG}} = I_{2\omega}/I_{\omega} \ll 1$), which are generally the case for experiments involving nanostructures, we treat the pump as being un-depleted and Equation 2.25a is equal to zero.

Second, Equation 2.25b states that the growth of the second harmonic field is dependent on $\tilde{E}_{\omega}^{2}$. This is the origin of the quadratic relationship between the intensity of a measured SHG signal and the intensity of the pump beam used to generate it. In our

experiments in future chapters, we will make use of this property to validate our measured SHG signals as genuine by performing a power series with respective to the pump.

Finally, as stated before there is a phase difference Δk between $\tilde{E}_{2w}$ and $\tilde{E}_w$. This had in fact already been predicted by Equation 2.15 when we discussed the refractive index being frequency-dependent, and the two waves cannot be expected to travel with the same phase velocity. In the low pump depletion approximation, we can solve Equation 2.25 to express the intensity of the generated second harmonic field as

$$I_{2\omega}(L) \propto I_{\omega}^2 L^2 \mathrm{sinc}^2(\frac{\Delta k L}{2}) \ , \tag{2.26}$$

where I_ω is the intensity of the pump beam at the fundamental frequency ω and L is the length of the path travelled through a nonlinear medium. In order to maximise $I_{2\omega}$ and grow the second harmonic field, we would like $\Delta k = 0$, which can be achieved via a technique called phase-matching. This typically involves the use of carefully oriented birefringent crystals with different refractive indices in orthogonal directions to induce a phase difference via polarisation control that negates Δk. However, one of the biggest advantages of nanoscale nonlinear optics is that we work in sub-wavelength domains where $L \sim \lambda$, and this allows us to safely relax the phase-matching restrictions that are placed on traditional bulk nonlinear optics. Of course, this comes at a significant cost to the conversion efficiency, and a great deal of research is dedicated to compensating for this fact by engineering nanostructures with the highest nonlinearity possible. In the experiments presented in this thesis, we will not be taking phase-matching into account, and thus we will not elaborate on this topic any further.

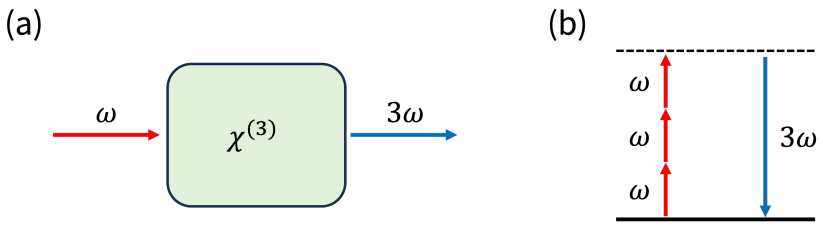


Figure 2.3: **Third harmonic generation**. **(a)** Illustration of THG in a $\chi^{(3)}$ material. **(b)** Energy level diagram for THG showing three photons at the fundamental frequency ω being annihilated to produce a photon at the third harmonic frequency 3ω.

2.4 Third-order processes

Third-order processes involve looking at the third-order term of the nonlinear polarisation in Equation 2.16,

$$\boldsymbol{P}^{(3)} = \varepsilon_0 \chi^{(3)} \boldsymbol{E}^3 \ , \tag{2.27}$$

for the frequencies of interest. It is straightforward to extend the detailed treatment we have given SHG to third- and higher-order processes, although this comes at the cost of collecting an exponentially increasing number of terms for the coupled wave equations for the different frequencies involved. As such we will simply summarise the key points of two additional nonlinear processes which we will be investigating in this thesis, THG and four-wave mixing (FWM).

2.4.1 Third harmonic generation

Similar to SHG, THG involves the annihilation of three pump photons at the fundamental frequency ω to produce a photon at frequency 3ω as shown in Figure 2.3. As such, the interaction still involves two distinct frequencies, and the coupled wave equations for

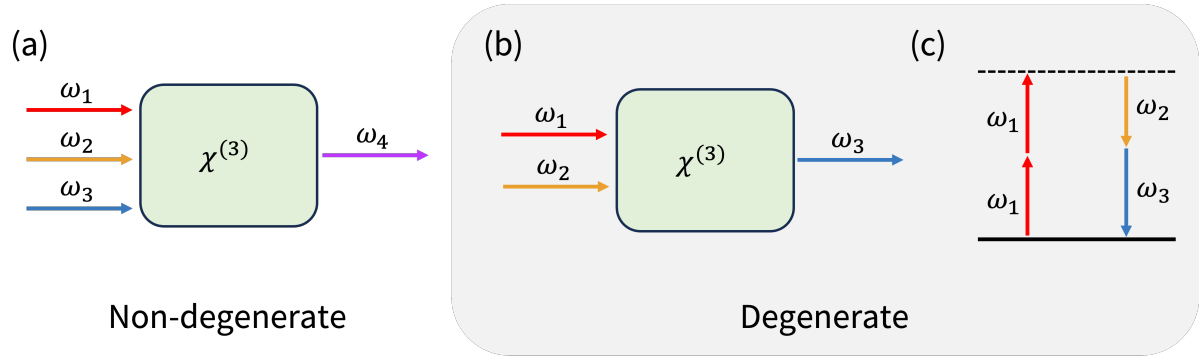


Figure 2.4: **Four-wave mixing**. **(a)** Illustration of non-degenerate FWM. **(b)** Illustration of degenerate FWM. **(c)** Energy level diagram for degenerate FWM.

third-harmonic generation read

$$\frac{\partial \tilde{E}_\omega}{\partial z} = \frac{3i\omega\chi^{(3)}}{8cn_\omega}\tilde{E}_{3\omega}\tilde{E}_\omega^{*2}e^{i\Delta kz} \tag{2.28a}$$

$$\frac{\partial \tilde{E}_{3\omega}}{\partial z} = \frac{3i\omega\chi^{(3)}}{8cn_{3\omega}}\tilde{E}_\omega^{3}e^{-i\Delta kz} \ . \tag{2.28b}$$

Similar to the case with SHG, Equation 2.28b tells us that the growth of the third harmonic field $\tilde{E}_{3\omega}$ depends on $\tilde{E}_\omega^3$ and we can expect a cubic dependence of a measured THG signal on the pump.

2.4.2 Four-wave mixing

Four-wave mixing, as the name implies, is a third-order process involving four distinct fields. The more general case of FWM is known as non-degenerate four-wave mixing and is illustrated in Figure 2.4a. Here, three photons with distinct frequencies $\omega_1 \neq \omega_2 \neq \omega_3$ interact in a $\chi^{(3)}$ medium to produce a fourth photon that can take on any one of 8 new frequencies $\pm\omega_1 \pm \omega_2 \pm \omega_3$. As each of these processes would require its own energy level diagram, we do not present one here.

A special case of non-degenerate FWM is degenerate FWM where two of the three

previously distinct frequencies are degenerate. As we will be interested in this case of FWM in our experiments, we will evaluate it in more detail and all future mentions of FWM in this thesis will refer to degenerate FWM. Here, two photons of frequency ω_1 interact with a photon of frequency ω_2 to produce a photon of frequency $\omega_3 = 2\omega_1 - \omega_2$. This situation is illustrated with a corresponding energy level diagram in Figure 2.4b and c. Here, the coupled wave equations read

$$\frac{\partial \tilde{E}_1}{\partial z} = \frac{-3i\omega_1\chi^{(3)}}{16cn_1}\tilde{E}_2\tilde{E}_3\tilde{E}_1^* e^{i\Delta kz} \tag{2.29a}$$

$$\frac{\partial \tilde{E}_2}{\partial z} = \frac{-3i\omega_2\chi^{(3)}}{16cn_2}\tilde{E}_1^2\tilde{E}_3^* e^{-i\Delta kz} \tag{2.29b}$$

$$\frac{\partial \tilde{E}_3}{\partial z} = \frac{-3i\omega_3\chi^{(3)}}{16cn_3}\tilde{E}_1^2\tilde{E}_2^* e^{-i\Delta kz} \tag{2.29c}$$

Once again, we turn to Equation 2.29c to give us insight into the growth of the four-wave mixing field $\tilde{E}_3$. In this instance, we see that it has a quadratic dependence on the pump field $\tilde{E}_1$ and a linear dependence on the second field $\tilde{E}_2$, and we will use this to confirm our FWM measurements in later chapters.

2.5 Conclusion

We have now laid the foundations of nonlinear optics we will need to discuss the physics presented in this thesis. We began with the fundamental properties of linear optics and have seen how the Lorentz oscillator model can describe the the interaction of light as an electromagnetic wave with matter. We then generalised our definition of the polarisation to include terms that are nonlinear with the electric field and have used this definition to derive the coupled wave equations that govern the interaction of related fields in a non-

linear optical process. We have used the coupled wave equations to gain insights on SHG, THG, and FWM, namely that these processes grow with varying degrees of dependency on the fundamental field. In the following chapter, we will discuss the fundamentals of plasmonics, to see how we can enhance these fields and support our discussions of the nonlinear experiments to be presented in Chapters 4–6.

Chapter 3

Plasmonics

In this chapter, we will cover the fundamentals of plasmonics and the origin of local field enhancements in plasmonic structures. We also discuss the two main manifestations of plasmonic modes, surface plasmon polaritons (SPPs) and localised surface plasmons (LSPs), as well as the use of plasmonic structures as nanoantennas. As in the previous chapter, we will limit our discussion to key principles that provide the motivation for the design of the plasmonic nanoantennas to be investigated in subsequent chapters. We will closely follow the derivations in Reference [22] and supplement this with relevant literature as necessary.

3.1 Background

Plasmonics is the study of the interaction between electromagnetic waves and the conduction electrons in metals as well as the interesting phenomena that arise as a result. It is a major driving force behind the field of nanophotonics that aims to control and confine light in sub-wavelength dimensions [22, 23]. Like the field of nonlinear optics, plasmonics is built on the foundations of classical physics and electromagnetism, and so we return to

Maxwell's equations which were first presented in Chapter 2.

3.1.1 Helmholtz equation and boundary conditions

We have already seen how Maxwell's equations (Eq. 2.10) can be combined to form the electromagnetic wave equation in a vacuum (Eq. 2.12). We once again assume a time-harmonic form of the electric field, $\boldsymbol{E}(\mathbf{r},t) = \boldsymbol{E}(\mathbf{r})e^{-i\omega t}$, and utilise the separation of variables to recast this in the form of the time-independent Helmholtz equation,

$$\nabla^2\boldsymbol{E}(\mathbf{r}) + k_0^2\varepsilon\boldsymbol{E}(\mathbf{r}) = 0 \ , \tag{3.1}$$

where $k_0 = \omega/c$ is the wavevector in a vacuum with frequency ω. Equation 3.1 is sufficient to describe the propagation of $\boldsymbol{E}$ in a homogeneous medium with permittivity ε. However, the effects of plasmonics are seen at the interface between a metal and dielectric, where the permittivity and permeability are spatially-dependent. In order to describe this, we must impose boundary conditions at the interface between two media as follows,

$$\boldsymbol{E}_{1,\parallel} - \boldsymbol{E}_{2,\parallel} = 0 \tag{3.2a}$$

$$\boldsymbol{H}_{1,\parallel} - \boldsymbol{H}_{2,\parallel} = \boldsymbol{J}_{\mathrm{s}} \times \hat{\boldsymbol{n}} \tag{3.2b}$$

where $\boldsymbol{J}_{\mathrm{s}}$ is the surface current density at the interface, $\hat{\boldsymbol{n}}$ is the unit normal vector to the interface, and $\boldsymbol{E}_{n,\parallel}$ and $\boldsymbol{H}_{n,\parallel}$ are the tangential components of the electric and magnetic field respectively for medium 1 and 2 at the interface. Provided that there are no external sources of current ($\boldsymbol{J}_{\mathrm{s}} = 0$), Equation 3.2 tells us that the tangential component of both the electric field and the magnetic at the interface must be continuous across the

boundary. This must be taken into account when solving the Helmholtz equation, and careful consideration must be given to the geometry and material properties of a given system.

3.1.2 Dielectric function of the free electron gas

Recall the Lorentz oscillator model discussed in Chapter 2.1 which yielded Equation 2.8 for the linear optical susceptibility. We rephrase this in terms of the permittivity (henceforth referred to as the dielectric function), which will be the most important parameter in describing all the optical phenomena discussed in this chapter,

$$\varepsilon = 1 + \chi^{(1)} = 1 + \frac{\omega_p^2}{\omega_0^2 - \omega^2 - i\gamma\omega} \ . \tag{3.3}$$

Also recall that we have previously defined the plasma frequency $\omega_p = \sqrt{e^2 N/\varepsilon_0 m}$ (Eq. 2.9), which we will now elaborate on further. Throughout this chapter, we will be viewing light-matter interaction under the Drude model which provides a good description of the optical properties of metals and is characterised by a free electron gas unbound by the nucleus and with number density N moving against a background of fixed positive ions. Here, ω_p is the characteristic frequency at which the free electrons collectively oscillate in response to an applied electric field, and we will be referring to this value repeatedly in the following discussions.

A crucial distinction between the Drude model and the model presented in Chapter 2 is that the electron is no longer bound to the nucleus, and as such we neglect the natural resonance frequency ω_0 which is related to the restoring force and rewrite Equation 3.3

as

$$\varepsilon(\omega) = 1 - \frac{\omega_p^2}{\omega^2 + i\gamma\omega} \ . \tag{3.4}$$

Equation 3.4 is the dielectric function of the free electron gas. Here, the damping term γ is now tied to the collisions between electrons as they oscillate, and it is related to the relaxation time of the electron gas τ as $\gamma = 1/\tau$. We have explicitly written it as a function of ω to remind ourselves that like the refractive index and optical susceptibility in Chapter 2, the dielectric function is dependent on the driving frequency. The real and imaginary parts of the complex dielectric function $\varepsilon(\omega) = \varepsilon_1(\omega) + i\varepsilon_2(\omega)$ are given by

$$\varepsilon_1(\omega) = 1 - \frac{\omega_p^2\tau^2}{1 + \omega^2\tau^2} \tag{3.5a}$$

$$\varepsilon_2(\omega) = \frac{\omega_p^2\tau}{\omega(1 + \omega^2\tau^2)} \ . \tag{3.5b}$$

We will now take a closer look at the dielectric function for different frequency ranges to gain further insights. First, we observe the behaviour at $\omega < \omega_p$ where the metallic characteristics of materials are preserved. For frequencies close to ω_p in this range, there is negligible damping and the dielectric function is mostly real,

$$\varepsilon(\omega) = 1 - \frac{\omega_p^2}{\omega^2} \ , \tag{3.6}$$

and the idealised model of a free electron gas is valid. For $\omega > \omega_p$, however, ε is mostly imaginary and we require a modification of the idealised dielectric constant to more accurately model real metals,

$$\varepsilon(\omega) = \varepsilon_\infty - \frac{\omega_p^2}{\omega^2 + i\gamma\omega} \ , \tag{3.7}$$

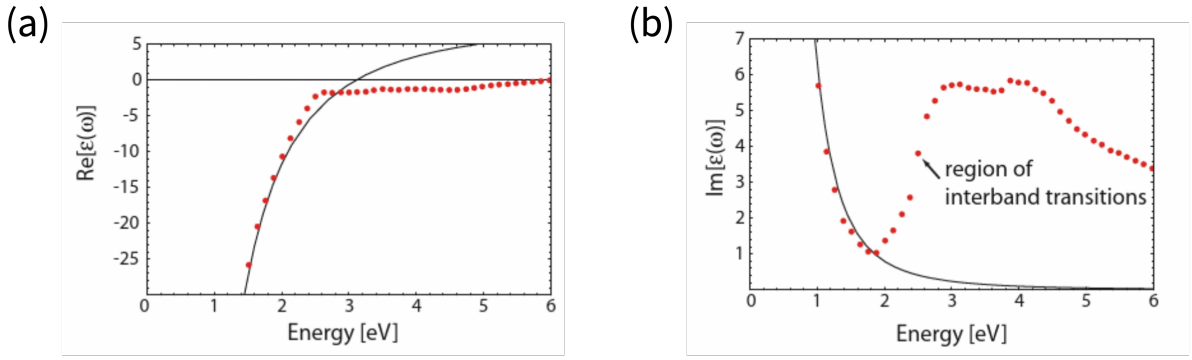


Figure 3.1: **Theoretical and experimental values for the dielectric function for gold**. **(a)** Real component of dielectric function. **(b)** Imaginary component of dielectric function showing the breakdown of theory near the region of interband transitions. The solid line indicates the theoretical model of a free electron gas, with red dots indicating experimental values. The experimental values in these figures are from Ref. [24]. Figures taken from Ref. [22].

where ε_∞ typically takes on a value $1 \leq \varepsilon_\infty \leq 10$. Further limitations to the idealised free electron model can be seen by comparing the theoretical and experimental dielectric functions for gold, as shown in Figure 3.1. At energies below 2 eV ($\sim$ 480 THz, 620 nm), we can see that the theoretical model experimental values fairly well. However, at higher energies marked by interband transitions between the d and f band in gold ($\sim$ 2.4 eV, 580 Thz, 516 nm), we can see that the model deviates significantly, as it cannot account for the electrons jumping energy levels. This transition in the visible range is particularly important to keep in mind when conducting nonlinear experiments with gold, as we shall see in the experimental chapters.

3.2 Surface plasmon polaritons

Surface plasmon polaritons are surface EM waves that propagate along the interface between a conductor and a dielectric. These waves arise from the coupling between an external electromagnetic field and the collective oscillations of the free electrons gas. In the following, we will derive the key expression for SPPs propagating along an interface

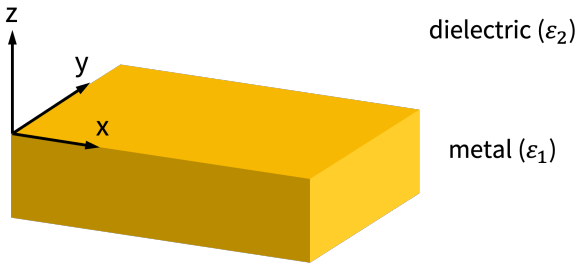


Figure 3.2: **Geometry of metal-dielectric interface**.

that will provide us with valuable insights.

We begin with Equation 3.1 and restrict ourselves to a wave travelling in the x direction for simplicity, with the material interface defined along the xy-plane as shown in Figure 3.2. The dielectric function $\varepsilon(z)$ only has a spatial dependence in z and does not vary over x or y. The wave is described by $\boldsymbol{E}(z)e^{i\beta x}$, where $\beta = k_x$ is the propagation constant corresponding to the wavevector in the propagation direction, and inserting this into the Helmholtz equation yields

$$\frac{\partial^2 \boldsymbol{E}(z)}{\partial z^2} + (k_0^2\varepsilon - \beta^2)\boldsymbol{E}(z) = 0 \ , \tag{3.8}$$

with the analogous wave equation for the magnetic field $\boldsymbol{H}$ being

$$\frac{\partial^2 \boldsymbol{H}(z)}{\partial z^2} + (k_0^2\varepsilon - \beta^2)\boldsymbol{H}(z) = 0 \ . \tag{3.9}$$

Before we can apply Equations 3.8 and 3.9, we define the different components of $\boldsymbol{E}$ and $\boldsymbol{H}$ utilising Equations 2.10c and 2.10d. We note that the region of interest is free of external charge ($\boldsymbol{J}_\mathrm{s} = 0$) or magnetisation ($\boldsymbol{M} = 0$), and that the electromagnetic wave has harmonic time dependence ($\partial/\partial t = -i\omega$), travels along x ($\partial/\partial x = i\beta$), and is

homogenous along y ($\partial/\partial y = 0$), to produce the following coupled equations:

$$\frac{\partial E_y}{\partial z} = -i\omega\mu_0 H_x \tag{3.10a}$$

$$\frac{\partial E_x}{\partial z} - i\beta E_z = i\omega\mu_0 H_y \tag{3.10b}$$

$$i\beta E_y = i\omega\mu_0 H_z \tag{3.10c}$$

$$\frac{\partial H_y}{\partial z} = i\omega\varepsilon_0\varepsilon E_x \tag{3.10d}$$

$$\frac{\partial H_x}{\partial z} - i\beta H_z = -i\omega\varepsilon_0\varepsilon E_y \tag{3.10e}$$

$$i\beta H_y = -i\omega\varepsilon_0\varepsilon E_z \ . \tag{3.10f}$$

Equation 3.10 has two different solutions depending on whether the propagating wave has transverse magnetic (TM) or transverse electric (TE) polarisation. For brevity, we assert that the TE mode vanishes and that SPPs only exist for TM polarisation (see Ref. [22] for the derivation). Restricting our focus to the TM modes where $H_x = H_z = E_y = 0$ reduces Equation 3.10 to

$$E_x = -i\frac{1}{\omega\varepsilon_0\varepsilon}\frac{\partial H_y}{\partial z} \tag{3.11a}$$

$$E_z = -\frac{\beta}{\omega\varepsilon_0\varepsilon}H_y \ , \tag{3.11b}$$

with the associated wave equation

$$\frac{\partial^2 H_y}{\partial z^2} + (k_0^2\varepsilon - \beta^2)H_y = 0 \ . \tag{3.12}$$

We now look at Equations 3.11 and 3.12 separately for the metal ($z < 0$) and dielectric ($z > 0$) regions, with the metal regions yielding solutions

$$H_y(z) = A_1 e^{i\beta x} e^{k_{z,1} z} \tag{3.13a}$$

$$E_x(z) = -iA_1 \frac{1}{\omega \varepsilon_0 \varepsilon_1} k_{z,1} e^{i\beta x} e^{k_{z,1} z} \tag{3.13b}$$

$$E_z(z) = -A_1 \frac{\beta}{\omega \varepsilon_0 \varepsilon_1} e^{i\beta x} e^{k_{z,1} z} \ , \tag{3.13c}$$

and the dielectric region yielding solutions

$$H_y(z) = A_2 e^{i\beta x} e^{-k_{z,2} z} \tag{3.14a}$$

$$E_x(z) = iA_2 \frac{1}{\omega \varepsilon_0 \varepsilon_2} k_{z,2} e^{i\beta x} e^{-k_{z,2} z} \tag{3.14b}$$

$$E_z(z) = -A_2 \frac{\beta}{\omega \varepsilon_0 \varepsilon_2} e^{i\beta x} e^{-k_{z,2} z} \ , \tag{3.14c}$$

where A_i is an unknown constant, ε_i is the permittivity, and $k_{z,i}$ is the wavevector perpendicular to the interface for the metal ($i = 1$) and dielectric ($i = 2$) regions respectively. We also note that the value $\hat{z} = 1/|k_{z,i}|$ describes the decay length of the fields perpendicular to the interface, which is a measure of the confinement of the field to the surface. The boundary conditions of Equation 3.2 require

$$A_1 = A_2 \tag{3.15a}$$

$$\frac{k_{z,1}}{k_{z,2}} = -\frac{\varepsilon_1}{\varepsilon_2} \ , \tag{3.15b}$$

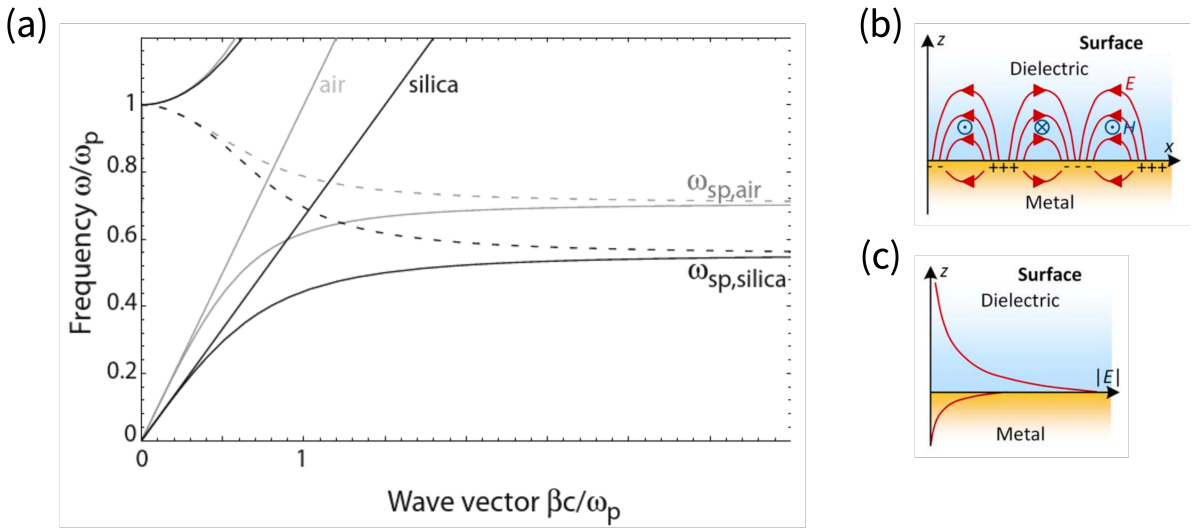


Figure 3.3: **Surface plasmon polaritons**. **(a)** Dispersion relation for SPPs at an interface between an idealised Drude metal and air/silica. The solid lines represent the real component and the dashed lines the imaginary component of β. The corresponding light lines for air and silica are also shown. Figure taken from Ref. [22]. **(b)** Diagram of SPP propagation along a metal/dielectric interface. Electric fields lines are in red and magnetic field lines are in blue. The local charge density is indicated just below the surface. **(c)** The magnitude of the electric field according to z showing exponential decay away from the surface. Figures (b) and (c) taken from Ref. [25].

and Equations 3.14a and 3.13a must fulfil Equation 3.12 which yields

$$k_{z,1}^2 = \beta^2 - k_0^2 \varepsilon_1 \tag{3.16a}$$

$$k_{z,2}^2 = \beta^2 - k_0^2 \varepsilon_2 \ . \tag{3.16b}$$

Finally, combining Equation 3.16 with Equation 3.15 gives us

$$\beta = k_0 \sqrt{\frac{\varepsilon_1 \varepsilon_2}{\varepsilon_1 + \varepsilon_2}} \ , \tag{3.17}$$

which is the dispersion relation of SPPs propagating along the defined interface.

Figure 3.3a plots β for SPPs at an interface between an idealised Drude metal and two dielectrics, air and silica, with the real and imaginary components represented by

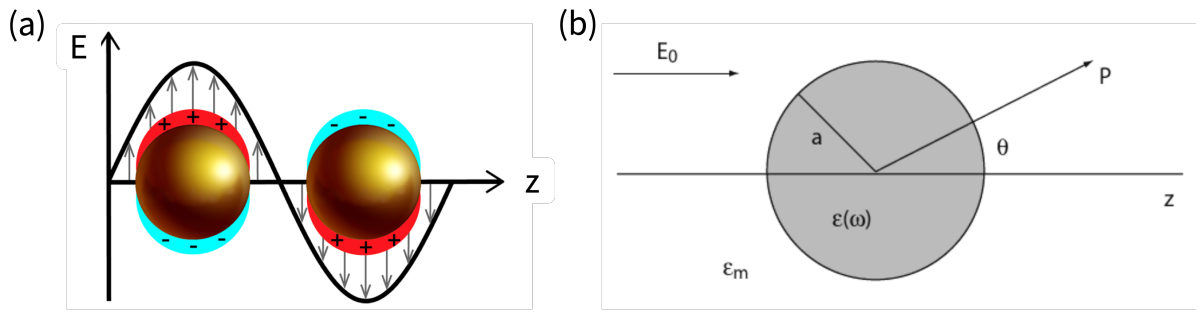


Figure 3.4: **Localised surface plasmons**. **(a)** Diagram of LSP. As an excitation field propagates in the z direction, the electron cloud within the nanosphere oscillates in response. Figure adapted from Ref. [26]. **(b)** Geometry of metallic sphere used in derivations. Figure taken from Ref. [22].

solid and dashed lines respectively. The light lines for air and silica are also plotted for reference. As bound modes, the SPPs correspond to the curves lying to the right of their respective light lines. For frequencies $\omega/\omega_p > 1$ there also exist radiative modes to the left of the light lines which are not SPP waves. A diagram of the SPP propagation along with the magnitude of the electric field are also shown in Figures 3.3b and c. As we can see, the field is confined near the interface and decays exponentially as you extend further out in either z-direction. As previously mentioned, the decay length is determined by k_z, while the propagation length of the SPP wave is determined by the imaginary component of β. Having observed the characteristic field confinement and enhancement properties of propagating SPP waves, we now turn to the second manifestation of plasmonic modes, localised surface plasmons.

3.3 Localised surface plasmons

Unlike the propagating SPPs, LSPs are non-propagating resonant modes that arise due to the collective oscillations of free electrons in a nanostructure when coupled to an external electromagnetic field as shown in Figure 3.4a. Here, we will derive its properties for the

simplest case of a metallic sphere with a radius that is much smaller than the wavelength of the excitation field, which allows us to use the quasi-static approximation and neglect any phase differences inside the particle. This simplifies our task to finding a solution to the Laplace equation,

$$\nabla^2 \Phi = 0 \ , \tag{3.18}$$

where Φ is the electrostatic potential, which in turn allows us to calculate the electric field $\boldsymbol{E} = -\nabla\Phi$. The geometry of the problem is shown in Figure 3.4b—a sphere of radius a and permittivity $\varepsilon(\omega)$ is surrounded by a dielectric with permittivity ε_m and experiences a field E_0 in the z-direction. The general solution for the case of spherical symmetry is given by

$$\Phi(r,\theta) = \sum_{l=0}^{\infty} \left[A_l r^l + B_l r^{-(l+1)} \right] P_l(\cos\theta) \ , \tag{3.19}$$

where $P_l(\cos\,\theta)$ are the Legendre polynomials of order l, and θ is the angle between position vector and the z-axis. After applying the appropriate boundary conditions at the surface of the sphere ($r = a$) and as r approaches infinity, the solutions read,

$$\Phi_{\text{in}} = -\frac{3\varepsilon_m}{\varepsilon + 2\varepsilon_m} E_0 r\cos\theta \tag{3.20a}$$

$$\Phi_{\text{out}} = -E_0 r\cos\theta + \frac{\boldsymbol{p}\cdot\boldsymbol{r}}{4\pi\varepsilon_0\varepsilon_m r^3} \ , \tag{3.20b}$$

where Φ_{in} and Φ_{out} are the potentials inside and outside of the sphere respectively, and $\boldsymbol{p}$ is the dipole moment,

$$\boldsymbol{p} = 4\pi\varepsilon_0\varepsilon_m a^3 \frac{\varepsilon - \varepsilon_m}{\varepsilon + 2\varepsilon_m} \boldsymbol{E}_0 \ . \tag{3.21}$$

Finally, we define the polarisability α according to $\boldsymbol{p} = \varepsilon_0 \varepsilon_m \alpha \boldsymbol{E}_0$ as

$$\alpha = 4\pi a^3 \frac{\varepsilon - \varepsilon_m}{\varepsilon + 2\varepsilon_m} \ . \tag{3.22}$$

Equation 3.22 describes the polarisability of a sub-wavelength metallic sphere, and α experiences a resonant enhancement for a minimum value of $\varepsilon + 2\varepsilon_m$, which for small values of $\mathrm{Im}(\varepsilon(\omega))$ simplifies to

$$\mathrm{Re}(\varepsilon(\omega)) = -2\varepsilon_m \ , \tag{3.23}$$

which is known as the Fröhlich condition. We note here that as the resonance of α is sensitive to the dielectric function of the surrounding medium, metallic nanoparticles such as the one described here make for excellent platforms for sensing applications. Another significant outcome of the resonant enhancement of α is the increased efficiency with which nanoparticles can scatter and absorb light [27]. The scattering and absorption cross-sections for particles with $a \ll \lambda$ are given by

$$\sigma_{\mathrm{sca}} = \frac{8\pi}{3} k^4 a^6 \left| \frac{\varepsilon - \varepsilon_m}{\varepsilon + 2\varepsilon_m} \right|^2 \tag{3.24a}$$

$$\sigma_{\mathrm{abs}} = 4\pi k a^3 \mathrm{Im}\left(\frac{\varepsilon - \varepsilon_m}{\varepsilon + 2\varepsilon_m} \right) \ . \tag{3.24b}$$

3.4 Conclusion

In this chapter, we covered the basic principles of plasmonics, starting with the Drude model and Helmholtz equation and the derivation of dielectric function for the free electron gas. We introduced the two different manifestations of plasmonic waves, SPPs, which

are propagating waves that are bound to the surface of a metal-dielectric interface, and LSPs, which are non-propagating waves that are bound to a nanostructure. We also discussed the fundamental characteristics of field confinement and resonant enhancement, which are the key properties that make plasmonic structures valuable for a variety of applications. One application in particular is that of a nanoantenna. Much like their radio counterpart, nanoantennas, or optical anteannas, manipulate light at optical frequencies [28]. As the fundamental working principle is essentially the same, nanoantennas couple free-space optical modes to highly localised near-field modes, though the scale of nanoantennas is much smaller, on the order of the wavelength of light. In a reciprocal fashion, nanoantennas are also able to efficiently radiate locally bound modes into the far-field. Due their high field confinement and resonant properties, plasmonic structures make for excellent nanoantennas and are often used for coupling light into sub-wavelength volumes. In the following chapter, we will present several examples of plasmonic nanoantennas that take advantage of the properties we have described here to enhance nonlinear processes.

Chapter 4

Optical Properties of Nanoantennas for Nonlinear Optics

In this chapter, we will discuss some of the key features that make for a good nonlinear optical nanoantenna, with an eye towards the nanoantenna designs that will be investigated in Chapters 5 and 6. We present some shared approaches to nanoantenna design through examples in recent literature, before performing a case study supported by simulations of two plasmonic nanoantennas, the waveguide resonator and dimer in Section 4.2 and the bar and discs in Section 4.3. The chapter concludes with key takeaways that will bridge the discussion presented here with the later experimental chapters.

4.1 Background

Nonlinear optical processes occur over a broad frequency range. In the case of SHG, for example, the fields involved in the mixing process span the range between the fundamental field (ω) and the second harmonic (2ω). The challenge in designing nanostructures for enhanced nonlinear emission lies in finding suitable materials and geometries that can

support resonances and high nonlinear coefficients at the fields of interest. As a starting point, it is common to turn to Miller's Rule which provides an empirical relationship between the nonlinear coefficients and the linear coefficients, which are easy to calculate. For the case of SHG, Miller's Rule gives

$$\chi^{(2)}(2\omega) = \delta^{(2)}(2\omega)\chi^{(1)}(2\omega)\chi^{(1)}(\omega)^2 \ , \tag{4.1}$$

where $\chi^{(2)}(2\omega)$ is the nonlinear susceptibility of interest, $\chi^{(1)}(2\omega)$ is the linear susceptibility at the second harmonic, $\chi^{(1)}(\omega)$ is the linear susceptibility at the fundamental, and $\delta^{(2)}(2\omega)$ is Miller's coefficient for a given material [29]. Equation 4.1 is derived from the Lorentz oscillator model treatment of oscillating charges discussed in Chapters 2 and 3, and its appeal lies in its applicability to a broad range of materials for predicting the nonlinear response to within an order of magnitude [30]. This expression gives us our first insight into designing nonlinear materials using plasmonic resonators—a resonance at each of the frequencies involved in a nonlinear process is expected to boost the nonlinear efficiency, as they directly affect a material's susceptibility.

4.1.1 Nonlinear optics via reciprocity

However, in the case of relatively new metamaterials, it is challenging to characterise even the $\chi^{(1)}$, as the optical response is dependent on the geometry of the nanostructures in question [31, 32]. Moreover, as we have seen in Chapter 3, the Drude-Lorentz model breaks down for gold at visible frequencies near interband transitions, and so to does Miller's Rule. Ultimately, Equation 4.1 deviates from experimental data for nanoantennas such as the ones we will study in subsequent sections [33, 34], and we require a different approach to supplement Miller's Rule and inform the direction of nanoantenna design for

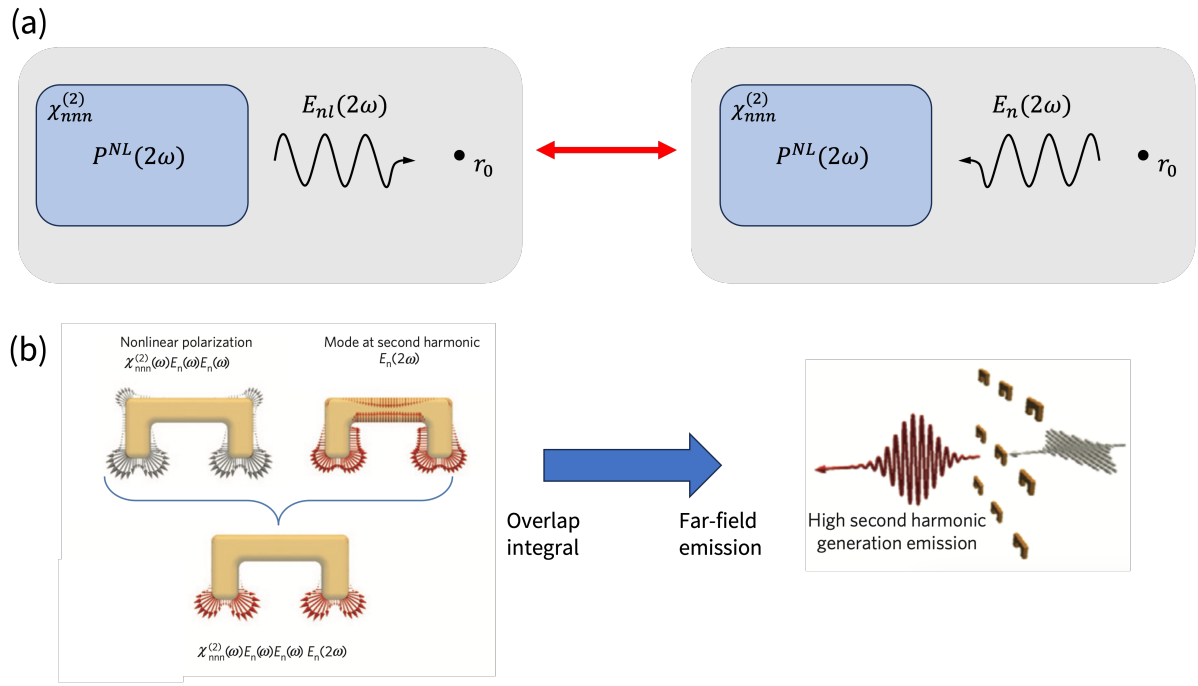


Figure 4.1: **Nonlinear scattering theory for SHG**. **(a)** Lorentz reciprocity for two different situations. On the left, an object with induced polarisation $P^{\mathrm{NL}}(2\omega)$ emits a field $E_{\mathrm{nl}}(2\omega)$ that is experienced at r_0. On the right, a dipole source at r_0 emits a field $E_{\mathrm{n}}(2\omega)$ that is experienced by the object. **(b)** An overlap integral is calculated from the linear fields at the fundamental and second harmonic in order to design a nanoantenna that demonstrates high SHG emission. Figure (b) adapted from Ref. [34].

nonlinear optics. The favoured approach, termed nonlinear scattering theory, is described in Reference [34] and diagrammed in Figure 4.1 for the case of SHG. In this example, suppose we have an input field $E_{\mathrm{n}}(\omega)$ that induces polarisation $P^{\mathrm{NL}}(2\omega)$ in a nonlinear medium with local nonlinear susceptibility $\chi^{(2)}_{\mathrm{nnn}}$. The dipoles within the medium then collectively act as a current source that generates a new field $E_{\mathrm{nl}}(2\omega)$ at the second harmonic. Lorentz reciprocity states that the same current would be generated in the medium if it was illuminated by a field $E_{\mathrm{n}}(2\omega)$ at the second harmonic frequency [35–37], and nonlinear scattering theory takes advantage of this to express the unknown nonlinear field in terms of an overlap integral,

$$E_{\mathrm{nl}}(2\omega) \propto \iint \chi^{(2)}_{\mathrm{nnn}} E^2_{\mathrm{n}}(\omega) \cdot E_{\mathrm{n}}(2\omega) dS \ , \tag{4.2}$$

where dS is the differential element of the surface S over which the integral is to be calculated. The analogous relation for THG is given by

$$E_{\mathrm{nl}}(3\omega) \propto \iint \chi^{(3)}_{\mathrm{nnn}} E^3_{\mathrm{n}}(\omega) \cdot E_{\mathrm{n}}(3\omega) dS \ , \tag{4.3}$$

where $E_{\mathrm{nl}}(3\omega)$ and $E_{\mathrm{n}}(3\omega)$ are the nonlinear and linear fields respectively at the third harmonic and $\chi^{(3)}_{\mathrm{nnn}}$ is the local third-order nonlinear susceptibility.

Equations 4.2 and 4.3 state that the relative strength of the nonlinear emission is dependent on the overlap between the modes at the fundamental and second/third harmonic, and this is useful for engineering nonlinear nanoantennas as it reduces the problem of directly calculating nonlinear emission from a distribution of dipoles into a calculation involving the linear fields at the relevant frequencies instead. Moreover, whereas Miller's rule considers the average susceptibility of a structure, which might not reflect the effects of local resonances, nonlinear scattering theory takes into account the local susceptibility χ_{nnn} which plays an important role in nanoscale engineering. This is aided by the availability of modern simulation software implementing numerical techniques that are capable of utilising χ_{nnn} over a 3D simulation space such as the finite-difference time-domain (FDTD) method, which we will make use of in Sections 4.2 and 4.3.

4.1.2 Multi-resonant antennas

We have seen in Chapter 3 how plasmonic structures provide field enhancements, and this can be used to boost nonlinear processes by augmenting the fundamental field. However, further optimisation is made possible by engineering nanoantennas that are resonant at multiple wavelengths for the different fields involved [38–41]. As an example, let us take a look at the plasmonic nanoantenna studied in Reference [42]. This nanoantenna, as

shown in Figure 4.2a, was designed to enhance SHG emission by engineering modes at the fundamental and second harmonic wavelengths. This is achieved by coupling between two particles (V-shape and nanorod) that possess their own individual modes to form hybridised modes for the collective nanoantenna. Figure 4.2b displays the scattering spectra that exhibit the various modes. The grey line is the scattering for the individual V-shape particle with modes V_1 (which is tuned to the pump wavelength) and V_2 (which is far from the second harmonic wavelength). When coupled with the nanorod, however, the scattering shown by the open black circles displays modes V_1 and V_2^A that are well aligned with the pump and second harmonic wavelengths respectively. Figure 4.2c shows the field enhancement profiles that give deeper insight into the polarisation of the modes. As can be seen in the rightmost figure, the resonance at the fundamental wavelength comes from a dipole mode in the V-shape particle that is oriented along the y-axis. In the leftmost figure, a dipole mode along the x-axis is responsible for the resonance at the second harmonic. This is confirmed by the scattering spectra of the blue and red lines in Figure 4.2b that are for x- and y-polarisation respectively.

Utilising this design, the authors achieved an SHG conversion efficiency of $\sim 5 \times 10^{-10}$ W^{-1} and SHG photon emission rate of $\sim 3 \times 10^6$ s^{-1}. As stated in the study, the efficiency of SHG in these structures is dependent on three conditions: (1) multi-resonance at the fundamental and second-harmonic wavelengths, (2) good spatial overlap of the localised fields (Equation 4.2), and (3) geometry that allows for dipolar second-harmonic emission. We will keep this in mind when evaluating the design of our own nanoantennas in the following sections. Furthermore, there are three additional takeaways from this study. First, fine-tuning of nanoantenna resonances can be achieved not only by varying the geometry but by coupling different structures with their own primary modes.

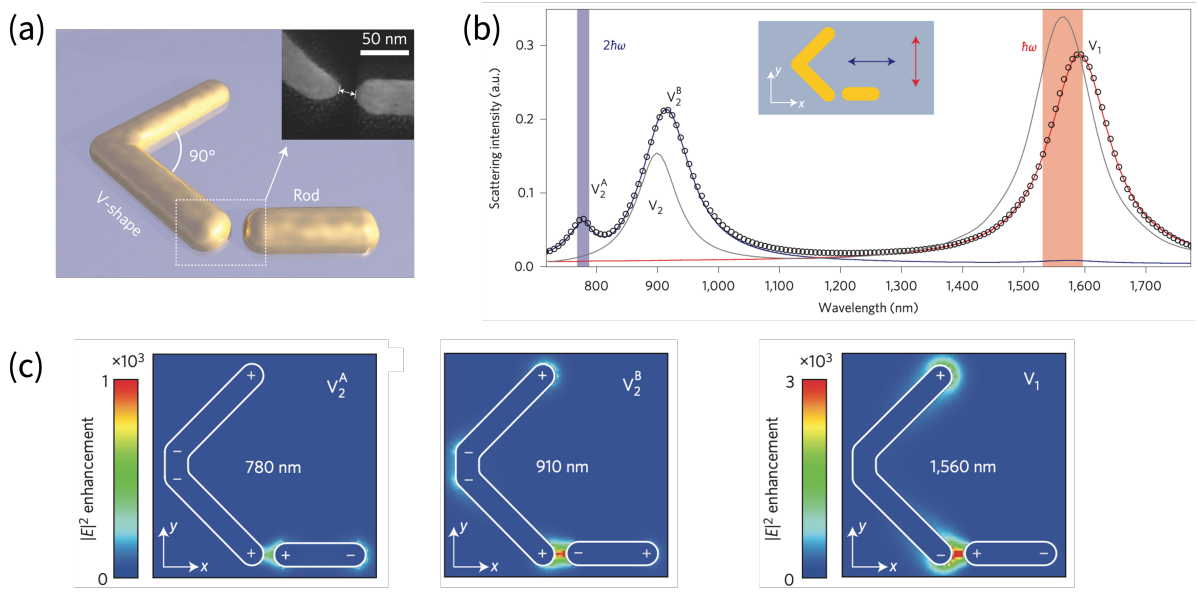


Figure 4.2: **Enhanced SHG in multiresonant plasmonic nanoantenna**. **(a)** Illustration of coupled V-shape and nanorod with the inset SEM image showing a 50 nm gap. **(b)** Simulated scattering spectra with an unpolarised source for the isolated V-shape particle (grey line) showing modes V_1 and V_2, and coupled nanoantenna (open black circles) showing hybrid modes V_2^A and V_2^B. Scattering for a linearly polarised source are shown by the blue and red lines with the polarisation direction indicated in the inset. The red and blue vertical stripes indicate the wavelength range of the pump and the expected SHG signal respectively. **(c)** Local electric field enhancement at the resonance wavelengths showing different orientations of dipole modes. All figures taken from Ref. [42].

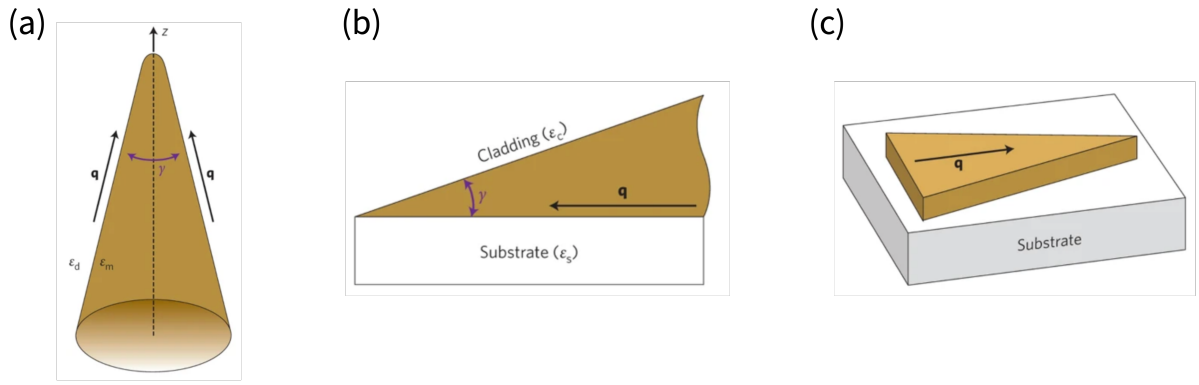


Figure 4.3: **Examples of nanofocusing configurations**. **(a)** Tapered metal rod with rounded tip. **(b)** Metal wedge surrounded by dielectric media. **(c)** Tapered metal waveguide. All figures taken from Ref. [46].

Second, coupling structures in this manner opens up additional degrees of freedom in geometric parameters for engineering modes (for example, the gap between the V-shape and nanorod and the angle of their orientation). Finally, the broadband field profiles extracted from linear simulations provide information on what polarisation can best excite the fundamental mode as well as the expected polarisation of the nonlinear emission.

4.1.3 Nanofocusing and coupling bright and dark modes

Although plasmonic structures provide the local field enhancements needed for a viable nanoantenna, there needs to be a way to efficiently direct optical energy into these local hot-spots. One technique that addresses this problem is known as nanofocusing, and it has gained significant attention for its ability to manipulate light and concentrate it into regions well below the diffraction limit in metal-dielectric structures [28, 43–45]. Early implementations of nanofocusing focused on tapered structures that support SPP modes such as rounded metallic tips [47, 48] or tapered waveguides [49, 50] as shown in Figure 4.3. More recently, the nanofocusing effect has been demonstrated in metallic nanoparticles [51, 52] and nanogaps [53, 54]. In the case of nanogap structures, the gap mode cannot

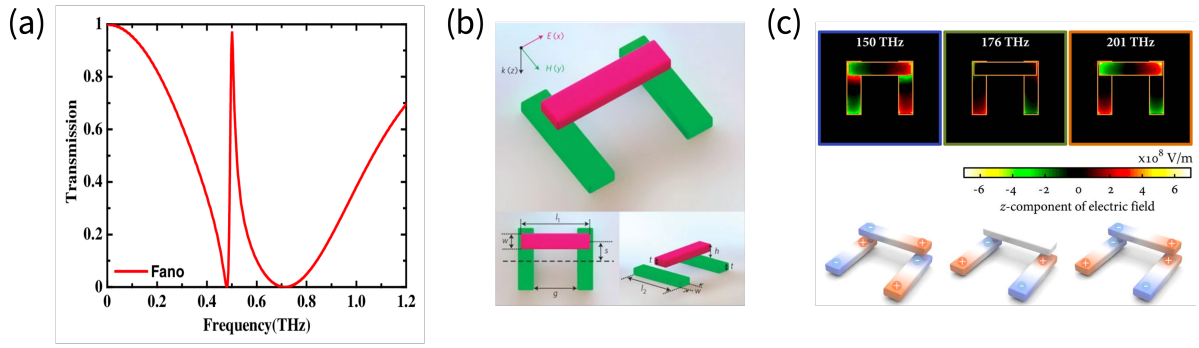


Figure 4.4: **Coupling bright and dark resonators**. **(a)** Simulated transmission spectrum of coupled structure showing Fano resonance. **(b)** Illustration of coupled bar and nanowires geometry with the two components shown in pink and green. **(c)** Simulated E_z profiles of nanoantenna in (b) at three different frequencies. Figures taken from: (a) Ref. [57], (b) Ref. [58], (c) Ref. [59].

typically be excited directly by external illumination due to the electric field symmetry or scale of the external field relative to the gap. A solution to this is to couple indirectly via a second resonator that can interact with the excitation field [53]. Coupling between multiple resonators in this fashion can lead to a phenomenon called Fano resonance [55–57], and a transmission spectrum exemplifying this is shown in Figure 4.4a. Here, a spectrally narrow resonance couples to a second much broader resonance, resulting in a sharp peak in the overall transmission dip which typically displays an asymmetric shape. This occurs because the narrow resonance represents a 'bright' resonator that couples well with an external field and radiates energy, reducing the population of the 'dark' resonance in the process. Composite nanoantennas like these typically exhibit a mechanism for controlling the coupling strength between the bright and dark resonators to manipulate the collective optical response.

An example that is of particular interest is the gold nanoantenna system described in Reference [58–60]. Figure 4.4b shows the two coupled elements in different colours with the top bar nanoantenna in pink being able to be displaced from the bottom nanowires in green in both the vertical and lateral directions. Figure 4.4c shows the E_z field profile

at different frequencies with either a symmetric or anti-symmetric field distribution between the top and bottom antennas and destructive interference exhibited in the middle figure. In this example, the lateral displacement of the bar nanoantenna was used to control the transmission of the composite system to demonstrate a phenomenon known as electromagnetically induced transparency [61, 62]. Here this is manifested as a coherent exchange of energy between a bright dipole that interacts with the incident beam, and a dark resonance that can only interact with the beam via the bright dipole mode. In the following section, we will see how a coupled nanoantenna similar to the one described here can be used to control field confinement and nonlinear scattering via nanofocusing.

4.2 Waveguide resonator and dimer

The proposed nanoantenna design is a coupled gold waveguide resonator and dimer, which is shown in Figure 4.5. The design is similar to the one in References [58–60] with the advantage of being a quasi-2D structure that can be built in a single fabrication step. Similar to the bar particle in the previous example, the dimer is able to be displaced along the waveguide axis, with d describing the lateral distance between the dimer and the centre of the waveguide. As our primary varying parameter, we wish to explore the effect of d on the coupling between the waveguide resonator and dimer modes, and ultimately on SHG and THG. The nanoantenna is to be illuminated at normal incidence for y-polarised light along the dimer axis. The designated fundamental wavelength is 1550 nm, for a second and third harmonic signal at 775 nm and 517 nm respectively. When coupling to the waveguide resonator via the dimer, we expect that the greatest field enhancement will occur in the 50 nm waveguide gap. In the following subsections, we examine this in more detail with broadband simulations performed on Lumerical FDTD.

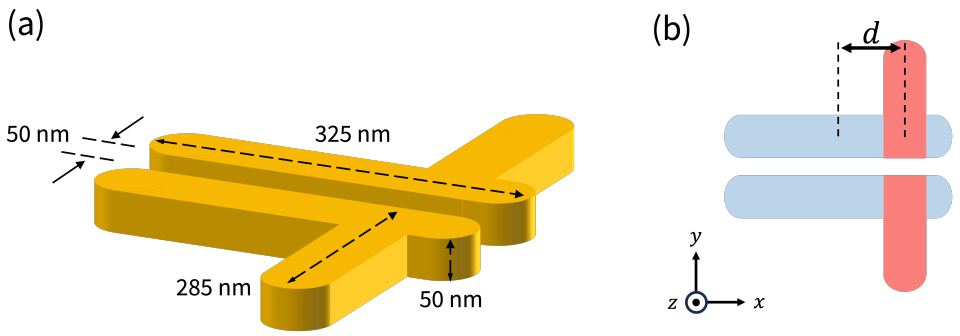


Figure 4.5: **Waveguide resonator and dimer nanoantenna**. **(a)** Illustration of nanoantenna with dimensions. **(b)** The displacement d measures the lateral distance of the dimer from the centre of the waveguide resonator.

4.2.1 Electric field enhancement and mode overlap

We begin by examining the waveguide resonator and dimer separately. As in the previous example, the waveguide acts as a dark resonator and the gap mode cannot be effectively excited independently. The field enhancement profile for the isolated waveguide resonator shown in Figure 4.6a confirms this, as the fields are concentrated on the ends of the waveguide with no localisation in the gap. Figure 4.6b, on the other hand, shows a bright dipole mode excited in the dimer for y-polarised light, which will be the primary means of coupling to the waveguide resonator mode.

Figure 4.7 shows the field enhancement at the fundamental wavelength for the coupled waveguide-dimer nanoantenna at $z = 0$ nm for displacements ranging from 0 to 110 nm. At $d = 0$ nm, the dimer is placed at the node of the waveguide resonator mode where the field is equal to zero, and as such we see minimal confinement of the field in the gap. As we break the symmetry by moving to higher displacement values, we can see the field strength increasing inside the gap due to stronger coupling between the dimer and waveguide resonator and the emergence of a quadrupole-like mode. However, the field strength diminishes again as we move to successively higher displacements. The same field enhancement profiles are shown for the second and third harmonic wavelengths in Figures

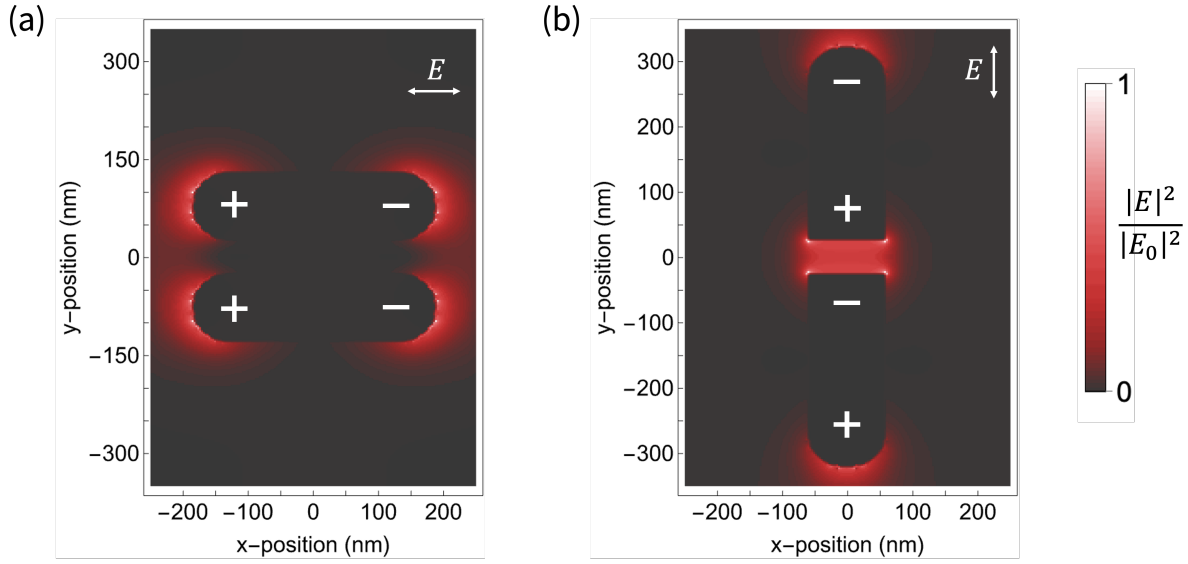


Figure 4.6: **Simulated field enhancement at fundamental wavelength for: (a)** waveguide resonator with x-polarisation and **(b)** dimer with y-polarisation for a 1550 nm source. Profiles are normalised to an arbitrary scale.

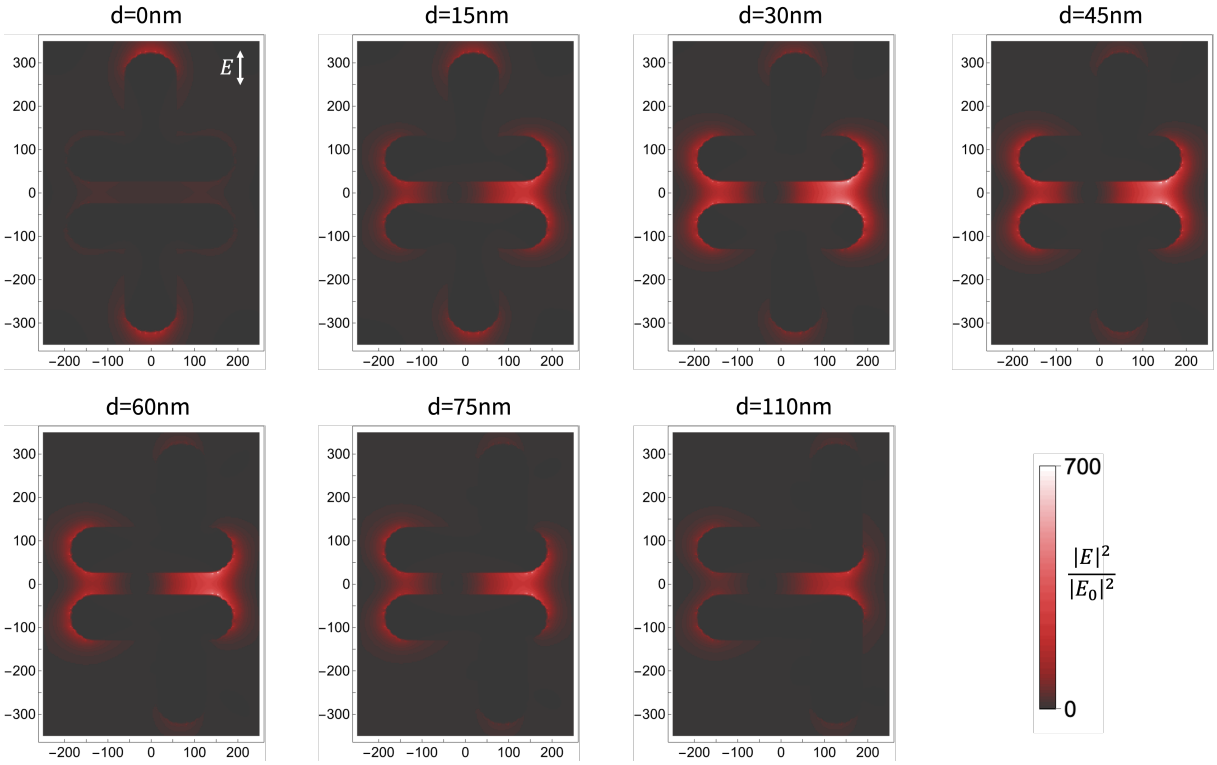


Figure 4.7: **Simulated field enhancement at fundamental wavelength for coupled waveguide-dimer**. Profiles are shown for seven different dimer displacements from $d = 0$ to $d = 110$ nm for a y-polarised source at 1550 nm.

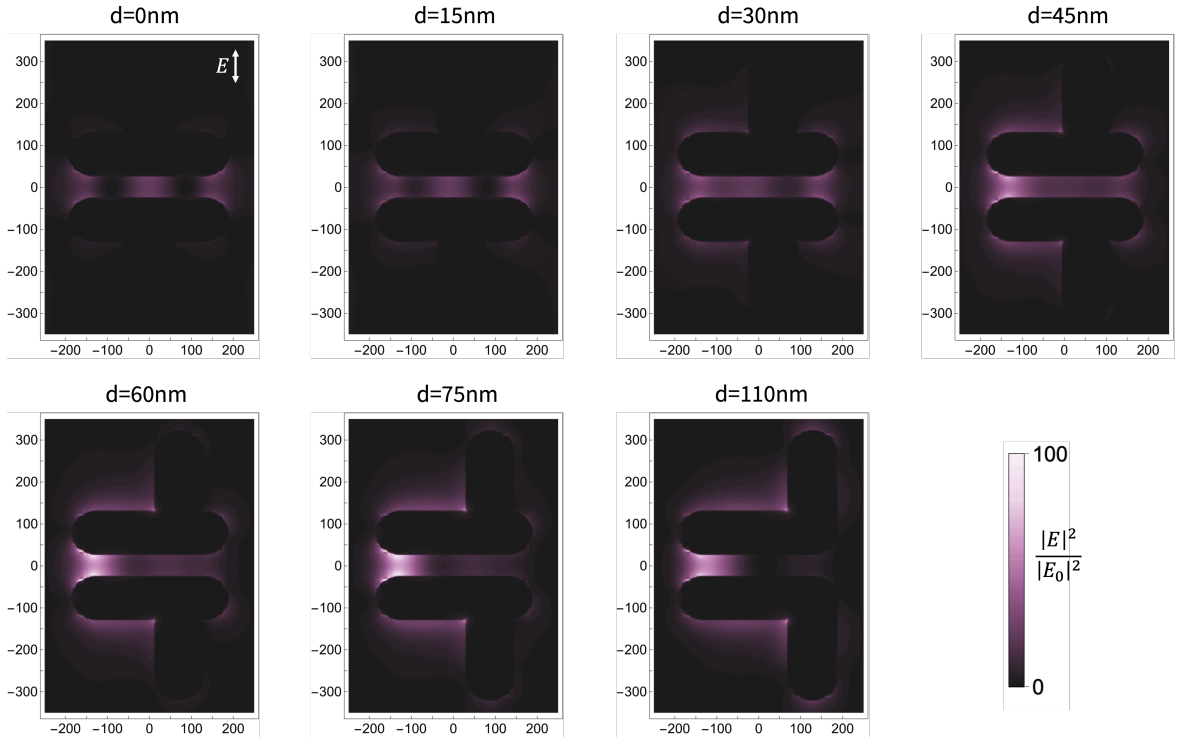


Figure 4.8: **Simulated field enhancement at second harmonic wavelength for coupled waveguide-dimer**. Profiles are shown for seven different dimer displacements from $d = 0$ to $d = 110$ nm for a y-polarised source at 775 nm.

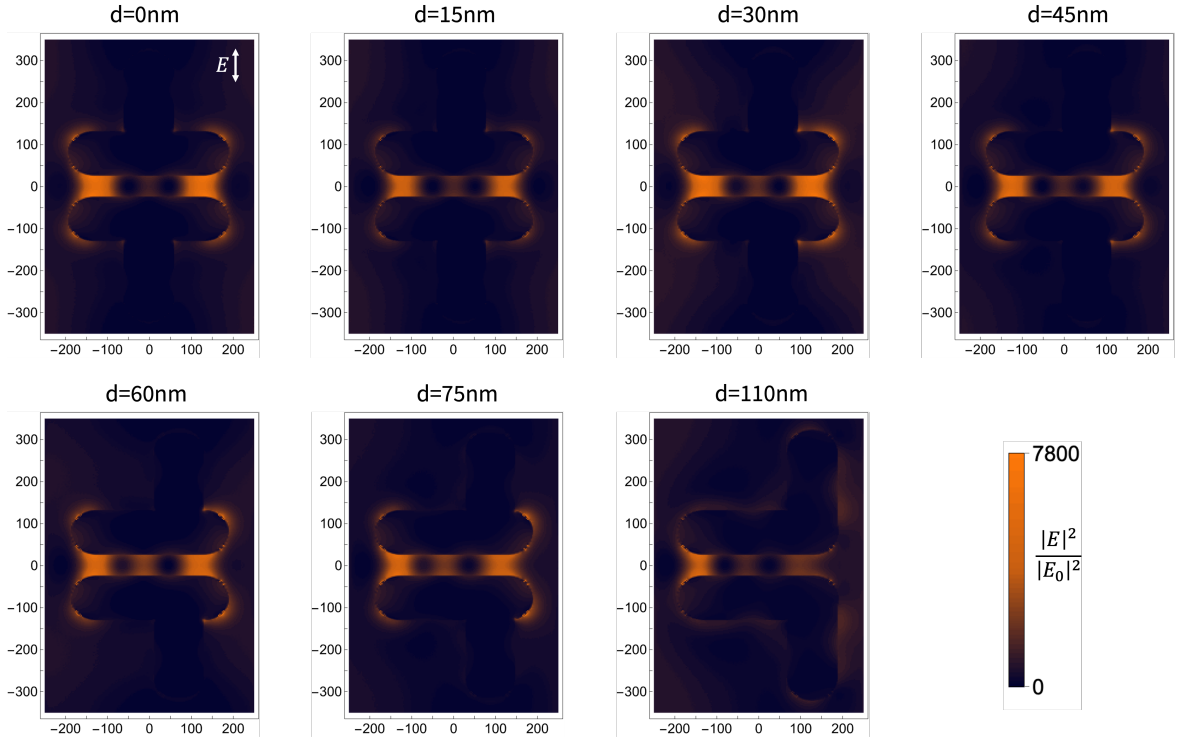


Figure 4.9: **Simulated field enhancement at third harmonic wavelength for coupled waveguide-dimer**. Profiles are shown for seven different dimer displacements from $d = 0$ to $d = 110$ nm for a y-polarised source at 517 nm.

4.8 and 4.9 respectively. Like the fundamental, the second and third harmonic fields are well confined to the waveguide gap, which suggests that there is non-trivial overlap with the fundamental mode.

As a point of reference, we first integrate the fundamental field enhancement profiles in Figure 4.7 according to $\iint E_{\omega}^{2} dS$. The integration was performed over the 2D plane shown in the figures, and the results according to the displacement value are plotted in Figure 4.10a. This confirms our earlier observation of the relative field strength within the waveguide gap, with a local maximum at $d = 30$ nm suggesting that excessive coupling between the waveguide resonator and dimer will have a negative impact on the field enhancement and nonlinear processes. We now refer to Equations 4.2 and 4.3 to calculate the overlap between the fundamental and second/third harmonic modes as $\iint E_{\omega}^{2} E_{2\omega} dS$ and $\iint E_{\omega}^{3} E_{r\omega} dS$ respectively. As we can see in Figures 4.10b and 4.10c, both overlap integrals follow the same pattern as the fundamental field enhancement in Figure 4.10a with a minimum value for $d = 0$ nm, a maximum value for $d = 30$ nm, and decreasing values for successively higher displacements.

The transmission spectra shown in Figure 4.10d provide further insights into the resonances of the coupled structures. For the case of $d = 0$ nm (dark green line) a single broad resonance can be seen corresponding to a transmission dip. This resonance is attributed to the excitation of the dimer, which is strongly coupled to the 1550 nm light in free space (Fig. 4.6b). The waveguide resonance is not visible here as the two are not coupled to each other in the absence of the symmetry breaking. For $d = 15$ nm (yellow line), we see the emergence of the characteristic Fano resonance with a small peak near 1550 nm within the transmission valley. This peak grows with increasing d, indicating the growing coupling strength between the two resonances and the domination of the waveguide

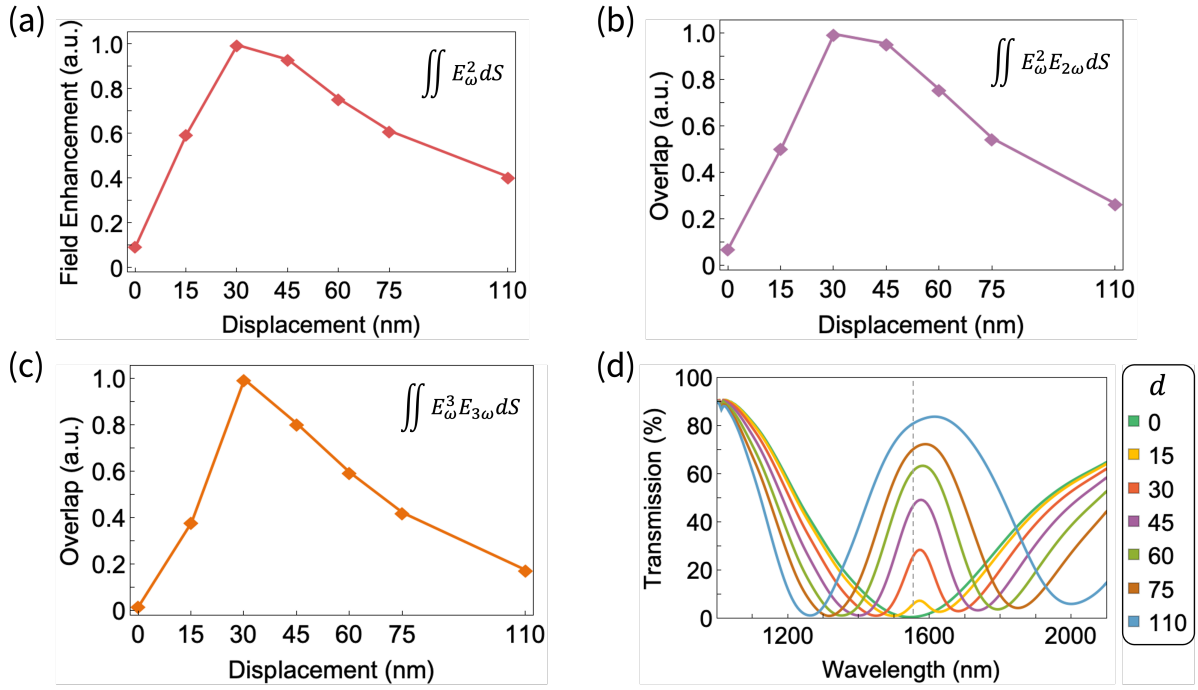


Figure 4.10: **Field enhancement, mode overlap, and transmission for coupled waveguide-dimer according to displacement**. **(a)** Fundamental field enhancement at 1550 nm. Calculated by integrating the profiles in Fig. 4.7. **(b)** Mode overlap between the fundamental and second harmonic fields. Calculated from profiles in Figs. 4.7 and 4.8. **(c)** Mode overlap between the fundamental and third harmonic fields. Calculated from profiles in Figs. 4.7 and 4.9. **(d)** Simulated transmission spectra for different displacements. A grey reference line at 1550 nm is included to show the resonance shifting to longer wavelengths for higher displacements.

resonator's quadrupole-like mode over the the dimer.

4.2.2 Polarisation

To conclude this simulation study, we perform a polarisation series of the 1550 nm input field to observe the effects of illuminating the nanoantenna at off-axis polarisations that are not optimal for exciting the dimer. Figure 4.11 shows the field enhancement calculated in the same manner as Figure 4.10a for different polarisations and displacements. For $d > 0$ nm we see the expected behaviour of the nanoantenna with the strongest enhancement occurring when light is optimally coupled to the waveguide resonator via the

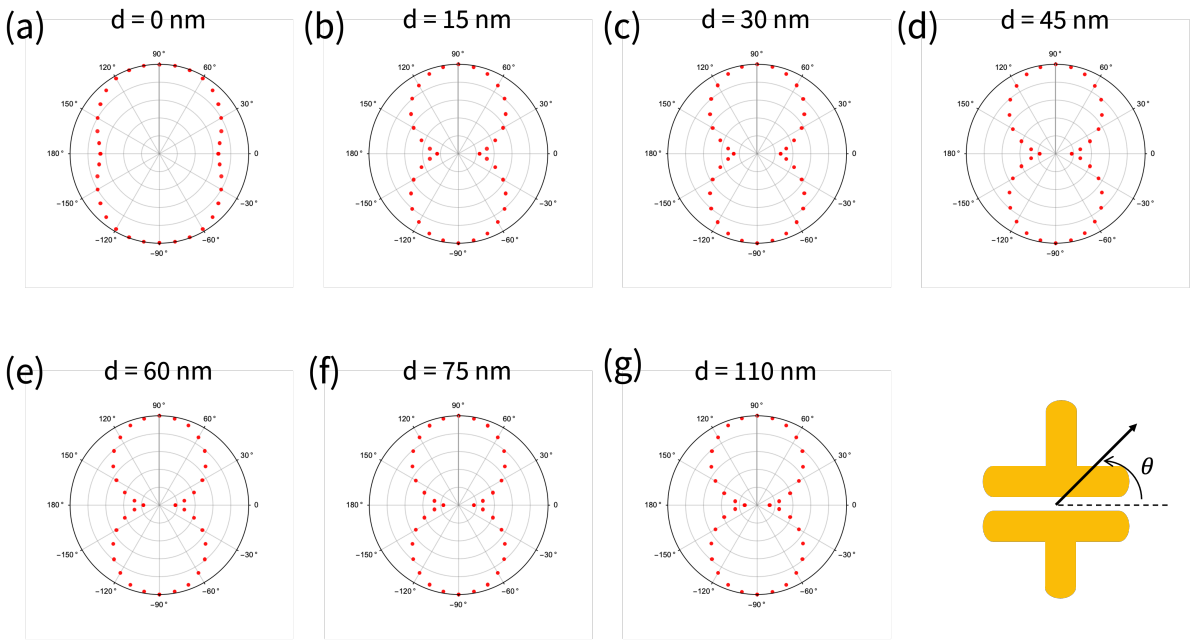


Figure 4.11: **Field enhancement according to polarisation for different dimer displacements**. 90° corresponds to the y-polarisation along the dimer axis.

dimer at 90° polarisation. For the symmetric configuration at $d = 0$ nm where light is not well coupled to the waveguide resonator, we still see a bias towards 90°, although the overall enhancement is weakest among the different displacements. As the actual nonlinear experiments involve non-ideal nanoantennas with fabrication imperfections and symmetry defects, we will return to this mode of investigation to explore potentially unforeseen effects.

4.3 Bar and discs

For our second case study, we turn to the gold bar and discs nanoantenna which has been previously studied in Reference [63]. Originally designed to study the effects of symmetry on SHG far-field emission, the nanoantenna supports dual resonances at the designated fundamental (1500 nm) and second harmonic (750 nm) wavelengths. Figure 4.12a shows the geometry of the nanoantenna for two different configurations. The nanoantenna itself

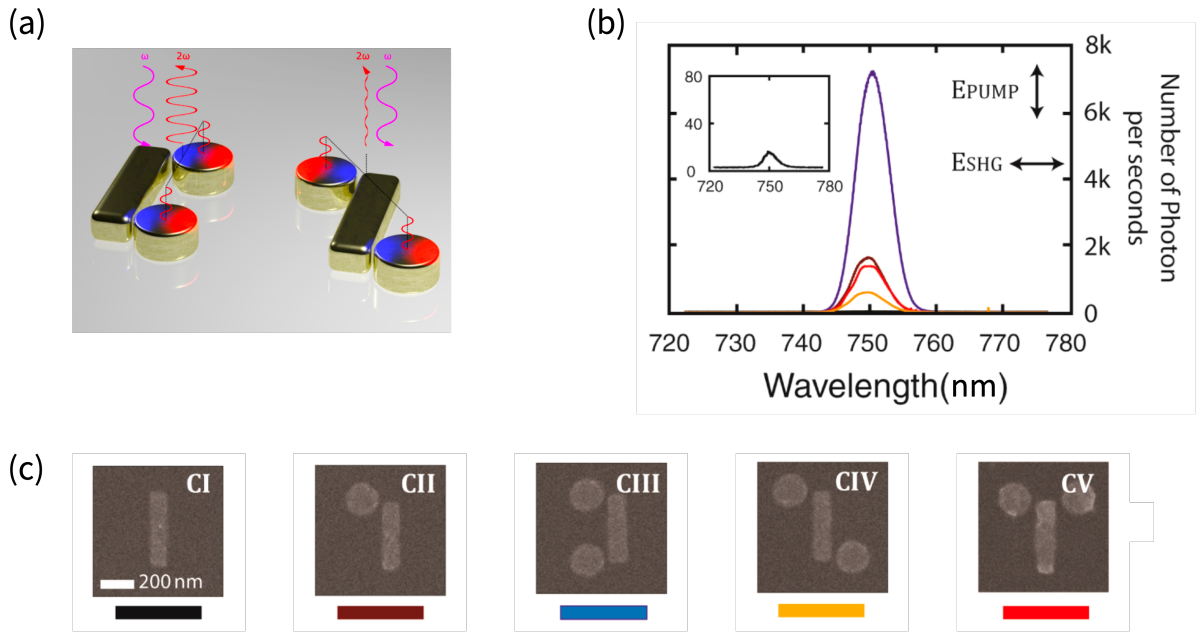


Figure 4.12: **Bar-discs nanoantenna for SHG**. **(a)** Illustration of bar-discs nanoantenna for two different configurations of discs. The antenna on the left has discs radiating in phase leading to bright SHG emission, as indicated by the red wave. **(b)** SHG intensity according to nanoantenna configuration. The highest SHG intensity is achieved by configuration CIII.The lowest SHG intensity exhibited by configuration CI is shown in the inset. **(c)** The five nanoantenna configurations studied in this experiment (CI–V). All figures taken from Ref. [63].

is composed of one bar particle and two disc particles that can be arranged in different locations around the bar with varying degrees of symmetry. The bar particle, which supports a dipole resonance at 1500 nm and a quadrupole-like mode at 750 nm is excited by an external field, with near-field coupling between the particles leading to re-radiation of SHG by the discs, which support a dipole resonance at 750 nm. The five different configurations of bar and discs that have been studied in this work are shown in Figure 4.12c.

We can see from Figure 4.12b that the highest measured SHG signal comes from nanoantenna configuration CIII with the discs placed on the same side of the bar. This is attributed to the dipole modes of the discs radiating in phase resulting in constructive interference and bright emission into the far-field (see Ref. [63] for a full discussion).

Meanwhile, configuration CIV has the discs radiating at π out of phase leading to destructive interference and reduced SHG far-field emission. As it is the most efficient configuration, we focus on nanoantenna CIII and move to simulate its optical properties.

4.3.1 Electric field profile and transmission

Figures 4.13 and 4.14 show the simulated $|E|^2/|E_0|^2$ and E_z/E_0 at horizontal and vertical polarisation for 1500 nm and 750 nm respectively. From Figures 4.13a–b, we can see that the dipole resonance at the fundamental wavelength of 1500 nm is well excited when the light is polarised along the bar axis. When the polarisation is perpendicular to the bar (Figs. 4.13c–d), the dipole orientation changes and the field enhancement is over an order of magnitude lower. This informs us on how to polarise the 1500 nm beam in later nonlinear experiments. For 750 nm illumination, the field is concentrated around the discs for x-polarisation (Fig. 4.14a) and the gap between the bar and discs for y-polarisation (Fig. 4.14c), indicating coupling between the two particles. The E_z profile for y-polarisation in the Figure 4.14d also shows the bar resonating in a quadrupole-like mode. This confirms our earlier assertion that the quadrupole mode of the bar couples with the dipole mode of the discs for efficient SHG radiation.

Finally, we turn to the transmission spectrum in Figure 4.15 to verify the multi-resonance of the coupled nanoantenna system. The identifiable dips near 1500 nm and 750 nm confirm that the nanoantenna supports dual resonances at the fundamental and second harmonic wavelengths for enhanced SHG emission. The additional dip in the transmission spectrum near 1020 nm is an artifact of the simulation, which is confirmed by FTIR spectra shown in Chapter 6.

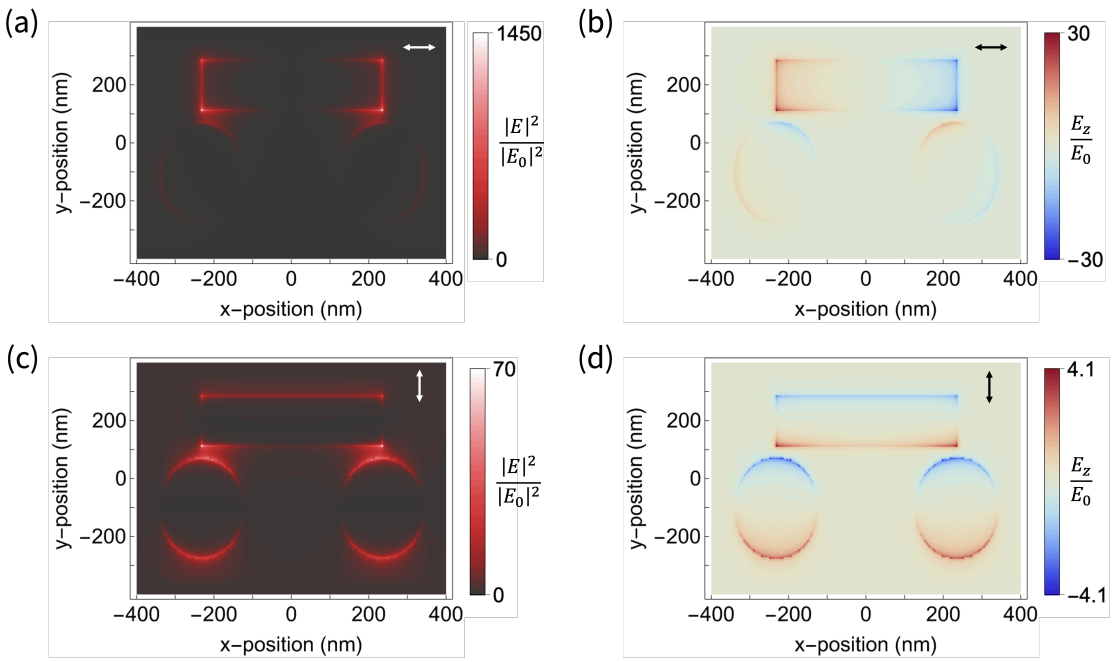


Figure 4.13: **Simulated field profiles at fundamental wavelength for bar-discs nanoantenna**. **(a–b)** $|E|^2/|E_0|^2$ and E_z/E_0 for x-polarisation parallel to the bar. **(c–d)** $|E|^2/|E_0|^2$ and E_z/E_0 for y-polarisation perpendicular to the bar. All profiles are taken on a plane 2 nm above the surface of the nanoantenna for a 1500 nm source. The polarisation direction is indicated by the black/white arrows.

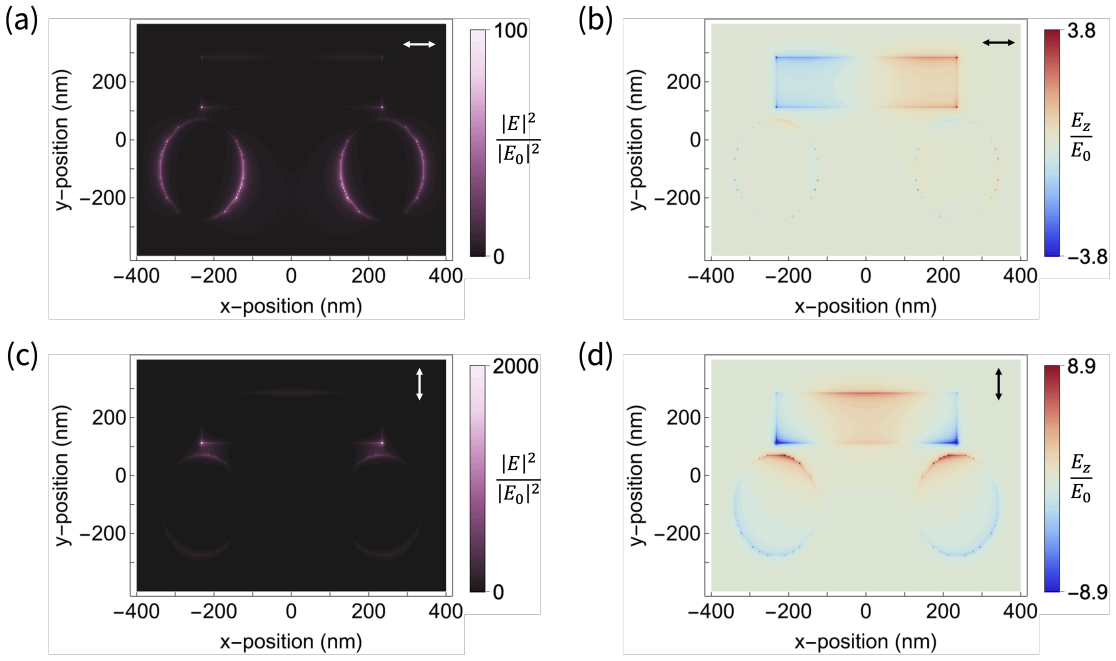


Figure 4.14: **Simulated field profiles at second harmonic wavelength for bar-discs nanoantenna**. **(a–b)** $|E|^2/|E_0|^2$ and E_z/E_0 for x-polarisation parallel to the bar. **(c–d)** $|E|^2/|E_0|^2$ and E_z/E_0 for y-polarisation perpendicular to the bar. All profiles are taken on a plane 2 nm above the surface of the nanoantenna for a 750 nm source. The polarisation direction is indicated by the black/white arrows.

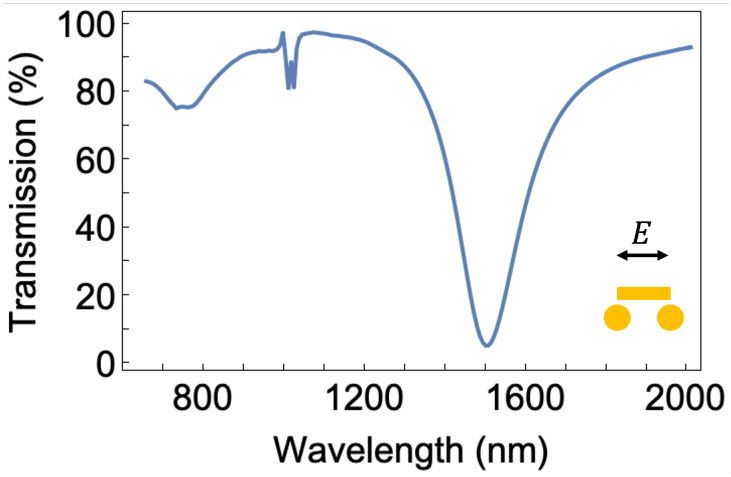


Figure 4.15: **Simulated transmission of bar-discs nanoantenna**. The source polarisation is parallel to the bar as shown in the inset.

4.4 Conclusion

In conclusion, we have presented the basic principles of Miller's rule and nonlinear scattering theory which justifies an approach to designing nonlinear nanoantennas by investigating their linear response to the wavelengths of interest. We also reviewed examples of plasmonic nanoantennas in recent literature which demonstrate multiple resonances, nanofocusing, and coupled bright-dark modes to enhance nonlinear emission. With this motivation, we performed simulations to explore the linear optical properties of two plasmonic nanoantennas, the waveguide-dimer and the bar-discs. We are now ready to investigate the nonlinear optical response of these structures. In Chapter 5 we will use the waveguide-dimer nanoantenna to examine the coupling mechanism that was described in Section 4.2 in more detail. In Chapter 6 we will use the bar-discs nanoantenna to demonstrate a new process, FWM, and assess its ability to produce correlated photons via spontaneous four-wave mixing (SFWM).

Chapter 5

Frequency Mixing in Critically Coupled Nanoantennas

In this chapter, we utilise our understanding of the waveguide resonator and dimer nanoantenna gained in Chapter 4 to support an experimental investigation of its enhanced nonlinear emission. We begin by presenting a coupled oscillator model in Section 5.1 that characterises the various parameters describing our coupled nanoantenna system and identifying the conditions for optimum field enhancement according to a critical coupling condition. We proceed by presenting SHG and THG measurements in Section 5.2 that validate the occurrence of critical coupling within the nanoantenna, along with measurements with off-axis input polarisations that exhibit interesting side features. Finally, we conclude with a summary of the experimental results and a perspective on future work and applications for this type of nanoantenna design. This chapter expands on the work presented in Reference [64] and contains contributions from Dr. Xiaofei Xiao in the fabrication of the nanoantenna and collection of SEM images and FTIR spectra.

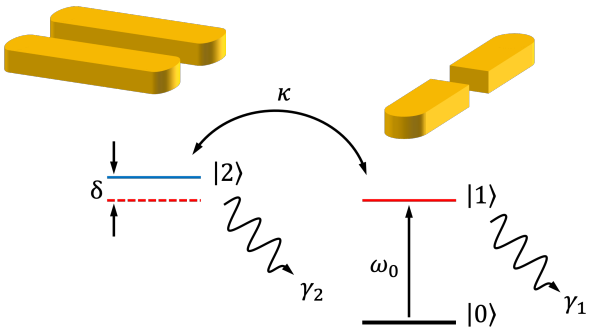


Figure 5.1: **Three-level model for coupled waveguide-dimer system**. The dimer in the ground state $|0\rangle$ can be excited by a bright transition to $|1\rangle$ and coupled to a dark state $|2\rangle$ as described by coupling parameter κ. The dissipation rate of the bright state due to both radiative and non-radiative damping is described by γ_1, and γ_2 is the dissipation of the dark state due solely to non-radiative damping. Figure drawn similar to Ref. [59].

5.1 Coupled oscillator model

As we have seen in Chapter 3, the optical response of a single plasmonic nanoantenna is well described by the classical model of a driven damped oscillator. Here, we extend the model to the case of two coupled oscillators, a bright dimer and a dark waveguide resonator. The oscillations of the dipole-like dimer mode with amplitude $a(t)$ and the quadrupole-like waveguide resonator mode with amplitude $b(t)$ are described by two second-order differential equations,

$$\ddot{a}(t) + \gamma_1 \dot{a}(t) + \omega_0^2 a(t) + \kappa b(t) = g_1 E(t) \tag{5.1a}$$

$$\ddot{b}(t) + \gamma_2 \dot{b}(t) + (\omega_0 + \delta)^2 b(t) + \kappa a(t) = g_2 E(t) \ , \tag{5.1b}$$

where γ_1 and γ_2 are the damping parameters for the dimer and waveguide resonator respectively, ω_0 is the resonance frequency of the dimer, δ is the detuning between the waveguide resonator and dimer resonances, κ represents the coupling strength between

the waveguide resonator and dimer, and g_1 and g_2 represent the coupling between the dimer and waveguide resonator respectively to an external driving field $E(t)$ that is co-polarised with the dimer (orthogonal to the waveguide axis) and at normal incidence. As the dark waveguide resonator mode cannot be excited by this field and can only be driven by the bright dimer mode, g_2 and Equation 5.1b are equal to zero. The three-level model describing this system is diagrammed in Figure 5.1.

If we assume $a(t) = a_o e^{-i\omega t}$, $b(t) = b_0 e^{-i\omega t}$, and $E(t) = E_0 e^{-i\omega t}$, our coupled equations read,

$$\begin{pmatrix} \omega_0^2 - i\omega\gamma_1 - \omega^2 & \kappa \\ \kappa & (\omega_0 + \delta)^2 - i\omega\gamma_2 - \omega^2 \end{pmatrix} \begin{pmatrix} a_0 \\ b_0 \end{pmatrix} = \begin{pmatrix} g_1 \\ 0 \end{pmatrix} E_0 \ . \tag{5.2}$$

If we further assume the detuning to be small, $\omega_0 \approx \omega_0 + \delta$, and the resonances sufficiently narrow, we can apply the rotating wave approximation such that $\omega_0^2 - i\omega\gamma_i - \omega^2 \approx \omega_0(\omega_0 - i\gamma_i - \omega)$ and divide by ω_0 and set $E_0 = 1$ to get

$$\begin{pmatrix} \omega_0 - i\gamma_1 - \omega & \kappa/\omega_0 \\ \kappa/\omega_0 & \omega_0 - i\gamma_2 - \omega \end{pmatrix} \begin{pmatrix} a_0 \\ b_0 \end{pmatrix} = \begin{pmatrix} g_1/\omega_0 \\ 0 \end{pmatrix} \ . \tag{5.3}$$

Solving for a_0 and b_0 yields

$$a_0 = \frac{g_1(\omega_0 - i\gamma_2 - \omega)}{(\omega_0 - i\gamma_1 - \omega)(\omega_0 - i\gamma_2 - \omega) - \kappa^2} \tag{5.4a}$$

$$b_0 = \frac{-g_1\kappa}{(\omega_0 - i\gamma_1 - \omega)(\omega_0 - i\gamma_2 - \omega) - \kappa^2} \ . \tag{5.4b}$$

As a reminder, a_0 represents the amplitude of the bright dimer mode, and b_0, the dark waveguide resonator mode. Armed with this knowledge, we are now ready to derive more

insightful parameters of our coupled nanoantenna system.

5.1.1 Critical coupling condition

As we have seen in Chapter 4, we can control the coupling strength between the bright dimer mode and the dark waveguide resonator mode via the placement of the dimer along the waveguide, which is quantified by the displacement parameter d. We wish to investigate the optimal coupling that provides the strongest field enhancement of the fundamental field in our nanoantenna, which we call the critical coupling condition. In order to do this, we wish to maximise $|b_0|^2$ with respect to the coupling parameter κ, as the waveguide resonator mode provides the strongest field confinement, and the electric field enhancement will be proportional to

$$|b_0|^2 = \frac{\kappa^2 g_1^2}{|(\omega_0 - i\gamma_1 - \omega)(\omega_0 - i\gamma_2 - \omega) - \kappa^2|^2} \ . \tag{5.5}$$

It is challenging to evaluate this for the general case so we restrict ourselves to the case where we are exciting the mode at its resonance frequency, $\omega = \omega_0$. Taking the derivative of Equation 5.5 with respect to κ and setting it equal to zero ($d|b_0|^2/d\kappa = 0$) yields

$$\kappa^2 = \gamma_1 \gamma_2 \ . \tag{5.6}$$

We have now identified the critical coupling condition for this system where energy from the beam is optimally coupled to the dark mode. In order to experimentally verify this, we will perform SHG and THG measurements on our nanontenna in Section 5.2, as the strength of the measured nonlinear signals should be affected by the local field enhancement.

5.1.2 Extracting fitted parameters

As a final preparatory step, we need to extract the coupling parameter κ and damping parameters γ_1 and γ_2 of our nanoantenna system by fitting our coupled oscillator model to experimental data similar to the methods presented in Reference [59]. Following the derivations in References [58] and [65], we can write the transmission of the system as

$$T = 1 - \mathrm{Re}\frac{i\omega\alpha(\omega^2 - (\omega_0 + \delta)^2 + i\omega\gamma_2)}{(\omega^2 - \omega_0^2 + i\omega\gamma_1)(\omega^2 - (\omega_0 + \delta)^2 + i\omega\gamma_2) - \omega^2\kappa^2 e^{2i\phi}} , \tag{5.7}$$

where α is a scaling factor and ϕ is a phase retardation factor relating the real coupling strength κ to the complex coupling parameter, $\tilde{\kappa} = \kappa e^{i\phi}$. The complex coefficient arises due to retardation effects in the coupling due to the finite size of the nanoantenna components [58], and we find that $\tilde{\kappa}$ describes the experimental data best.

Figure 5.2a* shows the transmission data used to extract the fitted parameters from Equation 5.7. We note that there are deviations from the simulated transmissions in Figure 4.10 of the previous chapter, which we attribute to fabrication imperfections, as it is difficult to produce nanostructures with sufficient resolution at this scale. To remedy this, new simulations were performed where the models were based on SEM images of the nanoantenna sample instead of idealised geometric structures. The updated simulations and the SEM images they are based on are shown in Figures 5.2b* and 5.2c*, showing far greater agreement with the measured transmission data. The transmission at $d = 0$ nm already shows the emergence of the Fano resonance peak, as the dimer is not placed at the exact centre of the waveguide and fabrication imperfections break the structure's

*The author would like to thank Dr. Xiaofei Xiao for fabricating the sample, taking the FTIR spectra and SEM images in Figs. 5.2a and 5.2c, and assisting with the simulations in Fig. 5.2b.

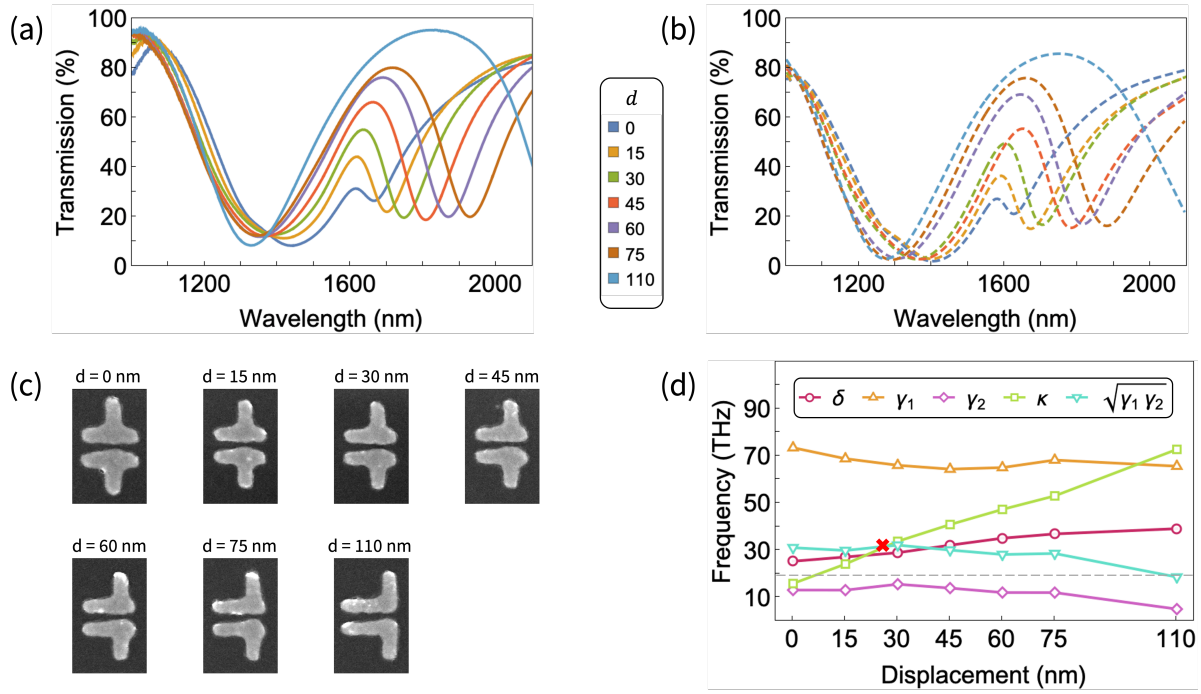


Figure 5.2: **Extraction of critical coupling parameters**. **(a)** Experimental transmission of nanoantennas with different displacements from FTIR spectra. **(b)** Simulated transmission of nanoantennas with different displacements based on SEM images in (c). **(c)** SEM images of nanoantennas that were used to model simulation structures in (b). **(d)** Extracted parameters from fitting (b) to Eq. 5.7. The grey dashed line marks the Drude damping limit of experimental thin gold films ($\sim$ 20 THz) [59], and the red X marks the critical coupling condition where $\kappa = \sqrt{\gamma_1\gamma_2}$. The FTIR spectra and SEM images in (a) and (c) were taken by Dr. Xiaofei Xiao.

symmetry, which is required to inhibit coupling to the dark mode. There is also red-shifting of the transmission peak for higher displacements which we again attribute to fabrication defects as well as deviations in the experimental permittivity of the gold due to surface scattering and grain boundary effects between the gold and substrate.

The extracted parameters for γ (detuning of waveguide resonator and dimer resonances), γ_1 (dimer damping), γ_2 (waveguide resonator damping), and κ (coupling between waveguide resonator and dimer) as well as $\sqrt{\gamma_1\gamma_2}$ for different dimer displacements are shown in Figure 5.2d. As expected, the coupling strength κ increases with the displacement d, as the placement of the dimer aligns with the higher fields at the ends of the waveguide resonator mode (see Figs. 4.6a and 4.7). The detuning δ also increases with d albeit at a smaller rate, while γ_1 andγ_2 remain roughly constant at 70 and 12 THz respectively. Of particular note is that the waveguide resonator damping lies below the Drude damping limit for gold thin films at 19.5 THz and approaches the limit for bulk gold at 6.5 THz [66, 67]. As this indicates the limit for purely non-radiative damping, the role of the waveguide as the dark resonator is confirmed, and the near total suppression of radiation from the waveguide resonator allows for strong confinement of light in the gap. The critical coupling condition identified by Equation 5.6 is indicated by the red 'X' in the figure. We thus expect that the strongest confinement and field enhancement occurs for $15 < d < 30$, and we now move to confirm this prediction with nonlinear frequency conversion measurements.

5.2 SHG and THG measurements

A simplified schematic of the experimental setup for measuring SHG and THG is shown in Figure 5.3. A Coherent Chameleon Ultra II tuneable Ti:Sapphire laser (80 MHz repetition

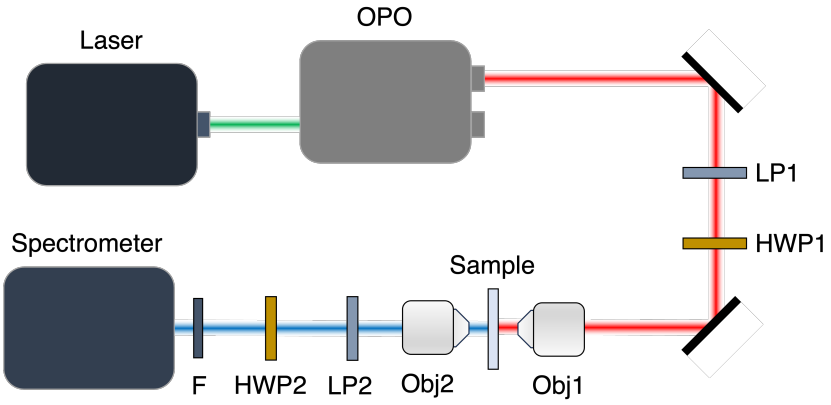


Figure 5.3: **Experimental setup for SHG/THG measurements**.

rate, ∼140 fs pulse duration) pumps a Coherent Chameleon Compact optical parametric oscillator (OPO) to produce a pump beam at 1550 nm. A linear polariser (LP1) and half-wave plate (HWP1) allows for polarisation control while ensuring the pump is linearly polarised. The pump is then focused with a Mitutoyo Plan Apo NIR 20X/0.4NA objective (Obj1) at normal incidence onto the sample, which is mounted on a piezo-controlled xyz stage, and the SHG and THG signals are collected in transmission by a Nikon S Plan Fluor 40X/0.6NA objective (Obj2). A second set of polariser and half-wave plate (LP2, HWP2) is only used when analysing the output polarisation of the nonlinear signals, and a Thorlabs FESH1000 shortpass filter (F) rejects the pump beam. The SHG and THG signals are then sent to an Acton SP2300 spectrometer for detection and analysis.

A representative spectrum displaying both SHG and THG generated from a 1550 nm pump source is shown in Figure 5.4a. As expected, the SHG and THG signals are centred at the second (∼ 775 nm) and third harmonic (∼ 517 nm) of the pump respectively. We note that the THG signal is relatively weak here, as it coincides with the absorption of gold where scattering is expected to be poor. Nonetheless, as we are primarily interested in proving the nanofocusing and critical coupling effect, the THG measurements will prove useful. To further validate the origin of the nonlinear signals, a power series measurement

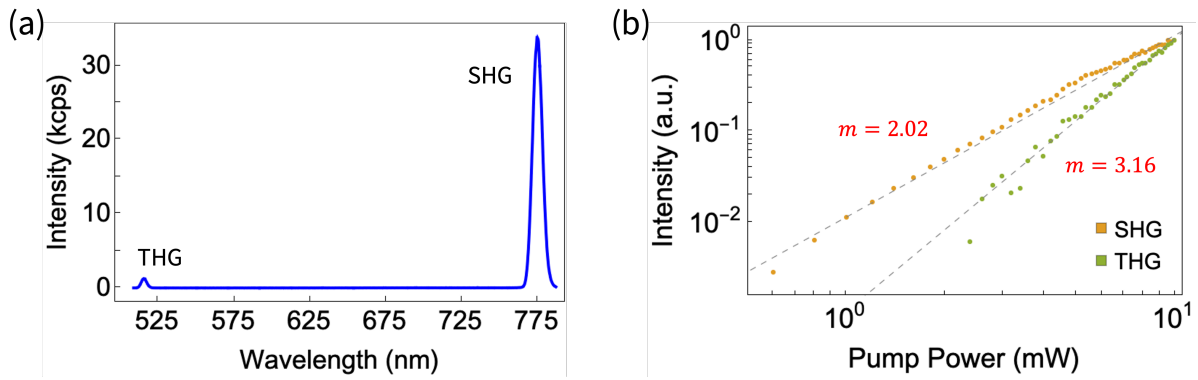


Figure 5.4: **Observation of SHG/THG in waveguide-dimer nanoantenna**. **(a)** Spectrum displaying simultaneous SHG and THG for a 1550 nm pump. **(b)** Power series for SHG/THG shown in log-log scale. The linear fit of the log-log data is shown by a dashed grey line with the slope indicated in red.

was performed, which is shown in log-log scale in Figure 5.4b. The slope of the linear fits shown in red are 2.02 and 3.16 for SHG and THG, which agrees with the quadratic and cubic power dependence of the respective processes on the pump power.

5.2.1 SHG and THG dependence on dimer displacement

As discussed in the previous section, we expect the highest enhancement for the fundamental field and the resulting nonlinear signals to occur for 15 nm $< d <$ 30 nm. To assess this in more detail, we turn once again to the SEM image-based simulations to compute the average electric field enhancement at 1550 nm in a 2D plane through the centre of the nanoantenna using the equation

$$F = \frac{\iint |E(\boldsymbol{r})|^2 dS}{|E_0|^2 S}\,, \tag{5.8}$$

where dS is the area of a unit cell as defined by the simulation mesh, S is the area surrounding the waveguide gap region, E is the local electric field, and E_0 is the field of the 1550 nm source. The field enhancement profiles of nanoantennas with four different

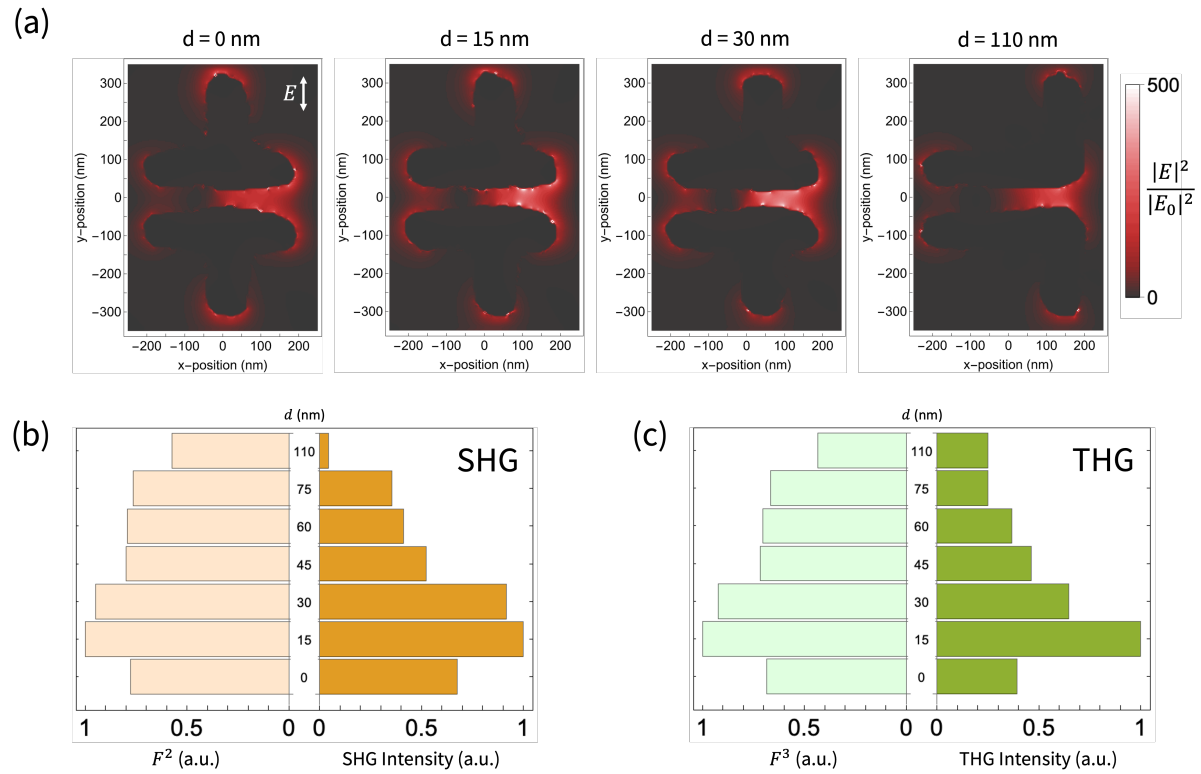


Figure 5.5: **Predicted and measured SHG/THG intensity according to dimer displacement**. **(a)** Simulated field enhancement profile using SEM images. Profiles are shown for four different dimer displacements for a y-polarised source at the fundamental wavelength of 1550 nm. **(b)** Measured SHG intensity according to dimer displacement compared to F^2. **(c)** Measured THG intensity according to dimer displacement compared to F^3.

dimer displacements are shown in Figure 5.5a.

The measured SHG and THG intensities of different dimer displacements are compared to the F^2 and F^3 values respectively in Figures 5.5b and 5.5bc. In both cases, the measured nonlinear signal increases with the displacement and peaks at $d = 15$ nm before decreasing again, which confirms our earlier prediction based on critical coupling. There is also agreement between the SHG and THG intensities and the relative strengths of F^2 and F^3 further validating our model of coupling based on dimer displacement. The discrepancy between the nonlinear intensities and absolute F^2 and F^3 values can be attributed to the simplified 2D computation of average field enhancement. For a more thorough investigation, the enhancement over a 3D volume around the nanoantenna

can be explored. Moreover, we have neglected to apply nonlinear scattering theory and consider the second and third harmonic fields and their respective overlaps with the fundamental, as the field profiles at these wavelengths contained too many artifact hot spots given the resolution of the SEM-based simulations. Therefore, a proper investigation of the simulated second and third harmonic fields is warranted to see if nonlinear scattering theory can corroborate the results presented in Figures 5.5b and 5.5c.

5.2.2 Pumping with off-axis polarisations

As a final investigation of the optical response of this nanoantenna, we deviate from the intended coupling mechanism of the dimer and illuminate the nanoantenna at polarisations that are off the dimer axis. As we have seen in Chapter 4.2, coupling to the waveguide resonator mode can only be achieved indirectly through the dimer, and we expect minimal confinement and field enhancement in the gap for off-axis polarisations. The normalised SHG and THG intensity vs pump polarisation for different displacements are shown in Figures 5.6 and 5.7. Interestingly, there is a measurable nonlinear signal when we illuminate the nanoantenna with a polarisation that is 45° off the waveguide/dimer axis for displacements $d < 30$ nm. This is most pronounced in the THG signal and can indicate the excitation of a different mode than the ones we have studied. As we move to higher displacements, the nonlinear response is quickly dominated by pump polarisations that are along the dimer axis, as the increased coupling strength between the waveguide resonator and dimer resonances directs more of the energy to the confined gap region. Still, the response at off-axis polarisations does not completely disappear for THG at higher displacements, although it appears to be absent in the case of SHG. This may indicate that different scattering mechanisms for SHG and THG are at play here, and a

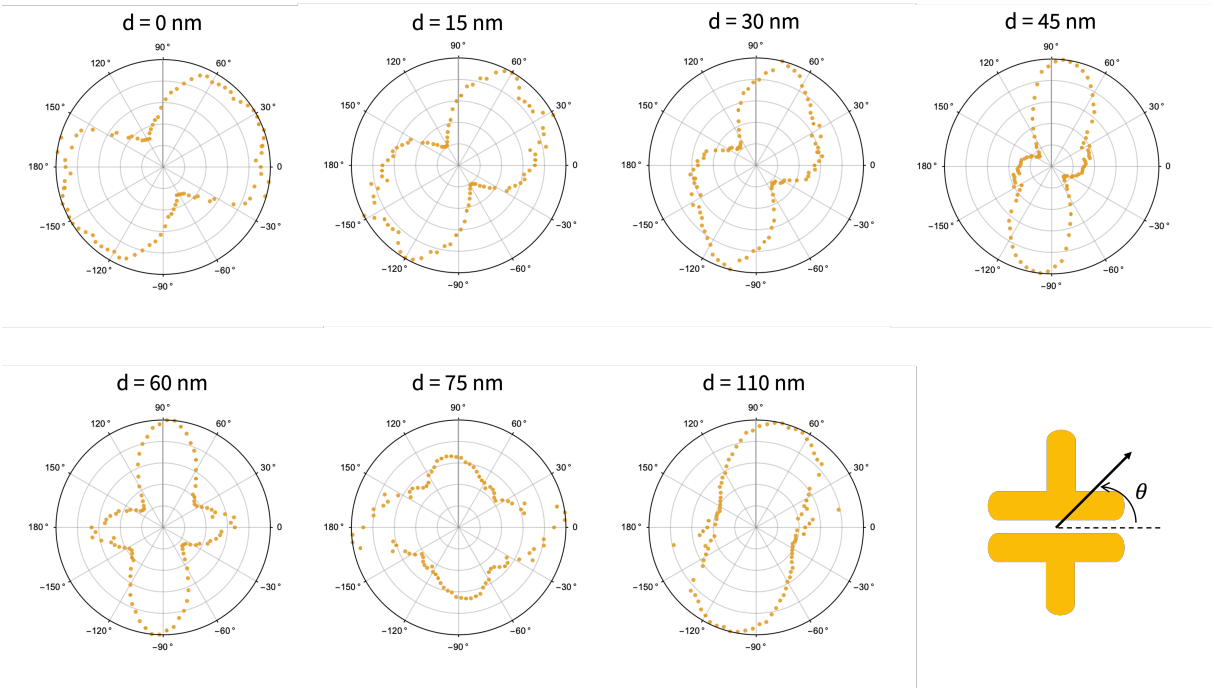


Figure 5.6: **Polarisation series for SHG**. All angles were adjusted by +7° to account for the sample mounting angle and more closely align the maximum signal with the vertical axis. Data for $-180 < \theta < 0$ is mirrored from $0 < \theta < 180$.

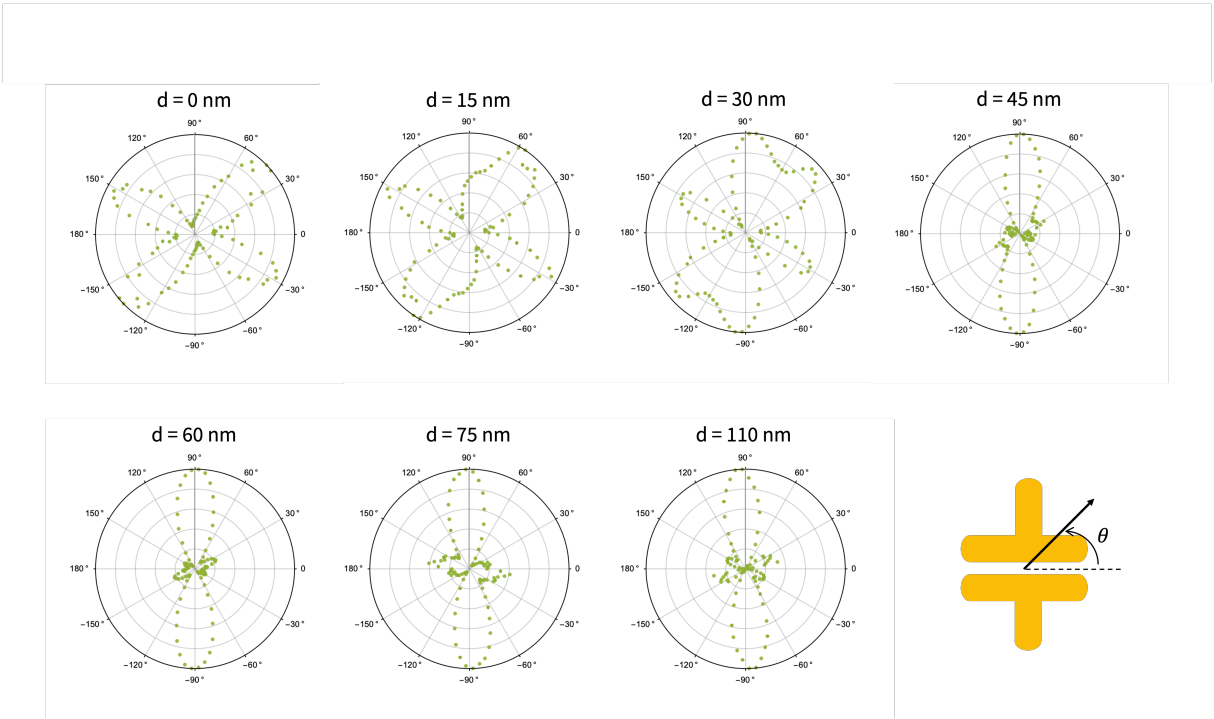


Figure 5.7: **Polarisation series for THG**. All angles were adjusted by +7° to account for the sample mounting angle and more closely align the maximum signal with the vertical axis. Data for $-180 < \theta < 0$ is mirrored from $0 < \theta < 180$.

more thorough investigation of the nanoantenna response is warranted.

5.3 Conclusion

In summary, we utilised the simulations of the waveguide-dimer nanoantenna in Chapter 4.2 to investigate the coupling of the two particles' respective resonances according to the displacement parameter. We have built on the Lorentz oscillator model introduced in previous chapters to present the coupled oscillator model which describes our coupled waveguide-dimer system. Using this model, we derived a critical coupling condition, $\kappa^2 = \gamma_1\gamma_2$, for the maximum amplitude of the waveguide resonator mode, where we predict the highest field enhancement, and by extension the highest nonlinear emission, to occur. We then identified where the critical coupling occurs in our nanoantenna by fitting experimental transmission data to the model and experimentally verified this with nonlinear measurements. Finally, we repeated the experiment for different input polarisations to verify that coupling strength and nonlinear emission is maximised when the polarisation is aligned with the dimer axis. Although we found some evidence of this occurring, particularly for higher displacement values and for THG, we also discovered that strong nonlinear emission can be generated for polarisation angles that are between the waveguide resonator and dimer axis, suggesting that other resonant modes may exist in our system.

The critical coupling mechanism demonstrated in this experiment contributes to ongoing efforts to optimise nanoantenna designs for nonlinear optics. Identifying the geometries of a particular nanoantenna configuration that allow for maximum field enhancement allows for control of nanofocusing effects to redirect optical energy to local regions of interest with nanoscale precision. The next logical step is to further boost the nonlinear

conversion efficiency we can achieve with this nanoantenna, which can be achieved in several ways. For one, we would like to adjust the dimensions of the nanoantenna to move to longer wavelengths which are further away from the absorption region of gold. Another exciting possibility is forming a hybrid nanoantenna by combining this structure with a different material. For example, we can introduce the highly nonlinear polymer MEH-PPV [68] into the gap region of the waveguide and utilise the nanofocusing mechanism to direct energy into a low-loss medium. This possibility is supported by examples in literature of hybrid plasmonic-polymer systems that have demonstrated significantly enhanced THG [69] and FWM [70]. In conclusion, we find the coupled nanoantenna investigated in this chapter to be a promising platform for furture nonlinear experiments.

Chapter 6

Four-Wave Mixing in Plasmonic Nanoantennas

In this chapter, we continue to explore the use of plasmonic nanoantennas to generate nonlinear emission with a particular emphasis on FWM. Compared to the SHG and THG experiments detailed in Chapter 5, FWM measurements present a greater challenge as we now require two input beams (pump and seed) and a more complex setup with a high level of control over the beam paths.

We begin the chapter by discussing our motivations for exploring FWM in Section 6.1. This is followed by a discussion in Section 6.2 of the sample and experimental setup used in this experiment. Section 6.3 presents our experimental results and characterisation of FWM, and Section 6.4 details a stimulated emission tomography (SET) analysis using the data we collected from this experiment. Section 6.5 concludes this chapter with a summary of our results and a discussion of the future outlook based on this experiment. This chapter expands on the work presented in References [71] and [72] and contains contributions from Dr. Mohsen Rahmani in the fabrication of the nanoantenna, Dr.

Xiaofei Xiao in the collection of SEM images, and Dr. Sylvain Gennaro in the collection of FTIR spectra.

6.1 Background and motivation

There exists a multitude of nonlinear optical processes, each with their own associated motivations and applications. In particular, strong interest has been shown in SPDC for generating entangled photon-pairs, as has been demonstrated in a variety of nonlinear media including nanoantennas [40], metasurfaces [73], and thin films [74]. The alternative method for producing entangled photon-pairs via nonlinear optics is SFWM, which has not received the same level of attention in recent literature. One of the reasons for this may be that SFWM is a third-order nonlinear process, while SPDC is a second-order process, and $\chi^{(3)}$ nonlinearities tend to be weaker than $\chi^{(2)}$ in many materials [3]. However, there are several advantages to SFWM, which make it an attractive option for nanoscale photon-pair sources and provide the motivation for the direction of this experiment.

6.1.1 The case for spontaneous four-wave mixing

First, SFWM allows for a more diverse range of candidate nonlinear materials, as only non-centrosymmetric materials possess an intrinsic $\chi^{(2)}$ nonlinearity, while all materials exhibit $\chi^{(3)}$ nonlinearity (see Ch. 2.2). Although there are exceptional cases where centrosymmetric materials can facilitate second-order processes at the material surface [3, 75, 76] or induce symmetry-breaking geometries [63, 77, 78], the lifting of this restriction cannot be understated, as this invites research into a much broader range of materials.

Second, nanoscale nonlinear optics requires the use of ultrafast pulses with high peak powers due to the exceedingly small nonlinear conversion efficiencies with reduced in-

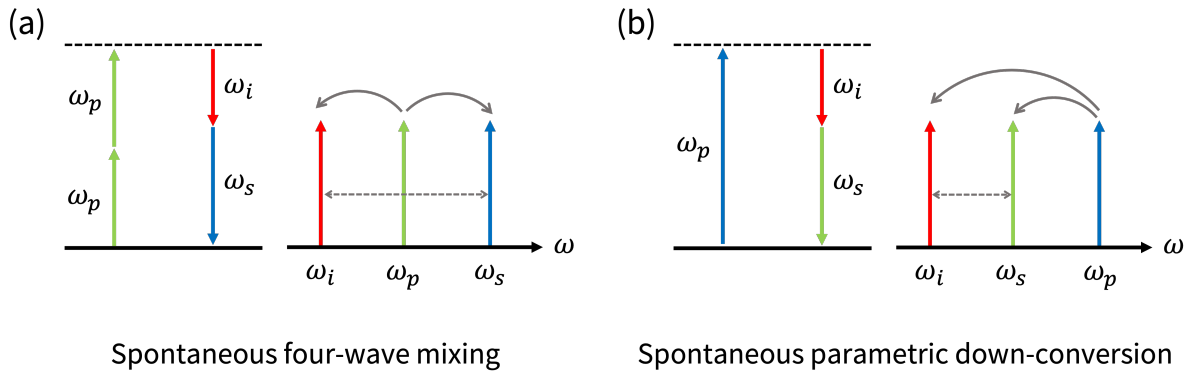


Figure 6.1: **Energy level diagrams for SFWM and SPDC**. **(a)** In SFWM, two pump photons are annihilated to produce a signal/idler pair. As shown in the relative energy diagram, the signal/idler photons are up-/down-converted from the pump photon, which shows potential for a broadband signal/idler pair. The bandwidth of the signal/idler pair is indicated by the dashed grey line. **(b)** In SPDC a single pump photon is annihilated to produce a signal/idler pair. Both the signal and idler photons are down-converted from the pump, with a potentially narrower bandwidth indicated by the dashed grey line.

teraction volumes relative to conventional nonlinear optics in bulk crystals [79]. In this context, SFWM is particularly well-suited for taking advantage of the high peak powers, because it scales quadratically with the pump (Chapter 2.4.2, Equation 2.29). SPDC, on the other hand only scales linearly with pump power and thus cannot fully take advantage of pulsed mode operation.

Finally, SFWM allows for greater flexibility in producing highly non-degenerate signal and idler wavelengths, because it produces one up-converted and one down-converted photon with energies that are higher and lower than the pump, respectively (Figure 6.1). SPDC, on the other hand, produces two down-converted photons that are both at lower energies than the pump. Highly non-degenerate photon-pairs are desirable for heralded single photon sources where the wavelength of the trigger photon is within the sensitivity range of silicon photodiodes and the heralded photon lies in the telecommunication band [80]. Another application for such non-degenerate photon-pairs is imaging with undetected photons, where the detected photon again lies in the visible range and the probe photon

lies in the near- and mid-infrared regions which are of particular interest for biomedical sensing applications [81].

6.1.2 Stimulated emission tomography

Regardless of whether one uses SFWM or SPDC to generate photon-pairs, it is crucial to characterise the spectral entanglement of the signal and idler photons, and this is an difficult task for experiments using nanoantennas and metasurfaces as the generation rates in these materials are exceedingly low. Traditionally, quantum state tomography (QST) is performed to reconstruct the density matrix describing a two-level photonic system via coincidence measurements [82], but this method requires single photon detectors and long integration times while suffering from poor signal-to-noise ratio [83]. SET, an alternative method proposed by Liscidini and Sipe [84], greatly simplifies this task and avoids the use of single photon detectors by establishing a relationship between a spontaneous parametric process and its stimulated analogue [84, 85],

$$\frac{\langle n_{\omega_s} \rangle_{A_{\omega_i}}}{\langle n_{\omega_s} n_{\omega_i} \rangle} \approx |A_{\omega_i}|^2 \ , \tag{6.1}$$

where $\langle n_{\omega_s} \rangle_{A_{\omega_i}}$ is the average number of signal photons with frequency ω_s that is stimulated by a seed beam at the idler frequency ω_i, $\langle n_{\omega_s} n_{\omega_i} \rangle$ is the average number of signal/idler pairs that would have been generated in a spontaneous process without the seed beam, and $|A_{\omega_i}|^2$ is the average number of idler photons within the coherence time of the seed beam.

Equation 6.1 allows for an indirect characterisation of spontaneous nonlinear processes like SFWM by performing a classical measurement of stimulated FWM which is a much brighter process that can be detected with conventional photodiodes, thus alleviating the

need for single photon detectors and long detection times. Furthermore, it is possible to recover the joint spectral density (JSD) of the spontaneous process by scanning the seed beam across the range of idler wavelengths of interest. The JSD obtained in this manner is of higher resolution than that of spectrally resolved coincidence measurements and is limited only by the linewidth of the seed beam [83, 85–87].

6.1.3 Summary

In the following sections we will demonstrate the generation of FWM in plasmonic nanoantennas and use SET to assess the SFWM generation rate that can be achieved. We provide a full characterisation of the SFWM process by studying both the up- and down-conversion cases within our SET analysis and producing a JSD map. Whereas previous demonstrations of the SET technique have either used nonlinear crystals [87–89], waveguides [83], or optical fibres [85, 86], here, we demonstrate for the first time, to our knowledge, SET analysis of a sub-wavelength source.

It should be stated that for the purpose of developing practical devices for photon-pair generation, plasmonic structures may prove to be unsuitable. In particular, plasmonic nanoparticles can generate a high amount of fluorescence [22], and this can hinder any attempt to isolate a nonlinear signal. However, they still provide a direct measure of the strength of a nonlinear process, and thus their use in the characterisation of nonlinear processes like FWM is still valuable.

6.2 Sample and experimental setup

For this experiment, we used the bar and discs nanoantenna configuration which we have studied in Chapter 4.3. As a reminder, the nanoantenna consists of a bar particle that

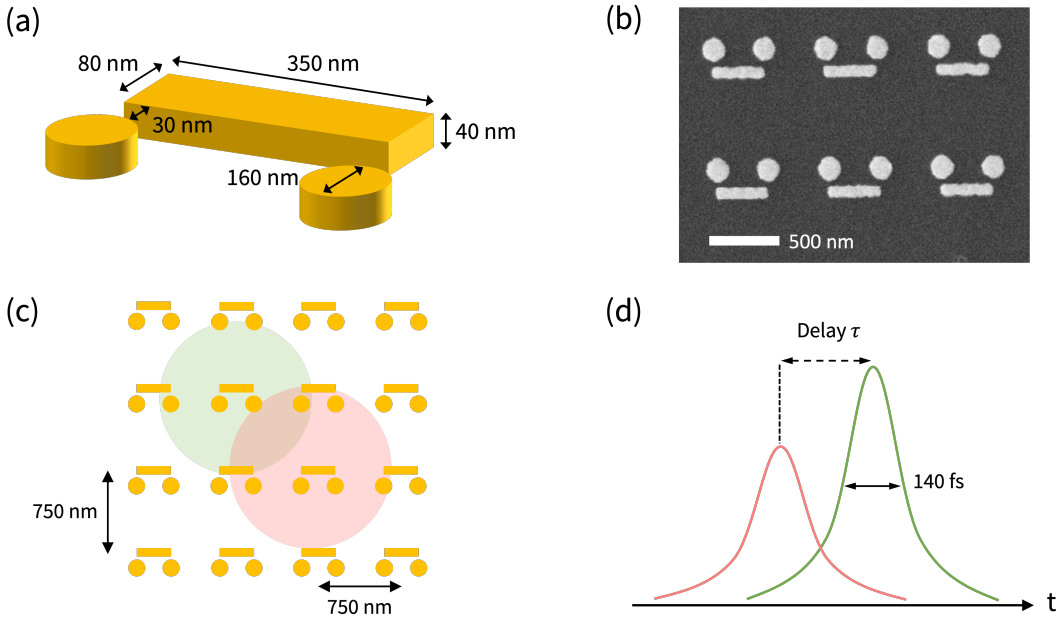


Figure 6.2: **Bar-discs nanoantenna**. **(a)** Illustration of nanoantenna with dimensions. **(b)** SEM image of nanoantenna array. **(c)** Diagram of spatial beam overlap on nanoantenna array. The pump beam in green and the seed beam in red is drawn to approximate the scale of the beams relative to the antenna array and are shown out of alignment here. **(d)** Diagram of temporal beam overlap. The pulse width of the beams is approximately 140 fs. The SEM image in (b) was taken by Dr. Xiaofei Xiao.

supports dual resonances near 1500 nm and 750 nm and two discs that are resonant near 750 nm. The nanoantenna geometry and an SEM image of the sample are shown in Figure 6.2.* The sample itself consists of a square array of individual nanoantennas in a 750 nm x 750 nm unit cell, with a 1.5 nm chromium adhesion layer between the nanoantennas and the silica substrate and an additional silica capping layer deposited on top of the nanoantennas. We wish to evaluate the performance of individual nanoantennas and thus will be focusing our excitation beams to the scale of the unit cell. This also maximises the power density of the pump and seed beams that can be delivered to the nanoantenna while remaining under the damage threshold. Illuminating individual nanoantennas poses a significant challenge, however, as this requires painstaking alignment and a high degree of control of the optical setup to overlap the beams in the correct positions, as diagramed in Figure 6.2c. In addition, as we are utilising a pulsed laser system, we need to delay one of the beam paths to ensure that the pulse trains arrive at the nanoantennas at the same time (Figure 6.2d).

6.2.1 Dual-beam setup

A simplified schematic of the pump-probe setup used for this experiment is shown in Figure 6.3. The setup is modified from the one presented in Chapter 5 with some key differences. We use the same tuneable Ti:Sapphire laser and OPO to produce the pump and seed beams respectively. For the main SET analysis, the central pump wavelength is designated to be 840 nm. In up-conversion measurements, the seed wavelength is 1500 nm, which generates a FWM signal near 583 nm when combined with the pump. In

*The author would like to thank Dr. Mohsen Rahmani for fabricating the sample and Dr. Xiaofei Xiao for taking the SEM image in Fig. 6.2b.

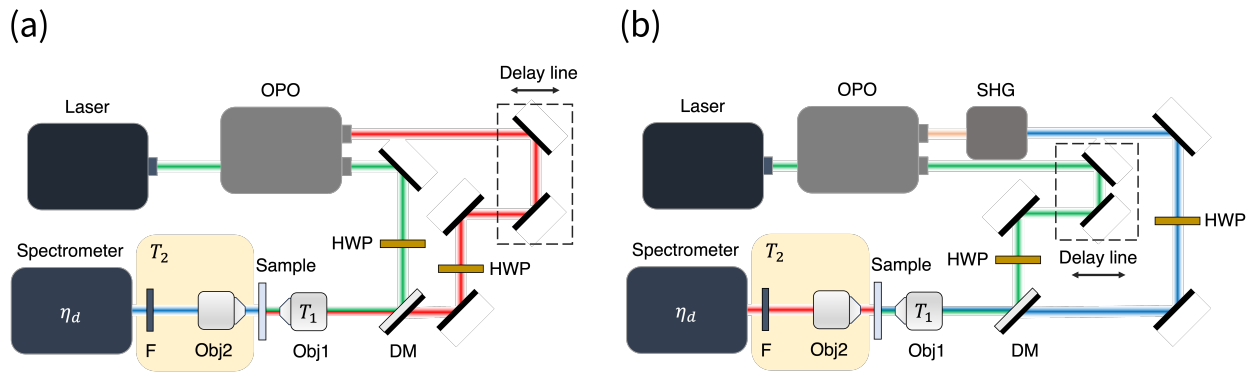


Figure 6.3: **Experimental setup for four-wave mixing**. **(a)** Up-conversion setup with 840 nm pump (green), 1500 nm seed (red), and 583 nm FWM signal (blue). **(b)** Down-conversion setup with 840 nm pump (green), 583 nm seed (blue), and 1500 nm FWM signal (red). In this configuration, the OPO output pumps a frequency doubler that converts brings an 1166 nm signal to 583 nm. Note that the pump line is delayed in this configuration, but the seed line is delayed in up-conversion.

down-conversion measurements, the OPO output at 1166 nm further pumps an APE HarmoniXX SHG frequency doubler (SHG in figure) to convert the seed wavelength to 583 nm, which then generates a FWM signal near 1500 nm when combined with the same pump. The tuneability of this setup allows for scanning both the pump and seed wavelength around the ranges mentioned above. Temporal overlap is achieved with the inclusion of a delay line controlled by a Thorlabs DDS220/M stage and retroreflector.

Half-wave plates (HWP) in each of the pump and seed paths control the polarisation, and the two beams are overlapped on either a Thorlabs DMSP1180 dichroic mirror (DM) for up-conversion or DMSP805 for down-conversion. The beams are focused collinearly by a Nikon Plan Apochromat 60X/0.95NA objective (Obj 1) onto the sample at normal incidence. The sample is mounted on a piezo-controlled xyz-stage to bring the nanoantenna to the correct position and focus of the beam path. The generated FWM signal is then collected in transmission by a Nikon S Plan Fluor 40X/0.6NA objective (Obj 2) and directed to the Acton SP2300 spectrometer for analysis. In addition there is either a Thorlabs FESH700 shortpass or FELH1100 longpass filter (F) in front of the spectrometer

to reject the pump and seed beams for up-conversion and down-conversion respectively.

As we will see in Section 6.4, we take into account the transmittance of the focusing objective (T_1), the collection efficiency of the collection objective (η_c), the transmittance of the entire FWM path from sample to spectrometer (T_2), and the detection efficiency of the spectrometer (η_d) in this experimental setup.

6.3 Observation of four-wave mixing

With proper spatial alignment and temporal overlap of the pump and seed beams, we are able to observe frequency mixing in the nanoantennas. Figure 6.4a shows a representative spectrum of FWM, sum-frequency generation (SFG), and THG, which we are able to observe simultaneously due to the relaxation of phase-matching restraints in the sub-wavelength volume of the nanoantenna. The frequency of the THG signal at 500 nm is the third harmonic of the 1500 nm seed beam, while the frequency of the SFG signal at 538 nm is the sum of the pump and seed frequencies, according to $\omega_{SFG} = \omega_p + \omega_s$. Figure 6.4b shows a combined spectrogram of the three signals which is composited from multiple spectra taken at varying delays between the pump and seed pulses by translating the delay line in 10 µm steps ($\sim$ 66 fs). We note that the FWM and SFG signals only appear for delays consistent with the temporal overlap of the pump and seed beams, while the THG signal persists for all delays as it is generated solely by the 1500 nm seed beam. The dependency of the nonlinear signal on the arrival times of the pulses amounts to a gating effect, and this has been exploited to provide a complete characterisation of the pulses via a technique called frequency-resolved optical gating in Reference [90].

Figure 6.4c takes a closer look at the FWM signal, and Figure 6.4d shows the spectrogram for down-conversion FWM with a 840 nm pump and 583 nm seed. A prominent

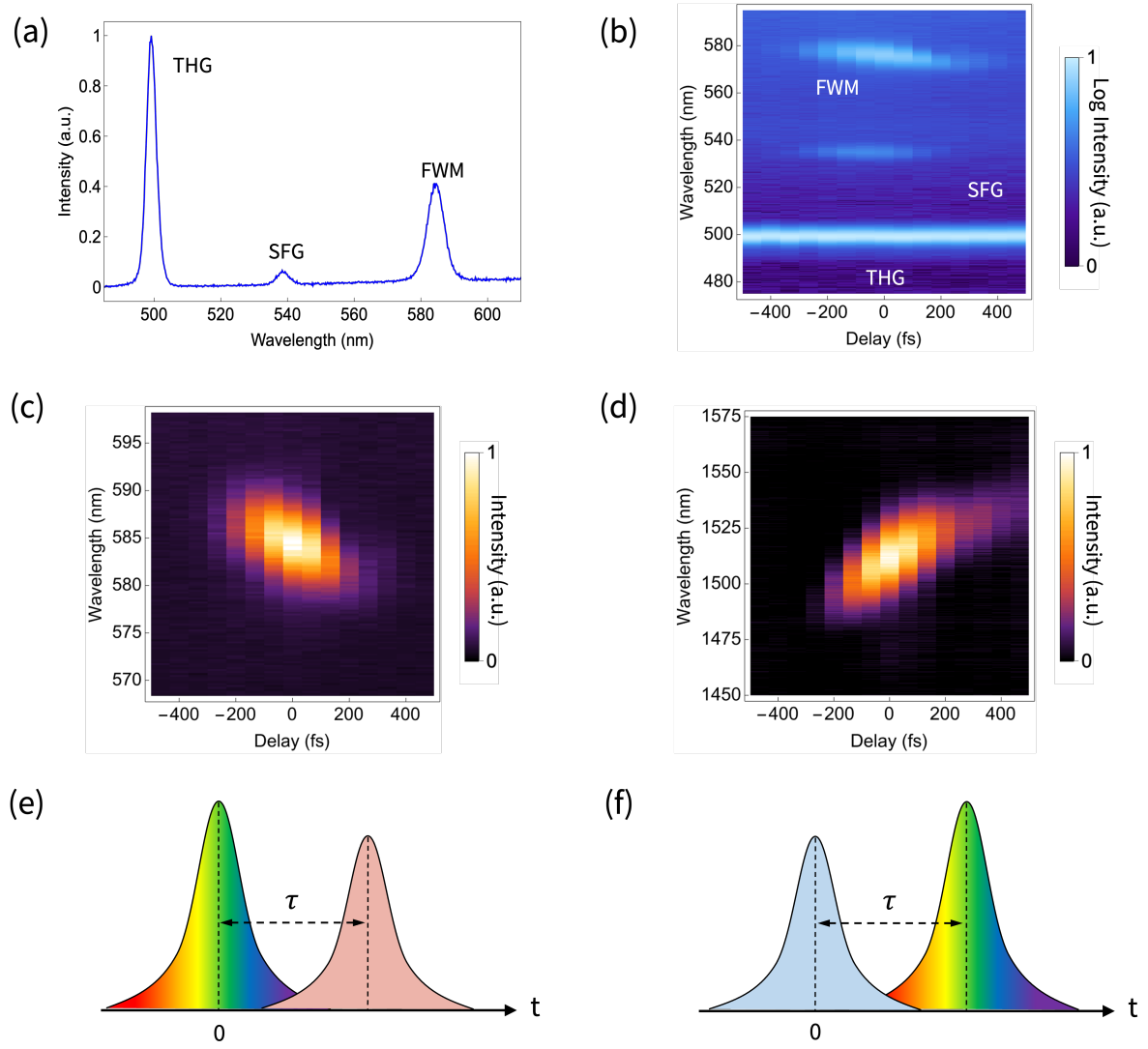


Figure 6.4: **Spectra of nonlinear processes in bar-discs nanoantenna**. **(a)** Spectrum showing simultaneous THG, SFG, and FWM. The wavelengths of the pump and seed beams are 840 nm and 1500 nm respectively. **(b)** Spectrogram of wavelength vs delay showing simultaneous THG, SFG, and FWM. The intensity is shown in logarithmic scale to highlight all three processes. The spectrum in (a) was taken at 0 fs delay. **(c)** A closer look at the spectrogram for up-conversion FWM in (b). **(d)** Spectrogram for down-conversion FWM with 840 nm pump and 583 nm seed. **(e)** Diagram of the pump (rainbow) and seed (red) pulses over time with delay $\tau > 0$, for up-conversion FWM. **(f)** The same diagram as in (e) with the pump being delayed instead of the seed (blue pulse), for down-conversion FWM.

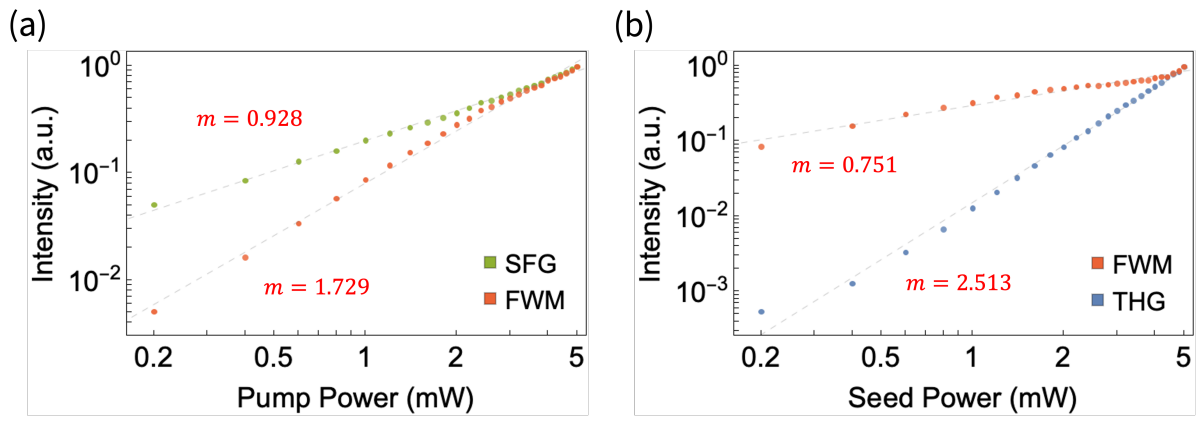


Figure 6.5: **Power series of nonlinear processes in bar-discs nanoantenna for**: **(a)** varying pump power with seed fixed at 1 mW and **(b)** varying seed power with pump fixed at 1 mW. The data is shown in log-log scale with the dashed lines representing the linear fit for each process and the slope of the fit shown in red.

feature revealed by these spectrograms is the presence of chirp in the FWM signals. This is attributed to the normally dispersive optics in the beam path resulting in the pump pulse broadening over time, with the lower frequencies arriving faster than the higher ones. Therefore, in the up-conversion setup the seed pulse interacts with the higher/lower frequency tail end of the pump pulse when the delay is positive/negative, resulting in the frequency shift exhibited in the spectrogram (Fig. 6.4e). In the down-conversion setup, the pump pulse is delayed instead of the seed pulse, and the chirp orientation of the FWM signal is reversed (Fig. 6.4f).

Power series measurements were again performed to validate the genuineness of the nonlinear signals and confirm their dependence on both the pump and seed powers. In terms of the pump power, FWM should scale quadratically while SFG should scale linearly. For the seed power, however, FWM has a linear dependence, while THG has a cubic dependence. The power series for the pump and seed beams were conducted while holding the power of the other beam constant. Fitting the slope of each curve in log-log scale revealed the dependence of SFG and FWM on the pump power to be 0.928 and 1.729

respectively, which is close to the expected values of 1 and 2 (Figure 6.5a). In terms of the seed power, the fitted slopes for FWM and THG were 0.751 and 2.513 respectively, close to the expected values of 1 and 3 (Figure 6.5b).

6.3.1 Delay shift with wavelength tuning

Before constructing the JSD maps for SFWM by scanning the seed beam, special care must be given to producing a consistent representative spectrum at each wavelength, including optimising the delay between the two pulses. It was initially assumed that once temporal overlap of the pump and seed beams was achieved with a given delay, the delay would persist as the pump and seed beams were tuned to different wavelengths. However, it was later found that the laser-OPO system used in this experiment exhibits non-uniform pulse timings across both pump and seed wavelengths. In order to investigate this, spectrograms for FWM were collected for all combinations of pump wavelength from 810–840 nm and seed wavelength from 1450–1550 nm in 10 nm steps. Figure 6.6 shows the tabulation of all spectrograms according to pump and seed wavelengths.

When moving to higher pump wavelengths (from left to right in Figure 6.6), the FWM signal shifts monotonically to lower delays. When moving to higher seed wavelengths (top to bottom), the signal is initially constant but begins shifting to lower delays starting at 1480 nm, eventually reaching a minimum at 1500 nm before shifting to higher delay again. These observations are summarised in Figure 6.7. This information was crucial for producing the JSD plots in the following section, as remaining at a constant delay while scanning the seed wavelength would result in a sub-optimal FWM spectrum.

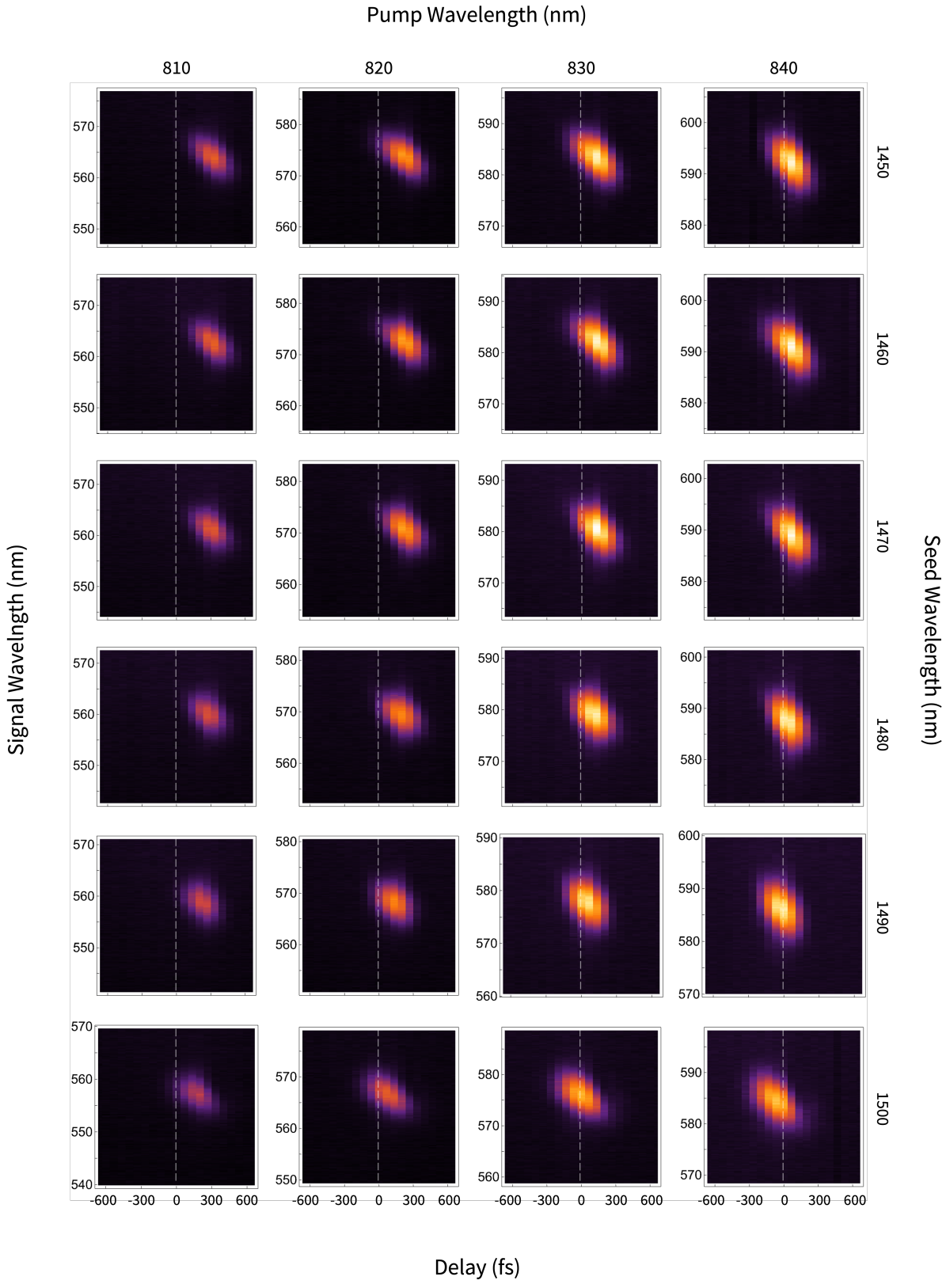


Figure 6.6: **Delay shift according to pump/seed wavelength**. Spectrograms are tabulated by pump (810–840 nm) and seed (1450–1550 nm) wavelength. The dashed white line indicates zero delay to better observe shifts in the delay timing according to wavelength. All intensities are normalised to the highest peak intensity among the pump/seed wavelength combinations.

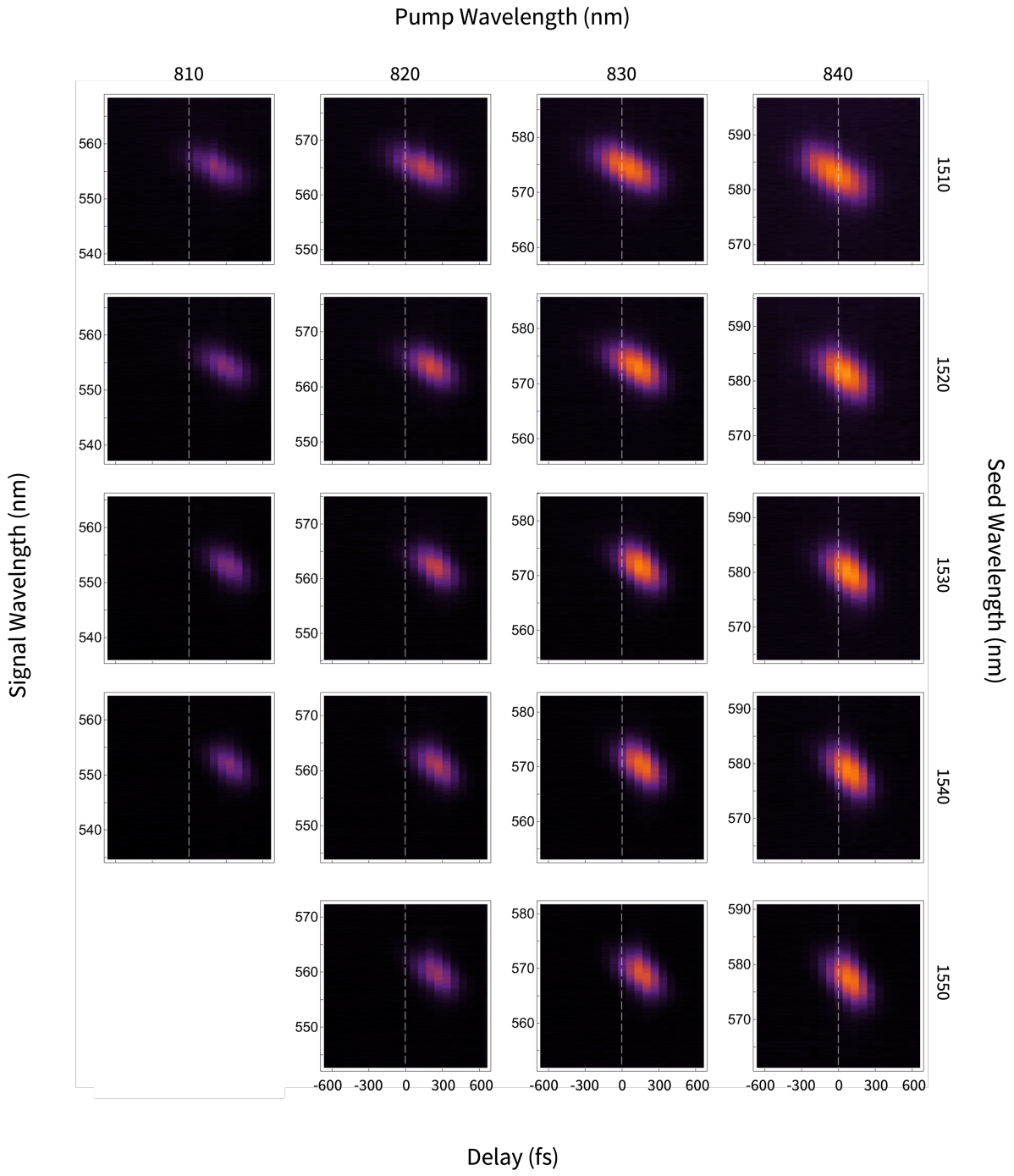


Figure 6.6: **Delay shift according to pump/seed wavelength (continued)**. Spectrograms are tabulated by pump (810–840 nm) and seed (1450–1550 nm) wavelength. The dashed white line indicates zero delay to better observe shifts in the delay timing according to wavelength. All intensities are normalised to the highest peak intensity among the pump/seed wavelength combinations. The spectrogram for 810 nm pump and 1550 nm seed is not available as the OPO was unable to output a stable seed beam at this wavelength combination.

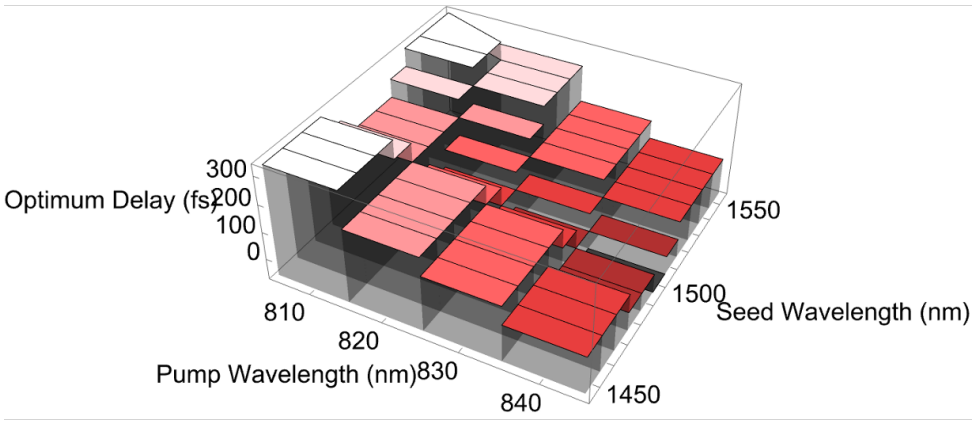


Figure 6.7: **Optimum delay for peak FWM signal according to pump/seed wavelength**.

6.3.2 JSD characterisation

Having observed the FWM signals for both up- and down-conversion and identified the optimum delay for each wavelength, we can now apply SET to construct JSD maps of SFWM signal-idler pairs by scanning the wavelength of the seed beam in 10 nm steps. Figure 6.8 shows the JSD maps for (a) up-conversion FWM, (b) down-conversion FWM, and (c) SFG. The SFG plot here is shown for reference and is constructed through the same procedure as FWM—it is worth noting that although the SFG and FWM signals are collected simultaneously in one spectrum, the optimum delay for SFG is slightly different from Figure 6.7, while showing similar trends. The resolution of these maps is limited by the linewidth of the seed beam produced by our OPO system which has a full width at half maximum (FWHM) value of ~ 20 nm.

In all three plots, the signal wavelength shifts linearly with the seed wavelength, which reflects the energy conservation of both FWM ($\omega_{\mathrm{FWM}} = 2\omega_p - \omega_s$) and SFG ($\omega_{\mathrm{SFG}} = \omega_p + \omega_s$), and further validates the occurrence of frequency mixing processes. Notably, the JSD for FWM is extremely broad showing the lack of phase-matching in an individual optical antenna. The FWM appears to be optimal near 1470 nm for up-conversion and

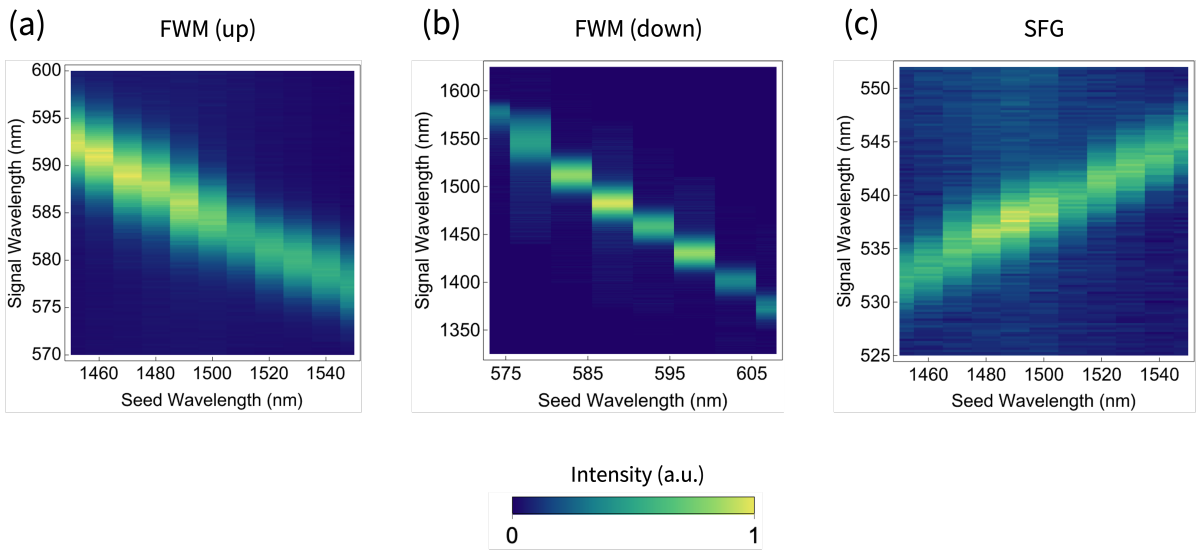


Figure 6.8: **Joint spectral density**. **(a)** Up-conversion SFWM. **(b)** Down-conversion SFWM. **(c)** SFG. All three maps were produced with an 840 nm pump.

590 nm for down-conversion which can be attributed to the dipole resonance of the bar as described in Chapter 4.3. The tuning range of the OPO system limits the seed wavelengths accessible, and thus the JSD maps appear incomplete as the antenna resonance is much broader than the seed wavelength range. Furthermore, the JSD map for down-conversion FWM was significantly more difficult to produce due to a higher signal-to-noise ratio resulting from a weaker signal and less efficient detector coupled with the presence of background fluorescence from the gold. Despite this, it has been demonstrated that the SET technique can be used to identify narrow resonant features in frequency mixing signals and produce insights into a SFWM experiment producing spectrally correlated photon-pairs.

6.4 Estimating SFWM generation rate

We have seen how SET can produce high resolution JSD maps of parametric processes, which is in itself a powerful application. However, the full power of the SET technique is on

display when utilising Equation 6.1 to assess the generation rate of spontaneous processes. We detail in this section the application of SET to estimate the SFWM photon-pair generation rate, but first we need to calculate the rate of incoming stimulating photons and generated FWM photons from our classical stimulated FWM experiment.

The rate of stimulating photons, $\dot{n}_{\mathrm{s}}$, is calculated from the stimulating seed beam power coupled to the antenna, $\bar{P}_{\mathrm{s}}$,

$$\dot{n}_{\mathrm{s}} = \frac{\bar{P}_{\mathrm{s}}}{\hbar\omega_{\mathrm{s}}} = \frac{P_{\mathrm{s}} T_{1,\mathrm{s}} \sigma_{\mathrm{s}}}{\hbar\omega_{\mathrm{s}} A_{\mathrm{s}}}, \tag{6.2}$$

where P_{s} is the seed beam power at the input of the focusing objective, $T_{1,\mathrm{s}}$ is the transmission of the objective at the seed wavelength, σ_{s} is the antenna cross-section at the seed wavelength, ω_{s} is the central frequency of the seed beam, and A_{s} is the area of the seed beam at the focus. We utilise the antenna cross-section here to approximate the nonlinear interaction occurring within a single nanoantenna. In practice, the size of our pump and seed beams at focus suggests we are illuminating several nanoantennas simultaneously. However, as this assumes perfect spatial overlap of the pump and seed beams, and we have witnessed the extinction and re-emergence of the nonlinear signals as we translate the sample by the unit cell distance, we find the single-antenna approximation to be acceptable for predicting our final results to within an order of magnitude.

To calculate the rate of FWM photons generated at the nanoantenna, $\dot{n}_{\mathrm{FWM}}$, the detector count rate, $\dot{n}_{\mathrm{cnt}}$, is divided by the total transmittance of the optical system between the particle and detector at the FWM wavelength, T_2, and the detector efficiency at the FWM wavelength, η_d,

$$\dot{n}_{\mathrm{FWM}} = \frac{\dot{n}_{\mathrm{cnt}}}{T_2 \eta_{\mathrm{d}}}. \tag{6.3}$$

We can now use Equation 6.1 to relate the spontaneous four-wave mixing rate to the stimulated four-wave mixing rate,

$$\dot{n}_{\mathrm{SFWM}} = \frac{\dot{n}_{\mathrm{FWM}}}{\dot{n}_{\mathrm{s}}}\,\Omega\ , \tag{6.4}$$

where we have multiplied the SET ratio by the repetition rate of our laser-OPO system, Ω, to recognise that FWM occurs within each pulse of the pump and seed beams, with the pulse duration determining the coherent interaction time.

Since the SFWM generation rate scales quadratically with the pump power coupled to the antenna, $\dot{n}_{\mathrm{SFWM}} \propto \bar{P}_{\mathrm{p}}^2$, we define a power-independent generation efficiency,

$$R_{\mathrm{SFWM}} = \frac{\dot{n}_{\mathrm{SFWM}}}{\bar{P}_{\mathrm{p}}} = \left(\frac{\hbar\omega_{\mathrm{s}}}{P_{\mathrm{p}}P_{\mathrm{s}}}\right)\left(\frac{\dot{n}_{\mathrm{cnt}}}{T_{1,\mathrm{p}}T_{1,\mathrm{s}}T_2\eta_{\mathrm{d}}}\right)\left(\frac{A_{\mathrm{p}}A_{\mathrm{s}}}{\sigma_{\mathrm{p}}\sigma_{\mathrm{s}}}\right)\Omega\ . \tag{6.5}$$

Here, we have substituted Equations 6.2–6.4 as well as $\bar{P}_{\mathrm{p}} = P_{\mathrm{p}}T_{1,\mathrm{p}}\sigma_{\mathrm{p}}/A_{\mathrm{p}}$, which accounts for the pump power at the input of the objective, P_{p}, the objective transmission at the pump wavelength, $T_{1,\mathrm{p}}$, the antenna's cross section at the pump wavelength, σ_{p}, and the pump beam area A_{p}.

The transmissions ($T_{1,\mathrm{p}}$, $T_{1,\mathrm{s}}$, T_2), beam areas (A_{p}, A_{s}), and detector efficiency (η_{d}) were measured and calibrated in the experimental set-up for both up- and down-conversion wavelengths (see Fig. 6.3), while the antenna cross sections at the pump and seed wavelengths (σ_{p}, σ_{s}) were estimated by multiplying the extinction shown in Figure 6.9[†] by the 750×750 nm^2 unit cell of the nanoantenna. All of the above calibration parameters are collected in Table 6.1.

[†]The author would like to thank Dr. Sylvain Gennaro for taking the FTIR spectra and Dr. Xiaofei Xiao for assisting with the simulations in Figs. 6.9a and 6.9b.

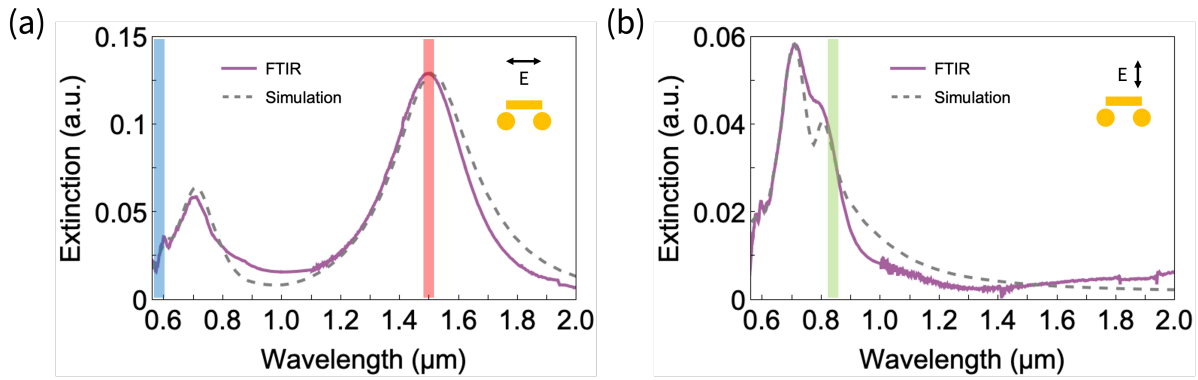


Figure 6.9: **Extinction of bar-discs antenna for**: **(a)** polarisation parallel to the bar, and **(b)** polarisation perpendicular to the bar. In both figures, the measured FTIR spectrum is shown by the solid purple line and the simulated extinction spectrum by the dashed grey line. The blue and red vertical bars in (a) indicate the down-conversion (583 nm) and up-conversion (1500 nm) wavelengths respectively, and the green bar in (b) indicates the pump wavelength (840 nm). The FTIR spectra in (a) and (b) were taken by Dr. Sylvain Gennaro.

We are now equipped to estimate the SFWM pair generation rate of our plasmonic nanoantennas from our stimulated FWM data. We first consider the case of up-conversion FWM with $\lambda_p \approx 840$ nm, $\lambda_s \approx 1500$ nm, and $\lambda_{FWM} \approx 583$ nm. Using Equations 6.2 and 6.3, we calculate $\dot{n}_s \approx 2.58 \times 10^{14}$ photons per second and $\dot{n}_{FWM} \approx 6.43 \times 10^6$ photons per second respectively. Applying Equation 6.5 yields $R_{SFWM} \approx 84.9$ photon pairs per second per mW and per nanoantenna. In the down-conversion case, the seed and signal wavelengths are interchanged such that $\lambda_p \approx 840$ nm, $\lambda_s \approx 583$ nm, and $\lambda_{FWM} \approx 1500$ nm. Applying the same methodology as above yields a spontaneous pair generation rate of $R_{SFWM} \approx 187$ photon pairs per second per mW and per nanoantenna. The above results are summarised in Table 6.2.

There are several observations to note here. First, the difference in the up- and down-conversion values can be attributed to several factors. The overall detection efficiency (η_d in Equation 6.3) was calculated separately for the up- and down-conversion wavelengths, and as each value carries its own level of uncertainty, the resulting spontaneous rates can

	Up-conversion	Down-conversion
$\dot{n}_{\mathrm{cnt}}$	35200 s^{-1}	4610 s^{-1}
P_{p}	2 ± 0.03 mW	3 ± 0.03 mW
P_{s}	2 ± 0.03 mW	1 ± 0.02 mW
$T_{1,\mathrm{p}}$	0.598 ± 0.030	0.598 ± 0.030
$T_{1,\mathrm{s}}$	0.317 ± 0.013	0.887 ± 0.034
T_2	0.797 ± 0.032	0.263 ± 0.013
η_{d}	0.00687 ± 0.0007	0.00110 ± 0.0001
A_{p}	6.79 $\mu\mathrm{m}^2$	6.79 $\mu\mathrm{m}^2$
A_{s}	7.80 $\mu\mathrm{m}^2$	1.18 $\mu\mathrm{m}^2$
σ_{p}	0.133 $\mu\mathrm{m}^2$	0.133 $\mu\mathrm{m}^2$
σ_{s}	0.420 $\mu\mathrm{m}^2$	0.0875 $\mu\mathrm{m}^2$
Ω	80 MHz	80 MHz

Table 6.1: Experimental parameters for SFWM generation rates.

vary considerably. Furthermore, recall that the nanoantennas support a resonance near 1500 nm for the wavelengths of interest in this experiment. In the case of up-conversion, this resonance aligns with the seed wavelength, while in down-conversion this occurs at the signal wavelength. This difference is non-trivial and may further contribute to the rate discrepancy. Second, for reasons discussed above, the nanoantenna sample in this work is not optimised for FWM emission, and the range of wavelengths we work with are constrained by our laser and OPO system. Using multi-resonant antennas potentially at different wavelength combinations may increase the pair generation rate. Finally, we have operated with relatively low pump powers (2 mW for up-conversion and 3 mW for down-conversion) due to the damage threshold of our gold nanoantennas. There is potential here to increase the pair generation rate further by moving to a metasurface design and illuminating a wide area of nanoantennas with higher average pump power.

	Up-conversion	Down-conversion
$\dot{n}_{\mathrm{s}}$	2.58×10^{14} s^{-1}	1.93×10^{14} s^{-1}
$\dot{n}_{\mathrm{FWM}}$	6.43×10^{6} s^{-1}	1.59×10^{7} s^{-1}
$\dot{n}_{\mathrm{SFWM}}$	1.99 s^{-1}	6.57 s^{-1}
R_{SFWM}	84.9 s^{-1} mW^{-1}	187 s^{-1} mW^{-1}

Table 6.2: SFWM photon-pair generation rates

6.5 Conclusion

In this chapter, we have provided the motivations for investigating FWM with the bar-discs nanoantenna and have taken the necessary steps to fully characterise the pulse timings of our laser-OPO system in preparation for a SET experiment. We observed FWM along with THG and SFG in approximately single nanoantennas and used the SET framework to construct JSD maps of up- and down-conversion SFWM with high resolution relative to the acquisition time. As the highlight of this experiment, we again utilised SET to estimate the SFWM generation rate of the bar-disc nanoantenna, finding a pump-normalised generation efficiency of $R_{\mathrm{SFWM}} \approx 84.9\ \mathrm{s}^{-1}\mathrm{mW}^{-1}$ per nanoantenna in up-conversion and $R_{\mathrm{SFWM}} \approx 187\ \mathrm{s}^{-1}\mathrm{mW}^{-1}$ per nanoantenna in down-conversion. We find this to be a competitive result when compared to the SPDC generation rates demonstrated in recent literature for antennas [91], thin films [74], and metasurfaces [92–94]. This is more so the case when considering the fact that the nanoantenna resonance is not optimised at the four-wave mixing wavelength, and the experiment was performed under relatively low power for individual nanoantennas. This suggests that metasurfaces designed for SFWM can be a promising alternative platform to SPDC as a source of ultrafast correlated photons.

We also present evidence of SET being a useful technique for assessing the quality of correlated photon sources with the significant advantages it offers in time and equipment.

A natural extension to the work in this chapter would be to repeat the SET analysis on a much brighter SPDC or SFWM source and compare the estimates of spontaenous photon generation rates to traditional QST methods. This would further validate the effectiveness of the SET approach for future nonlinear metasurface research.

Chapter 7

Conclusion

7.1 Summary

In this thesis, we explored the use of nanoantennas for enhancing nonlinear optical processes. After an introduction and overview of the thesis outline in Chapter 1, we derived the fundamental principles of nonlinear optics and plasmonics in Chapters 2 and 3 that were relevant to later discussions of experimental results.

In Chapter 4, we gave background to our approach to nonlinear nanoantenna design, which is based on nonlinear scattering theory and reciprocity. Under this framework, we are able to predict the nonlinearity of a structure by analysing its linear response to the frequencies of a nonlinear process. We identified several key features of effective nonlinear nanoantennas and provided examples from literature to see how they're used in practice. We then performed our own simulations of two different plasmonic nanoantennas that provided motivation for how they would be used in nonlinear experiments.

In Chapter 5 we performed experiments on the first of these nanoantennas, the coupled waveguide resonator and dimer. We presented a model describing the coupling between

the two components of the nanoantenna and predicted the existence of a critical coupling condition by fitting the model to experimental data. Through SHG and THG measurements, we were able to confirm this prediction and demonstrate the working principle of a mechanism to control the coupling strength in multi-particle structures.

In Chapter 6, we used an existing nanoantenna design, the coupled bar and discs, which had previously demonstrated efficient SHG emission, and demonstrated a new nonlinear process, FWM. We introduced the SET technique and explained how classical FWM experiments on the nanoantenna can be used to characterise its SFWM properties, which is a purely quantum phenomena. We assembled a JSD map for both up- and down-conversion FWM by scanning the seed beam across a wavelength range, and estimated the SFWM generation rate which was found to be on the order of ~ 4 $\mathrm{s}^{-1}\mathrm{mW}^{-1}$ per nanoantenna. As this nanoantenna was not optimised for efficient FWM emission, we found this to be a competitive result and an effective demonstration of SET in practice.

7.2 Outlook

We consider the projects presented in this thesis to still be in the early- to mid-stages of development, as both the experiments in Chapter 5 and 6 were proof-of-concept demonstrations of critical coupling and the SET technique respectively. For the work on critical coupling nanoantennas, gains have already been made at the time of writing this thesis in the fabrication of more accurate structures with geometries that are closer to their nominal values. It is also promising to see how we can exploit the critical coupling and nanofocusing effect by integrating these designs into full-length waveguides that can measure both the coupling-in and coupling-out of optical modes. We also discussed the possibility of combining the nanoantenna with a highly nonlinear polymer to further boost the

nonlinear conversion efficiencies achievable, and this looks promising as a quick progression as similar experiments have been conducted incorporating plasmonic structures with minimal complications.

The work on SET also looks promising as observation of FWM from nanoantennas is in itself a significant achievement. The next steps would be to design tailor-made antennas that can support triple resonances at the three wavelengths involved. This is expected to significantly boost the conversion efficiencies demonstrated in this thesis. Having characterised the single antenna performance, we also propose moving to a proper metasurface design where we illuminate a far wider area of particles. As the efficiency of any nonlinear process is best near the damage threshold of the material, moving to a wider beam area would bring down the efficiency in terms of the input power, but this may be offset by the excitation of multiple antennas. As the tradeoff between per power and per particle efficiency is not immediately clear, exploring this could prove to be insightful for future metasurface design.

References

1. Kerr, J. XL. A new relation between electricity and light: Dielectrified media birefringent. *The London, Edinburgh and Dublin Philosophical Magazine and Journal of Science* **50,** 337–348 (1875).
2. Maiman, T. H. Stimulated Optical Radiation in Ruby. *Nature* **187,** 493–494 (1960).
3. Boyd, R. W. *Nonlinear Optics* 3rd ed. (Academic Press, 2008).
4. Franken, P. A., Hill, A. E., Peters, C. W. & Weinreich, G. Generation of Optical Harmonics. *Physical Review Letters* **7,** 118–119 (1961).
5. Terhune, R., Maker, P. & Savage, C. Optical harmonic generation in calcite. *Physical Review Letters* **8,** 404 (1962).
6. Strickland, D. & Mourou, G. Compression of amplified chirped optical pulses. *Optics Communications* **55,** 447–449 (1985).
7. Burnham, D. C. & Weinberg, D. L. Observation of Simultaneity in Parametric Production of Optical Photon Pairs. *Physical Review Letters* **25,** 84 (1970).
8. Sharping, J. E., Fiorentino, M. & Kumar, P. Observation of twin-beam-type quantum correlation in optical fiber. *Optics Letters* **26,** 367–369 (2001).
9. New, G. *Introduction to nonlinear optics* (Cambridge University Press, 2011).
10. Fox, M. *Optical properties of solids* 2nd ed. (Oxford university press, 2010).
11. Giordmaine, J. Mixing of Light Beams in Crystals. *Physical Review Letters* **8,** 19 (1962).
12. Maker, P., Terhune, R., Nisenoff, M. & Savage, C. Effects of Dispersion and Focusing on the Production of Optical Harmonics. *Physical Review Letters* **8,** 21 (1962).

13. Boyd, G., Miller, R. C., Nassau, K., Bond, W. & Savage, A. LiNbO3: an efficient phase matchable nonlinear optical material. *Applied Physics Letters* **5,** 234–236 (1964).

14. Giordmaine, J. A. & Miller, R. C. Tunable Coherent Parametric Oscillation in LiNbO3 at Optical Frequencies. *Physical Review Letters* **14,** 973 (1965).

15. Krasnok, A., Tymchenko, M. & Alù, A. Nonlinear metasurfaces: a paradigm shift in nonlinear optics. *Materials Today* **21,** 8–21 (2018).

16. Yamada, M., Nada, N., Saitoh, M. & Watanabe, K. First-order quasi-phase matched LiNbO3 waveguide periodically poled by applying an external field for efficient blue second-harmonic generation. *Applied Physics Letters* **62,** 435–436 (1993).

17. Wagner, C. & Harned, N. Lithography gets extreme. *Nature Photonics* **4,** 24–26 (2010).

18. Fan, D. & Ekinci, Y. Photolithography reaches 6 nm half-pitch using extreme ultraviolet light. *Journal of Micro/Nanolithography, MEMS, and MOEMS* **15,** 033505–033505 (2016).

19. Saleh, B. E. & Teich, M. C. *Fundamentals of photonics* (john Wiley & sons, 2019).

20. Zheludev, N. I. & Kivshar, Y. S. From metamaterials to metadevices. *Nature Materials* **11,** 917–924 (2012).

21. Rahmani, M. *et al.* Nonlinear frequency conversion in optical nanoantennas and metasurfaces: materials evolution and fabrication. *Opto-Electronic Advances* **1,** 180021 (2018).

22. Maier, S. A. *Plasmonics: Fundamentals and Applications* (Springer Science & Business Media, 2007).

23. Kauranen, M. & Zayats, A. V. Nonlinear plasmonics. *Nature photonics* **6,** 737–748 (2012).

24. Johnson, P. Christy RW Optical Constants of the Noble Metals. *Phys. Rev,* 4370–4379 (1972).

25. Koch, U. *et al.* Plasmonics—High-speed photonics for co-integration with electronics. *Japanese Journal of Applied Physics* **60,** SB0806 (2021).

26. Lin, L., Bi, X., Gu, Y., Wang, F. & Ye, J. Surface-enhanced Raman scattering nanotags for bioimaging. *Journal of Applied Physics* **129** (2021).

27. Bohren, C. F. & Huffman, D. R. *Absorption and scattering of light by small particles* (John Wiley & Sons, 2008).

28. Novotny, L. & Van Hulst, N. Antennas for light. *Nature photonics* **5,** 83–90 (2011).

29. Miller, R. C. Optical second harmonic generation in piezoelectric crystals. *Applied Physics Letters* **5,** 17–19 (1964).

30. Meyer, M. T. & Schindlmayr, A. Derivation of Miller's rule for the nonlinear optical susceptibility of a quantum anharmonic oscillator. *Journal of Physics B: Atomic, Molecular and Optical Physics* **57,** 095001 (2024).

31. Fontana, J. *et al.* Linear and nonlinear optical characterization of self-assembled, large-area gold nanosphere metasurfaces with sub-nanometer gaps. *Optics Express* **24,** 27360–27370 (2016).

32. Neira, A. D. *et al.* Eliminating material constraints for nonlinearity with plasmonic metamaterials. *Nature communications* **6,** 7757 (2015).

33. Butet, J. & Martin, O. J. Evaluation of the nonlinear response of plasmonic metasurfaces: Miller's rule, nonlinear effective susceptibility method, and full-wave computation. *JOSA B* **33,** A8–A15 (2016).

34. O'Brien, K. *et al.* Predicting nonlinear properties of metamaterials from the linear response. *Nature materials* **14,** 379–383 (2015).

35. Lorentz, H. A. The theorem of Poynting concerning the energy in the electromagnetic field and two general propositions concerning the propagation of light. *Amsterdammer Akademie der Wetenschappen* **4,** 176 (1896).

36. Roke, S., Bonn, M. & Petukhov, A. V. Nonlinear optical scattering: The concept of effective susceptibility. *Physical Review B—Condensed Matter and Materials Physics* **70,** 115106 (2004).

37. De Beer, A. G. & Roke, S. Nonlinear Mie theory for second-harmonic and sum-frequency scattering. *Physical Review B—Condensed Matter and Materials Physics* **79,** 155420 (2009).

38. Danckwerts, M. & Novotny, L. Optical Frequency Mixing at Coupled Gold Nanoparticles. *Physical Review Letters* **98,** 026104 (2007).

39. Shcherbakov, M. R. *et al.* Enhanced Third-Harmonic Generation in Silicon Nanoparticles Driven by Magnetic Response. *Nano Letters* **14,** 6488–6492 (2014).

40. Marino, G. *et al.* Spontaneous photon-pair generation from a dielectric nanoantenna. *Optica* **6,** 1416–1422 (2019).

41. Koshelev, K. *et al.* Subwavelength dielectric resonators for nonlinear nanophotonics. *Science* **367,** 288–292 (2020).

42. Celebrano, M. *et al.* Mode matching in multiresonant plasmonic nanoantennas for enhanced second harmonic generation. *Nature Nanotechnology* **10,** 412 (2015).

43. Schuller, J. A. *et al.* Plasmonics for extreme light concentration and manipulation. *Nature materials* **9,** 193–204 (2010).

44. Biagioni, P., Huang, J.-S. & Hecht, B. Nanoantennas for visible and infrared radiation. *Reports on Progress in Physics* **75,** 024402 (2012).

45. Dombi, P. *et al.* Strong-field nano-optics. *Reviews of Modern Physics* **92,** 025003 (2020).

46. Gramotnev, D. K. & Bozhevolnyi, S. I. Nanofocusing of electromagnetic radiation. *Nature Photonics* **8,** 13–22 (2014).

47. Babadjanyan, A., Margaryan, N. & Nerkararyan, K. V. Superfocusing of surface polaritons in the conical structure. *Journal of Applied Physics* **87,** 3785–3788 (2000).

48. Issa, N. A. & Guckenberger, R. Optical nanofocusing on tapered metallic waveguides. *Plasmonics* **2,** 31–37 (2007).

49. Verhagen, E., Polman, A. & Kuipers, L. Nanofocusing in laterally tapered plasmonic waveguides. *Optics express* **16,** 45–57 (2008).

50. Verhagen, E., Spasenović, M., Polman, A. & Kuipers, L. Nanowire plasmon excitation by adiabatic mode transformation. *Physical review letters* **102,** 203904 (2009).

51. Li, K., Stockman, M. I. & Bergman, D. J. Self-similar chain of metal nanospheres as an efficient nanolens. *Physical review letters* **91,** 227402 (2003).

52. Li, K. *et al.* Balancing near-field enhancement, absorption, and scattering for effective antenna–reactor plasmonic photocatalysis. *Nano letters* **17,** 3710–3717 (2017).

53. Zhang, S., Genov, D. A., Wang, Y., Liu, M. & Zhang, X. Plasmon-induced transparency in metamaterials. *Physical review letters* **101,** 047401 (2008).

54. Fu, M. *et al.* Near-unity Raman β-factor of surface-enhanced Raman scattering in a waveguide. *Nature Nanotechnology* **17,** 1251–1257 (2022).

55. Luk'Yanchuk, B. *et al.* The Fano resonance in plasmonic nanostructures and metamaterials. *Nature materials* **9,** 707–715 (2010).

56. Limonov, M. F., Rybin, M. V., Poddubny, A. N. & Kivshar, Y. S. Fano resonances in photonics. *Nature photonics* **11,** 543–554 (2017).

57. Liu, Y. *et al.* Tunable Fano resonance with ultrahigh peak by bright-dark mode coupling in Dirac semimetal. *JOSA B* **36,** 2461–2467 (2019).

58. Taubert, R., Hentschel, M. & Giessen, H. Plasmonic analog of electromagnetically induced absorption: simulations, experiments, and coupled oscillator analysis. *JOSA B* **30,** 3123–3134 (2013).

59. Liu, N. *et al.* Plasmonic analogue of electromagnetically induced transparency at the Drude damping limit. *Nature materials* **8,** 758–762 (2009).

60. Taubert, R., Hentschel, M., Kästel, J. & Giessen, H. Classical analog of electromagnetically induced absorption in plasmonics. *Nano letters* **12,** 1367–1371 (2012).

61. Boller, K.-J., Imamoğlu, A. & Harris, S. E. Observation of electromagnetically induced transparency. *Physical Review Letters* **66,** 2593 (1991).

62. Fleischhauer, M., Imamoglu, A. & Marangos, J. P. Electromagnetically induced transparency: Optics in coherent media. *Reviews of modern physics* **77,** 633–673 (2005).

63. Gennaro, S. D. *et al.* The Interplay of Symmetry and Scattering Phase in Second Harmonic Generation from Gold Nanoantennas. *Nano Letters* **16,** 5278–5285 (2016).

64. Xiao, X. *et al.* Nanofocusing in Critically Coupled Nanogap Waveguide Resonators. *ACS Photonics* **11,** 2836–2842 (2024).

65. Lin, H., Yang, D., Han, S., Liu, Y. & Yang, H. Analog electromagnetically induced transparency for circularly polarized wave using three-dimensional chiral metamaterials. *Optics Express* **24,** 30068–30078 (2016).

66. Johnson, P. B. & Christy, R.-W. Optical constants of the noble metals. *Physical review B* **6,** 4370 (1972).

67. Ordal, M. A. *et al.* Optical properties of the metals al, co, cu, au, fe, pb, ni, pd, pt, ag, ti, and w in the infrared and far infrared. *Applied optics* **22,** 1099–1119 (1983).

68. Martin, S., Bradley, D., Lane, P., Mellor, H. & Burn, P. Linear and nonlinear optical properties of the conjugated polymers PPV and MEH-PPV. *Physical Review B* **59,** 15133 (1999).

69. Albrecht, G., Hentschel, M., Kaiser, S. & Giessen, H. Hybrid organic-plasmonic nanoantennas with enhanced third-harmonic generation. *ACS omega* **2,** 2577–2582 (2017).

70. Nielsen, M. P., Shi, X., Dichtl, P., Maier, S. A. & Oulton, R. F. Giant nonlinear response at a plasmonic nanofocus drives efficient four-wave mixing. *Science* **358,** 1179–1181 (2017).

71. Yang, J. *et al. Stimulated emission tomography analysis of plasmonic nanoantennas* in *Active Photonic Platforms 2022* **12196** (2022), 78–84.

72. Dichtl, P. M. *Nonlinear Optics on the Nanoscale: Solid State and Quantum Aplications* PhD thesis (Imperial College London, 2021).

73. Santiago-Cruz, T. *et al.* Photon Pairs from Resonant Metasurfaces. *Nano letters* **21,** 4423–4429 (2021).

74. Santiago-Cruz, T., Sultanov, V., Zhang, H., Krivitsky, L. A. & Chekhova, M. V. Entangled photons from subwavelength nonlinear films. *Optics Letters* **46,** 653–656 (2021).

75. Fischer, P. & Buckingham, A. Surface second-order nonlinear optical activity. *JOSA B* **15,** 2951–2957 (1998).

76. Heinz, T. F. in *Modern Problems in Condensed Matter Sciences* 353–416 (Elsevier, 1991).

77. Canfield, B. K. *et al.* Local field asymmetry drives second-harmonic generation in noncentrosymmetric nanodimers. *Nano Letters* **7,** 1251–1255 (2007).

78. Czaplicki, R. *et al.* Second-harmonic generation from metal nanoparticles: resonance enhancement versus particle geometry. *Nano letters* **15,** 530–534 (2015).

79. Schulz, S. A. *et al.* Roadmap on photonic metasurfaces. *Applied Physics Letters* **124,** 260701 (2024).

80. Kaneda, F., Garay-Palmett, K., U'Ren, A. B. & Kwiat, P. G. Heralded single-photon source utilizing highly nondegenerate, spectrally factorable spontaneous parametric downconversion. *Optics express* **24,** 10733–10747 (2016).

81. Gemmell, N. R. *et al.* Loss-compensated and enhanced midinfrared interaction-free sensing with undetected photons. *Physical Review Applied* **19,** 054019 (2023).

82. James, D. F. V., Kwiat, P. G., Munro, W. J. & White, A. G. Measurement of qubits. *Physical Review A* **64,** 052312 (2001).

83. Eckstein, A. *et al.* High-resolution spectral characterization of two photon states via classical measurements. *Laser & Photonics Reviews* **8,** L76–L80 (2014).

84. Liscidini, M. & Sipe, J. Stimulated Emission Tomography. *Physical Review Letters* **111,** 193602 (2013).

85. Fang, B., Cohen, O., Liscidini, M., Sipe, J. E. & Lorenz, V. O. Fast and highly resolved capture of the joint spectral density of photon pairs. *Optica* **1,** 281–284 (2014).

86. Fang, B., Liscidini, M., Sipe, J. & Lorenz, V. Multidimensional characterization of an entangled photon-pair source via stimulated emission tomography. *Optics Express* **24,** 10013–10019 (2016).

87. Yang, Y., Zhang, P. & Ma, X.-S. Stimulated emission tomography for entangled photon pairs with different detection spectral ranges. *JOSA B* **37,** 2071–2075 (2020).

88. Rozema, L. A. *et al.* Characterizing an entangled-photon source with classical detectors and measurements. *Optica* **2,** 430–433 (2015).

89. Ciampini, M. A. *et al.* Stimulated emission tomography: beyond polarization. *Optics Letters* **44,** 41–44 (2019).

90. Gennaro, S. D., Li, Y., Maier, S. A. & Oulton, R. F. Double Blind Ultrafast Pulse Characterization by Mixed Frequency Generation in a Gold Antenna. *ACS Photonics* **5,** 3166–3171 (2018).

91. Zilli, A. *et al. Spontaneous Parametric Down-Conversion Beaming from a Lithium Niobate Nanostructured Resonator* in *CLEO: Fundamental Science* (2023), FTu4C–8.

92. Cheng, X. *et al.* Design of spontaneous parametric down-conversion in integrated hybrid Si x N y-PPLN waveguides. *Optics Express* **27,** 30773–30787 (2019).

93. Santiago-Cruz, T. *et al.* Resonant metasurfaces for generating complex quantum states. *Science* **377,** 991–995 (2022).

94. Son, C. *et al.* Photon pairs bi-directionally emitted from a resonant metasurface. *Nanoscale* **15,** 2567–2572 (2023).